Effect of Electric Field on Relaxor Ferroelectrics Studied by Brillouin Scattering and Dielectric Spectroscopy

Effect of Electric Field on Relaxor Ferroelectrics Studied by Brillouin Scattering and Dielectric Spectroscopy

Md. Aftabuzzaman

February 2018

Effect of Electric Field on Relaxor Ferroelectrics Studied by Brillouin Scattering and Dielectric Spectroscopy

Md. Aftabuzzaman

Doctoral Program in Materials Science

Submitted to the Graduate School of
Pure and Applied Sciences
in Partial Fulfillment of the Requirements
for the Degree of Doctor of Philosophy in
Engineering

at the
University of Tsukuba

Abstract

Relaxor ferroelectrics (REFs) are very fascinating materials because of their excellent piezoelectric and electromechanical properties, and have been extensively studied over the last several decades. Owing to their exceptionally large piezoelectric effect, REFs are very useful materials for applications in piezoelectric devices. REFs can be categorized into the cubic perovskite and uniaxial tetragonal tungsten bronze (TTB) relaxors. Both the perovskite and uniaxial TTB relaxors possess some kinds of disorder in their structure, which induces quenched random fields (RFs) and causes the appearance of polar nanoregions (PNRs). In perovskite relaxors, the sources of RFs are the chemical disorder by random occupancy at B-site and differences in ionic charge and radius between different cations, whereas in TTB relaxors, RFs arise due to random occupancy in unfilled cation sites.

Upon cooling from high temperatures, RFs induce the dynamic PNRs at the Burns temperature T_B. Below T_B, the size of PNRs starts to increase and the interaction among PNRs is initiated, which causes the slowing down of their dynamics and forms the quasistatic PNRs. Consequently, the dynamic-to-static transition of PNRs starts at the intermediate temperature T^*, below which a rapid growth of PNRs is also observed. Upon further cooling, most of the PNRs are frozen into a nonequilibrium polar nanodomain state at the Curie temperature T_C, while RFs restrict the growth of polar macrodomains. Finally, at a sufficiently low temperature called the freezing temperature T_f, all PNR dipoles become frozen into a nonergodic state similar to some kind of glass-like state. Therefore, PNRs are considered to play a vital role in the relaxor behavior by inducing the diffuseness of the ferroelectric phase transition, frequency-dispersive dielectric anomalies, and various precursor phenomena of both the perovskite and TTB relaxors.

Most of the perovskite relaxors are Pb-based, and among them (1-x)Pb($Mg_{1/3}Nb_{2/3}$)O_3-$x$$PbTiO_3$ (PMN-xPT) single crystals with the compositions near morphotropic phase boundary (MPB) (x = 0.33-0.37%) are the most attractive in the application of piezoelectric devices due to their superior piezoelectric properties. They show the maximum dielectric and piezoelectric responses which have the broad range temperature dependencies. These high electrical responses are necessary to increase the efficiency and reduce the size of the various devices such as condensers, actuators, and transducers. From recent study, a further enhancement of the above properties is observed at critical end point (CEP), an upper limit of the critical external electric field at which the polarization rotation energy is decreased significantly. However, the origin of these enhancement of the physical properties is still an intriguing topic for research.

Therefore, in the present study, the acoustic and dielectric properties of PMN-30PT (x = 0.30) single crystals were investigated under the external dc electric field using Brillouin scattering and dielectric spectroscopy to clarify the origin of the field-induced enhancement of dielectric responses. Under a moderate electric field E, a mixed state consisting of field-induced macrodomain and nanodomain due to RFs was identified by observing the longitudinal acoustic (LA) mode splitting in Brillouin scattering and coexistence of Monoclinic (M) and field-induced Tetragonal (T) phases in dielectric measurement. Under a sufficiently high E, the LA mode splitting and the M phase disappear due to the complete switching of nanodomain into the field-induced macro/single domain states by stabilizing the T phase with the E along a

[001] direction. The highest dielectric constant was observed at CEP (at 1.2 kV/cm and at 398K), which was the boundary between a mixed state and a macro/single domain state. Therefore at CEP, the transition from a mixed state to a macro/single domain state was suggested to be the origin of the maximum electric responses in PMN-30PT near the MPB composition. After removing the external field, a field-induced memory effect was observed in the dielectric measurement. Therefore, the origin of this field-induced memory effect and the process of removing this memory were also clarified using dielectric spectroscopy.

Recently, the immense interest of the research on Pb-free materials has been growing due to the emerging demand of such materials in green sustainable technology. Most of the TTB relaxors such as $Sr_xBa_{1-x}Nb_2O_6$ (SBN) and $Ca_xBa_{1-x}Nb_2O_6$ (CBN) are Pb-free and till now the study of these REFs is insufficient and the understanding of their intrinsic mechanism is still unclear. Uniaxial REFs with the TTB structure such as SBN and CBN are very attractive materials for technological applications and basic research owing to their remarkably effective dielectric, piezoelectric, pyroelectric, and photorefractive properties. These excellent physical properties are useful for modern applications such as sensors, data storage, lasers, and holography. The unique combination of outstanding physical features and Pb-free nature makes SBN and CBN single crystals the crucial materials for research. Up to the present, most of the studies of uniaxial TTB REFs have been carried out mainly focusing on their different functional properties and structures, and the origin of the relaxor behavior and its composition dependence. However, the detailed study of the effect of an external E on PNRs is even now insufficient and the role of PNRs in the states above and below T_C is still a puzzling issue of materials science. The PNRs in the paraelectric phase and nanodomain state/static PNRs in the ferroelectric phase are very sensitive to an external E and aging by which they gradually switch into a metastable macro- or even a single domain state. Therefore, a change in acoustic properties of the materials such as sound velocity and sound attenuation is expected, which can easily be detected using Brillouin scattering. Therefore, the use of Brillouin scattering is a new approach of experimental technique to study the aging and electric field effect of the ferroelectric materials.

Therefore, in the present study, the acoustic properties of SBN70 (x = 0.70), SBN40 (x = 0.40) and CBN30 (x = 0.30) single crystals were investigated under zero and externally applied dc E using Brillouin scattering to clarify the critical nature and related functionality of PNRs and domain states in uniaxial REFs with TTB structure. The effect of an external E along the [001] direction was clearly observed. On field heating, an incomplete alignment of nanodomains was observed at a low temperature region of SBN40 due to the formation of a cluster-glass state induced by the interaction among PNRs. Upon heating, this interaction among PNRs becomes very weak neat T_C and therefore, a high E aligns all PNRs along the field direction. As a result a complete switching of nanodomain to a macrodomain states was observed near T_C. Below T_C, an isothermal aging of SBN40 shows a clear memory and rejuvenation effects which indicate the formation of a cluster-glass state due to the interaction among PNRs. In the field-dependent measurement of SBN70, SBN40 and CBN30, a mixed state of macrodomain and nanodomain was observed up to a very high E because of the incomplete switching of nanodomains below T_C due to the interaction among PNRs. A filed-induced macro/single domain state was also observed on field cooling from a high temperature under a lower E.

Contents

Chapter 1
General Introduction

1.1 Historical background of ferroelectric materials

Ferroelectric materials are the highly polar dielectric materials which possess a very high value of dielectric constant and have been known from almost a century. The discovery of the ferroelectricity was leaded by the occurrence of two well-known related phenomena piezoelectricity and pyroelectricity. In piezoelectricity, the electric polarization is induced by mechanical strain [1], while in pyroelectricity, a temperature dependent spontaneous electric dipole moment is observed [2]. The term "pyroelectricity" was already known to the people since ancient time by observing the phenomena that the certain materials have ability to attract small objects when they are heated. The piezoelectricity was discovered by J. Curie and P. Curie in 1880. They observed that the charge induced by non-uniform and uniform heating was actually due to the thermal stress from the microscopic point of view [1]. On much later, ferroelectricity was discovered primarily owing to the fact that at equilibrium, the randomly distributed domain polarizations result a very weak net polarization in the bulk material. The ferroelectricity was first observed by Valasek in 1920 in the Rochelle salt ($KNaC_4H_4O_6 \cdot 4H_2O$) when he found that upon application of an external electric field, the polarization of $KNaC_4H_4O_6 \cdot 4H_2O$ could be reversed [3-8]. However, its crystal structure is very complicated which greatly discourage the researchers for any further theoretical studies. Later on, the ferroelectricity was observed in dihydrogen phosphate (KH_2PO_4) [8-10] and ammonium salts ($(NH_4)H_2PO_4$) [11-13] with less structural complexity. Consequently, Slater introduced the first theoretical model of ferroelectricity which mainly focused on the dipolar units induced by the arrangement of the hydrogen bonds [14]. Since at that time this model was consistent with the experimental results, therefore, during several decades it was believed that hydrogen bonds were essential for the ferroelectricity. In 1945, Wul and Goldman showed that the above statement was not true by observing ferroelectricity in barium titanate ($BaTiO_3$) which was the first ferroelectric crystal without hydrogen bonds. In addition $BaTiO_3$ is the first ferroelectric crystal with more than one ferroelectric phase [15-19]. In 1960s, the ferroelectricity was discovered in many new materials, and research was focused on the most interesting materials with perovskite and tetragonal tungsten bronze structure oxides and ferroelectric polymers [20]. The word "ferroelectricity" is originated from the analogy of the fundamental concept in ferromagnetic materials, such as magnetization, magnetic domains, and magnetic hysteresis loop. However, the inside mechanism behind this phenomenon is completely different from those in the ferroelectric materials. The magnetism can be explained as an intrinsically quantum mechanical phenomenon, while in general the ferroelectricity can be described by means of classical physics [21].

1.2 Ferroelectricity

Ferroelectricity is a characteristic of certain dielectric materials that display spontaneous polarization which can be reversed by applying a suitable external electric field. By heating a ferroelectric

materials above its Curie temperature, its unit cell becomes centrosymmetric, *i.e.*, all the ions assumed to be in the symmetric positions of the unit cell and ferroelectric behavior ceases. Therefore, to be ferroelectrics, the must have requirement is the non-centrosymmetric structure. Among the 32 point groups in crystal symmetry, 21 point groups are non-centrosymmetric due to the absence of center of symmetry. The crystals having these non-centrosymmetric point groups exhibit third-rank tensor properties such as linear electro-optic and piezoelectric effects along a unique crystallographic direction except 432 point group. Among them, 10 point groups *i.e.*, 1, 2, *m*, *mm*2, 4, 4*mm*, 3, 3*m*, 6 and 6*mm* represent the polar crystal classes which exhibit pyroelectricity. The crystal having one of these point groups has a unique rotation axis without having any mirror perpendicular to this axis. Therefore, the atomic arrangement at one end along the unique rotation axis is completely different from that at the other end. As a result, the crystal becomes bi-polar and exhibits spontaneous polarization along a certain crystallographic direction in the absence of an electric field [22]. If this spontaneous polarization can be reversed by the application of an external electric field, the material is said to be ferroelectric. Ferroelectric materials also exhibit piezoelectricity and pyroeletricity.

1.3 Characteristics of ferroelectric materials

1.3.1 Ferroelectric domains and domain walls

Generally in a ferroelectric crystal, the uniform alignment of electric dipoles occurs in a certain region which is known as the ferroelectric domains. The spontaneous polarization in different domains along the different directions causes the zero net polarization. The interface between two adjacent domains is known as a domain wall which is characterized by the angle between the polarization directions on either side of the wall. Generally, the domain walls are very thin *i.e.*, less than a few lattice cells. In a tetragonal ferroelectric

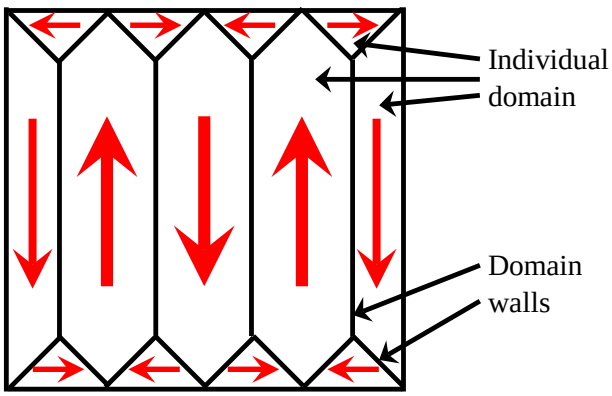

Figure 1.1. Schematic illustration of ferroelectric domains and domain walls. The red arrow indicates the direction of the spontaneous polarization.

phase, the angles between two adjacent domains are either 90° or 180°, while they are 71°, 109°, or 180° in a rhombohedral ferroelectric phase. The region which separates the domains of oppositely oriented polarization is called a 180° domain wall, while a 90° domain wall separates the perpendicular domains. The polarization reversal by applying an external electric field is known as switching. The 180° domain

switching occurs with a minimal structural strains. Whereas, a marked structural deformation is necessary for the switching of 71°, 90°, and 109° domains.

1.3.2 *P-E* hysteresis loop

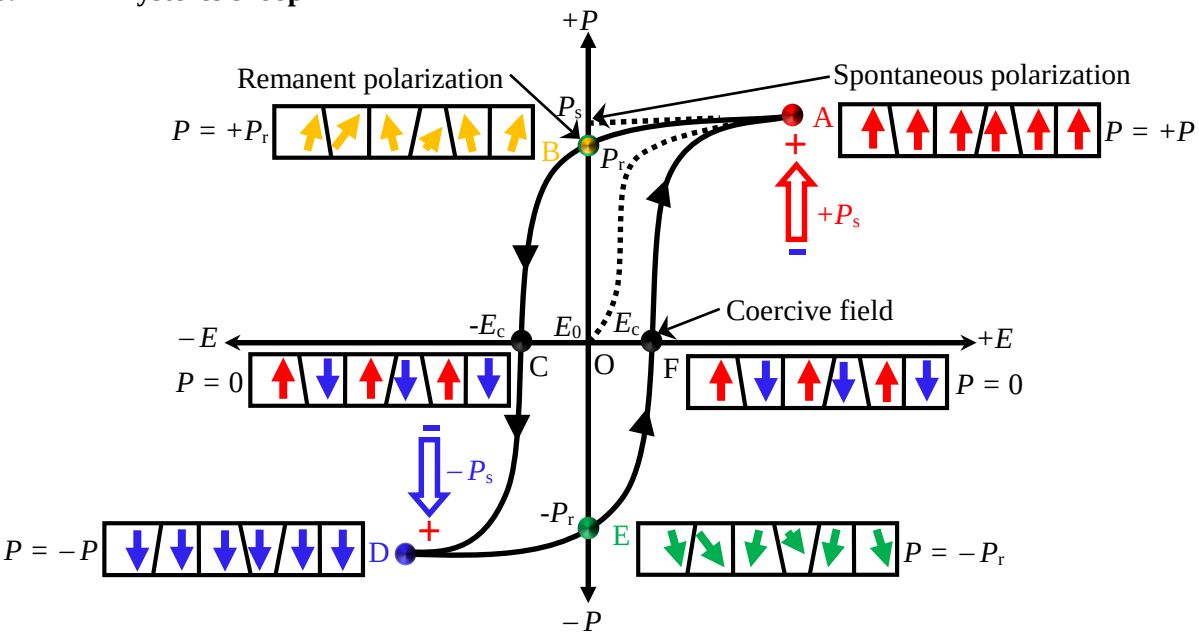

Fig. 1.2. Typical diagram of a *P-E* hysteresis loop in ferroelectric materials.

The typical ferroelectric polarization-electric field (*P-E*) hysteresis loop is shown in Fig. 1.2. When an external *E* is applied along a certain crystallographic direction, the domains with an unfavorable direction of *P* trend to align along the field direction [22]. Under a sufficiently high *E*, all the domains are aligned along the field direction and the *P* becomes saturated (point A in Fig. 1.2) which is known as a spontaneous polarization P_s. This process is reversible and called the polarization switching. When *E* is decreased to zero, $P \neq 0$ *i.e.*, the polarization does not return to the initial value (point B in Fig. 1.2). After the removal of *E*, the amount of switchable *P* is called the remnant polarization P_r. The return of an initial state of *P* requires an application of a reverse *E*. The strength of *E* required to bring the initial sate of *P* is called the coercive field E_C (point C in Fig. 1.2). Upon further increase of the reverse *E*, again *P* becomes saturated (point D in Fig. 1.2) but the direction of *P* is opposite to that of at point A. This indicates a complete switching of domains from a state A to a state D. By decreasing a reverse *E* and reapplying *E* along the initial direction, a complete *P-E* hysteresis loop is observed. The above process can be repeated.

1.3.3 Curie temperature and ferroelectric phase transition

The structural phase transition is one of the most important properties of the ferroelectric materials. Upon cooling, the ferroelectric materials exhibit the structural phase transition from a paraelectric phase to a ferroelectric phase. The temperature at which a paraelectric to ferroelectric phase transition occurs is called the Curie temperature T_C. Some ferroelectric materials possess more than one ferroelectric phase. In that

case, T_C will be only the temperature at which a paraelectric to ferroelectric phase transition occurs. While, the temperature at which the ferroelectric materials exhibit the structural phase transition from one ferroelectric to another ferroelectric phases is simply known as the phase transition temperature.

To interpret the properties of ferroelectric materials, the concept of a ferroelectric phase transition is very important. Generally, the phase transitions are described by using a quantity referred to as the order parameter $\eta(T)$. With the increase of temperature $\eta(T)$ decreases and goes to zero at the T_C. In case of the ferroelectric phase transition, the parameter $\eta(T)$ is denoted as the polarization. Depending on the nature of $\eta(T)$ and its interaction with macroscopic parameter such as strain, the observed phase transitions in crystals are order-disorder, displacive, and electronic types. The order-disorder and the displacive phase transitions correspond to order parameters which are primarily atomic, while electronically induced phase transitions correspond to an electron-lattice coupled order parameter.

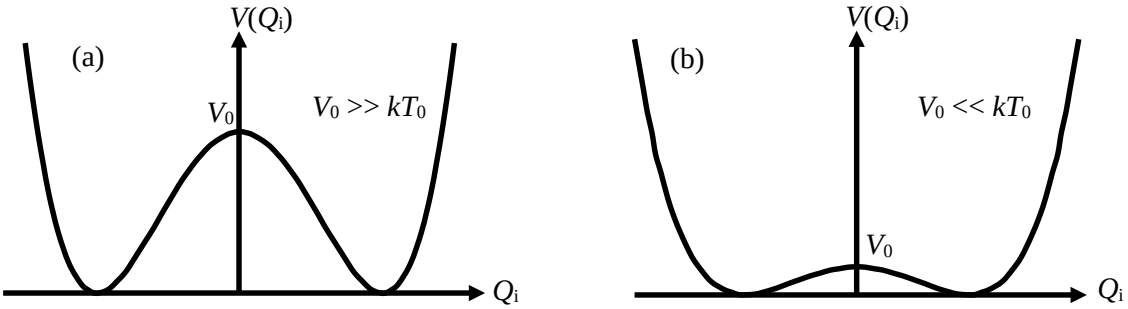

Fig. 1.3. Single cell potentials in (a) order-disorder type and (b) displacive type structural phase transitions.

Figure 1.3 shows the order-disorder and the displacive type phase transitions in terms of single cell potential for a special coordinate Q with an anharmonic potential using the equation [23]

$$V(Q) = aQ^2+bQ^4, \qquad (1.1)$$

where constants $a < 0$ and $b > 0$. Equation (1.1) attributes to a double well potential with an energy difference V_0 between the maximum and two minima. In case of $V_0 >> kT_0$ where T_0 is the transition temperature, the phase transition would be associated with the dynamic ordering at one site or orientation. In case of $V_0 << kT_0$, upon cooling from a high temperature, a cooperative displacements of atoms along Q occurs, which describes the limiting case of a displacive type phase transition. In inelastic light/neutron scattering, the existence of the soft optic phonon indicates the displacive type phase transition, while the presence of a central peak indicates the order-disorder type phase transition in case of ferroelectric materials.

1.3.4 Piezoelectric effect

The word “piezo” is a Greek word meaning pressure and piezoelectricity means pressure electricity [24]. Therefore, piezoelectricity means the ability of materials by which mechanical stress is converted into electric charge [25]. In a more precise sense, the application of mechanical stress on some dielectric materials induces an electric polarization and this effect is called piezoelectricity. All ferroelectric materials

are piezoelectric but all piezoelectric materials are not ferroelectric. In crystals with centrosymmetric structure, the piezoelectric effect is understood as a linear electromechanical interaction of the mechanical and the electrical states. In case of ferroelectric materials in which the paraelectric phase is centrosymmetric, the piezoelectric coefficient d_{mij}, which is third order polar tensor, can be represented as a derivative of strain to electric field by the following equations:

$$d_{mij} = \frac{\partial S_{ij}}{\partial E_m} = \frac{Q_{ijkl} P_k \partial P_l}{\partial E_m} + \frac{Q_{ijkl} P_l \partial P_k}{\partial E_m}, \; i, j, k, l, m = 1,2,3, \tag{1.2}$$

$$d_{mij} = Q_{ijkl} P_k \varepsilon_{lm} + Q_{ijkl} P_l \varepsilon_{km}, \tag{1.3}$$

where S_{ij}, Q_{ijkl}, and ε_{ij} are the strain, electrostrictive coefficient, and dielectric permittivity, respectively.

1.3.5 Electrostrictive effect

Upon the application of an external electric field to a dielectric material, the strain is induced in the material which is proportional to the square of the applied field. The electrostriction is an electromechanical phenomenon in all dielectric materials in which small displacements of ions in a crystal occur upon the application of an external electric field result in overall strain along the direction of the field. The electrostrictive effect describes the strain (S_{ij}) induced by the electric field/polarization, which is proportional to the square of the electric field/polarization, and is expressed by the following equations:

$$S_{ij} = M_{ijkl} E_k E_l, \tag{1.4}$$

$$S_{ij} = Q_{ijkl} P_k P_l, \tag{1.5}$$

where M_{ijkl} and Q_{ijkl} are the electrostrictive coefficients. The electrostriction is a four-rank polar tensor property which can be observed in all crystalline materials [26]. The electrostrictive coefficients are related to each other via the dielectric susceptibility which can be expressed by the following relation:

$$M_{ijmn} = \sum_{kl} \chi_{km} \chi_{ln} Q_{ijkl}, \tag{1.6}$$

where χ_{km} and χ_{ln} are the dielectric susceptibility. Only for weak fields the Eq. (1.4) holds good. Therefore, the Eq. (1.5) is more suitable one to explain the electrostrictive effect. While, for pure electrostrictive effect the Eq. (1.6) is always valid. Therefore in ferroelectric materials, the piezoelectric effect is one kind of electrostrictive effect biased by P_s. Generally, the piezoelectric effect is much stronger than the electrostrictive effect. However in certain materials, the strain direction is independent of the direction of field and hysteresis effects are decreased, which make the electrostrictive effect dominant and preferable. The most commonly used electrostrictive materials are $Pb(Mg_{1/3}Nb_{2/3})O_3$ (PMN), $PbTiO_3$ (PT) and PMN-*x*PT.

1.4 Classification of ferroelectrics

On the basis of dielectric, polarization, and phase transition properties, ferroelectrics can be categorized into two types [2,27]:

(i) Normal ferroelectrics

(ii) Relaxor ferroelectrics

(i) Normal ferroelectrics:

In case of normal ferroelectrics, the dielectric constant does not vary with the frequency of the measurement and a sharp phase transition about T_C is observed. In addition, it undergoes a sharp or progress vanishing of P_s corresponds to a first or second order phase transition respectively. Above T_C *i.e.*, in a paraelectric phase, dielectric constant of normal ferroelectrics follow the well-known Curie-Weiss law:

$$\frac{1}{\varepsilon}=\frac{T-T_C}{C},\ T>T_C\ , \tag{1.7}$$

where T_C and C are the Curie temperature and Curie constant, respectively. The temperature dependence of the dielectric constant of a normal ferroelectric such as $BaTiO_3$ single crystal is shown in Fig. 1.4.

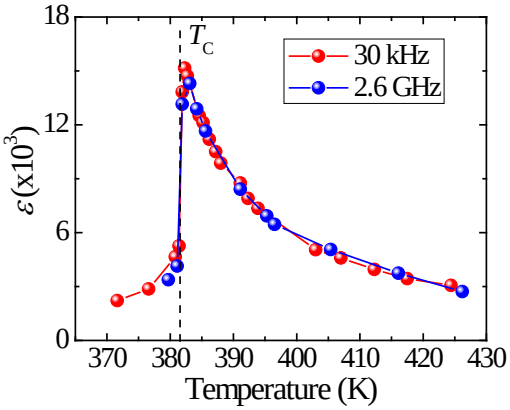

Fig. 1.4. The temperature dependence of the dielectric constant of a $BaTiO_3$ single crystal at some selected frequencies [28].

(ii) Relaxor ferroelectrics:

In relaxor ferroelectrics (REFs), the dielectric constant shows a strong frequency dependency and a broad and diffused phase transition about maximum dielectric temperature T_m is observed as shown in Fig. 1.5. In the high temperature region, RFEs at first follow the Curie-Weiss law and then start to deviate from it below the Burns temperature T_B at which dynamic polar nanoregions (PNRs) appear. Therefore, below the T_B, the dielectric constant no longer obeys the simple Curie-Weiss law and changes with temperature by following the phenomenological equation [29]:

$$\frac{1}{\varepsilon}=\frac{1}{\varepsilon_m}\left[1+\frac{(T-T_m)^\gamma}{2\delta^2}\right],\ (T>T_m)\ ;\ 1<\gamma\leq 2\ , \tag{1.8}$$

where ε_m is a maximum dielectric constant at T_m. γ and δ are fitting parameters corresponding to the degree of diffuseness of a phase transition. When γ = 1, Eq. (1.8) is the same as the Curie-Weiss equation which corresponds to the normal ferroelectrics, while γ = 2 corresponds to the typical relaxor behavior. It is believed that such a peculiar properties of REFs attribute to random fields which is related to PNRs.

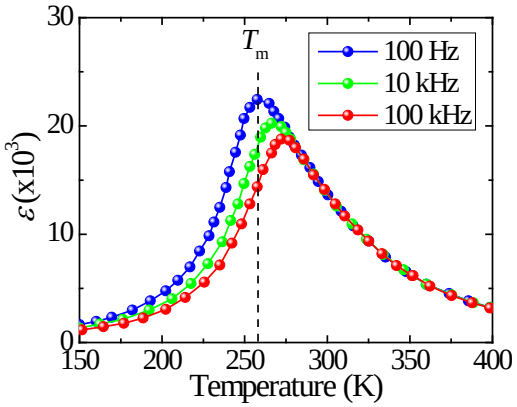

Fig. 1.5. The temperature dependence of the dielectric constant of a $Pb(Mg_{1/3}Nb_{2/3})O_3$ single crystal at some selected frequencies [30].

1.5 Theory of structural phase transition of ferroelectrics

1.5.1 Thermodynamics of the phase transition

There are many microscopic models which have been proposed to explain the origin of ferroelectricity. The most extensively used phenomenological or thermodynamic theory is the Landau-Ginzburg free energy theory [31,32] in which the thermodynamic potential is expressed in terms of an order parameter. Based on this theory, Devonshire developed a phenomenological theory of ferroelectricity by choosing the polarization P as an order parameter to explain the ferroelectric phase transition [33,34]. Generally, the elastic Gibbs function G_1 is the most convenient thermodynamic potential, which can be expressed as a function of temperature, stress, and polarization [35]. For simplicity, Devonshire consider a ferroelectric crystal having an intrinsic spontaneous polarization P_s along a certain crystallographic axis, and express G_1 as a function of polarization by the following equation [34]:

$$G_1(T, P) = G_0(T) + \frac{1}{2}\beta(T)P^2 + \frac{1}{4}\xi(T)P^4 + \frac{1}{6}\zeta(T)P^6 + \dots , \qquad (1.9)$$

where in general, the coefficients G_0, β, ξ, ζ……., are the functions of temperature T. G_0 is the free energy at P = 0. A stable state of a thermodynamic system is described by the minimum value of the free energy G ($G_1 = G$, when E = 0). Therefore at a certain temperature, when a crystal exhibits a stable P_s, the conditions for the minimum value of G are given by

$$E = \left(\frac{\partial G}{\partial P}\right)_{Ps} = 0, \ \left(\frac{\partial^2 G}{\partial P^2}\right)_{Ps} > 0 \text{ , or } \left(\frac{\partial E}{\partial P}\right)_{Ps} = \chi^{-1} > 0 . \qquad (1.10)$$

If Eqs. (1.9) and (1.10) are combined, the equation of state for a ferroelectric system takes the following

form:

$$E = \frac{\partial G}{\partial P} = P_s\left(\beta + \xi P_s^2 + \zeta P_s^4\right) = 0, \tag{1.11}$$

$$\chi^{-1} = \left(\beta + 3\xi P_s^2 + 5\zeta P_s^4\right) > 0\ , \tag{1.12}$$

where E is the Maxwell field (parallel to P_s). The G versus P_s curves are qualitatively shown in Fig. 1.6 (a) using the Eq. (1.9) where ξ and ζ are positive. When β is positive, the free energy curve has the single minimum

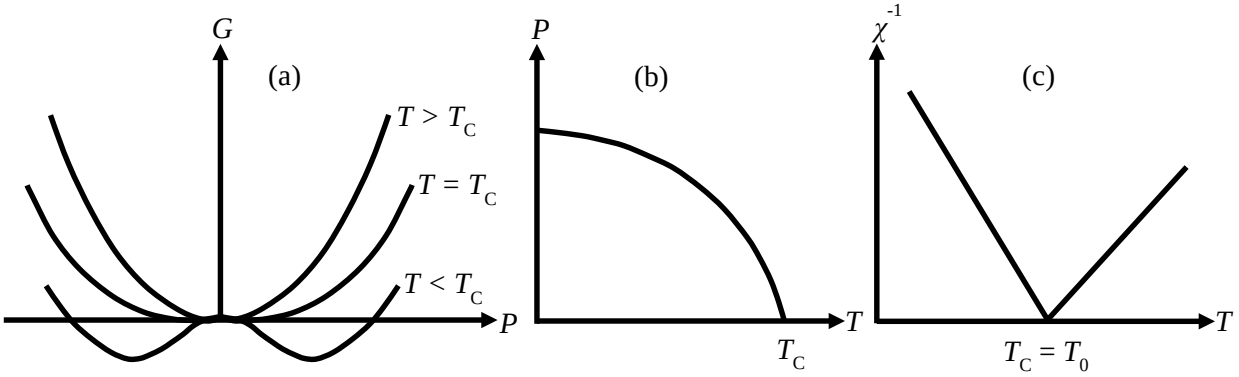

Fig. 1.6. The temperature dependence of (a) the free energy, (b) polarization, and (c) dielectric susceptibility for the second order phase transition.

at $P_s = 0$, and when β is negative, the curve acquires a double-minimum at non-zero value of polarization. Since the minima correspond to the equilibrium value of polarization as a function of temperature, the change of β from positive to negative attributes to the change of stable paraelectric state with $P = 0$ into a ferroelectric state with $P_s \neq 0$. This is called the ferroelectric phase transition. For $P_s = 0$, the Eq. (1.12) can be written as:

$$\chi^{-1} = \beta > 0\ . \tag{1.13}$$

It is obvious that β must be a positive value when the paraelectric phase become stable. Therefore, the boundary condition at T_C becomes $\beta \geq 0$. By expanding β as a Taylor series of $(T\text{-}T_0)$ and considering only the first term in $(T\text{-}T_0)$, β can be written as:

$$\beta = \beta_0(T - T_0)\ . \tag{1.14}$$

By combining Eqs. (1.13) and (1.14), the dielectric susceptibility can be represented as:

$$\chi = \frac{1}{\beta\,(T - T_0)}\ . \tag{1.15}$$

The Eq. (1.15) is known as the Curie-Weiss law which is applicable for the dielectric permittivity in a paraelectric phase. Since ξ and ζ exhibit a very weak temperature dependence, they can be neglected. However, if $P_s \neq 0$, one result corresponds to the first order phase transition when $\xi < 0$, and other result

corresponds to the second order phase transition when $\xi > 0$. According to the Devonshire theory, the temperature dependence of free energy, polarization, and dielectric susceptibility for the second order and first order phase transition are represented in Figs. 1.6 and 1.7, respectively.

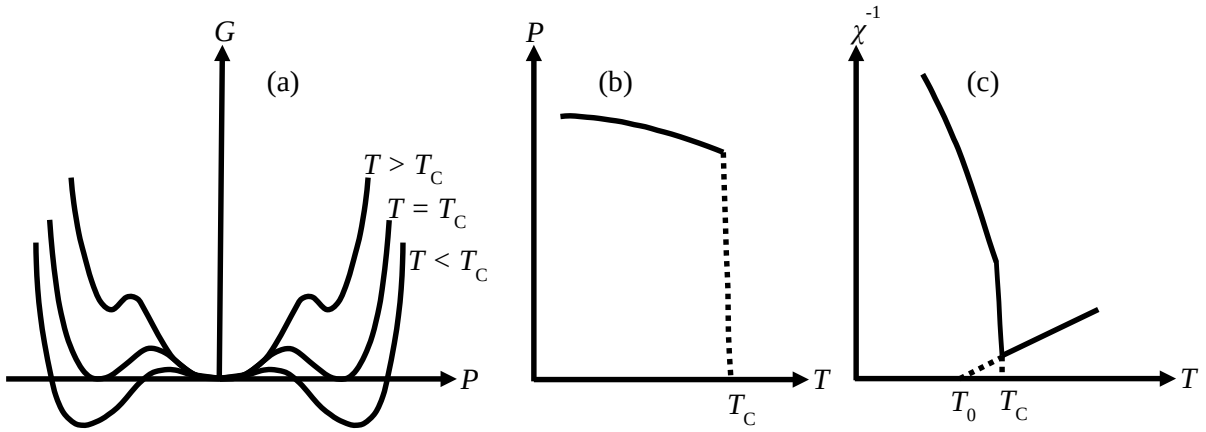

Fig. 1.7. The temperature dependence of (a) the free energy, (b) polarization, and (c) dielectric susceptibility for the first order phase transition.

1.5.2 Devonshire theory

Devonshire rationalizes the phase and phase transition mechanism of ferroelectric materials in terms of Landau-type expansion of the free energy by considering polarization P as an order parameter. He presents a straightforward model with a single temperature dependent second order coefficient and three temperature independent higher order coefficients for the expansion of the free energy to the six order of P [36]. The free energy G can be represented as a function of polarization components P_x, P_y, and P_z using the following relation:

$$G = \frac{1}{2}\beta(P_x^2+P_y^2+P_z^2)+\frac{1}{4}\xi_{11}'(P_x^4+P_y^4+P_z^4)+\frac{1}{2}\xi_{12}'(P_y^2P_z^2+P_z^2P_x^2+P_x^2P_y^2)+\frac{1}{6}\zeta'(P_x^6+P_y^6+P_z^6), \qquad (1.16)$$

where β is a monotonic decreasing function of temperature. It passes through the zero value in the vicinity of a paraelectric to ferroelectric phase transition. Coefficients ξ_{11}', ξ_{12}', and ζ' are the temperature independent and $\zeta' > 0$, $\xi_{12}' > 0$, and $\xi_{11}' < 0$. The field component for an unstressed crystal can be obtained from the derivatives of G with respect to P_x.

$$E_x = \frac{\partial G}{\partial P_x} = \beta P_x + \xi_{11}' P_x^3 + \xi_{12}' P_x\left(P_y^2 + P_z^2\right) + \zeta' P_x^5 . \qquad (1.17)$$

In the absence of an electric field, the field component E_x must be zero and G must be a minimum for the stability. When β is sufficiently large, the minimum of G corresponds to the zero polarization. However, for small or negative value of β, the minimum of G will correspond to the finite polarization. In Eq. (1.16), the second order term is direction independent, but for a given resultant polarization, fourth and sixth order terms have their minima along the axial and diagonal directions, respectively. Therefore, the magnitude of the polarization increases with the decrease of temperature and the direction of the polarization changes from

the axial to a diagonal one. For a zero electric field, the Eq. (1.17) and similar equations take the form:

$$\begin{aligned} P_x &= 0, \text{ or } \zeta' P_x^4 + \xi'_{11} P_x^2 + \xi'_{12}\left(P_y^2 + P_z^2\right) + \beta = 0, \\ P_y &= 0, \text{ or } \zeta' P_y^4 + \xi'_{11} P_y^2 + \xi'_{12}\left(P_z^2 + P_x^2\right) + \beta = 0, \\ P_z &= 0, \text{ or } \zeta' P_z^4 + \xi'_{11} P_z^2 + \xi'_{12}\left(P_x^2 + P_y^2\right) + \beta = 0. \end{aligned} \tag{1.18}$$

For the corresponding minima of G, there are four sets of solution for above equations:

$$\begin{aligned} &P_x = P_y = P_z = 0, \\ &P_x = P_y = 0,\ \zeta' P_z^4 + \xi'_{11} P_z^2 + \beta = 0, \\ &P_x = 0,\ P_y = P_z,\ \zeta' P_z^4 + \left(\xi'_{11} + \xi'_{12}\right) P_z^2 + \beta = 0, \\ &P_x = P_y = P_z,\ \zeta' P_z^4 + \left(\xi'_{11} + 2\xi'_{12}\right) P_z^2 + \beta = 0. \end{aligned} \tag{1.19}$$

Therefore, upon cooling from a high temperature region, the polarization, which is zero in a paraelectric phase, will in turn point along a cubic edge, a face diagonal, and a body diagonal directions. As a result, the crystal symmetry will be changed from the paraelectric cubic ($Pm\bar{3}m$) symmetry to tetragonal ($P4mm$), orthorhombic ($Pmm2$) and rhombohedral ($R3m$) symmetry successively. The typical directions of polarization in the respective phase are shown in Fig. 1.8.

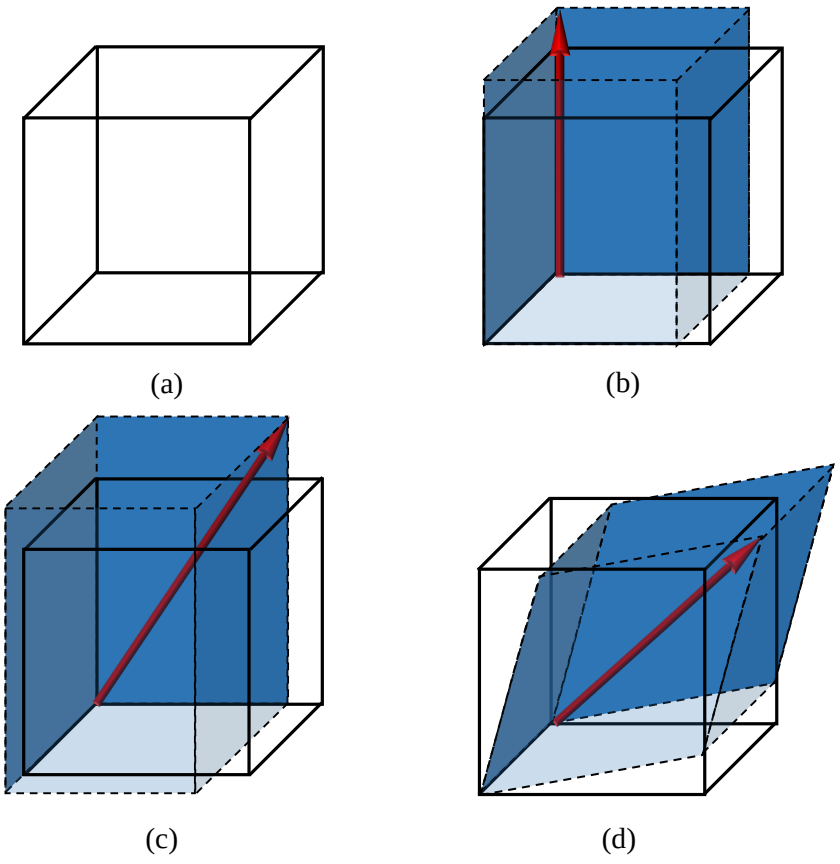

Fig. 1.8. Schematic illustration of the polarization direction in (a) cubic phase, (b) tetragonal phase, (c) orthorhombic phase, and (d) rhombohedral phase.

1.6 Structure of ferroelectrics

According to the differences in the bonding, there are several groups of ferroelectrics. The physical properties of each group are different from other. In general, the structure of ferroelectrics can be categorized into two types:

(i) Cubic perovskite type structure

(ii) Tetragonal tungsten bronze type structure

1.6.1 Cubic perovskite type structure

The term "perovskite" comes from the name Perovsky who discovered the mineral crystals composed of calcium titanate with chemical formula $CaTiO_3$. Therefore, the materials which have the similar type of crystal structure as $CaTiO_3$ are known as the perovskite structures. Many compounds belonging to the perovskite-like structure family exihibit outstanding physical properties. Although $CaTiO_3$ is the natural mineral representing the perovskite material, $BaTiO_3$ is widely used as a reference material in the dielectric industry as well as in the research of ferroelectric materials. The general formula of perovskite structure is ABO_3 in which A-site contains the cation with larger ionic radius, B-site contains the cation with smaller ionic radius, and O is oxygen atom. The crystal structure of ABO_3 type cubic perovskite is shown in

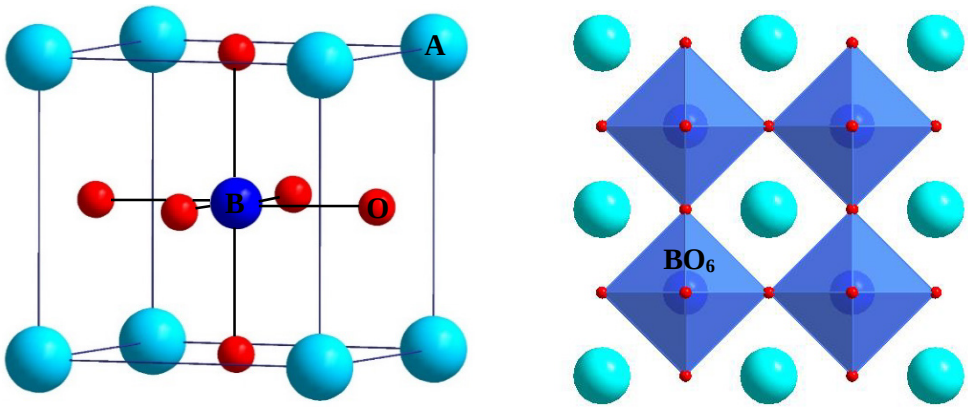

Fig. 1.9. A cubic ABO_3 type perovskite unit cell.

in Fig. 1.9. Most of the ferroelectrics with perovskite type structure have either $A^{2+}B^{4+}O_3^{2-}$ or $A^{1+}B^{5+}O_3^{2-}$ type formula. The crystals with perovskite ABO_3 type structure and its derivative have received a great attention, because they can accommodate various metals with a wide range of valences and ionic radii. Generally, the perovskite structure is a three dimensional network of a BO_6 octahedral unit, it can also be considered as a cubic close pack arrangement of A-site and O ions with B-site ions filling the octahedral interstitial positions. The competition among the degree of freedom of each sublattice leads to the different structural variants such as atom displacements and/or octahedral rotation or tiltings [37-39]. Therefore, more or less important distortions from an ideal cubic structure are observed. This type of distortions can be limited to the local symmetry: nanoregions or nanodomains or can give rise to the long-range order structural phase transition sequence. The perovskite structure has a great importance in materials science because of the following reasons:

(i) Large number of compounds, very stable structure, variety of properties, many practical applications.

(ii) Key role of a BO_6 octahedral unit in ferromagnetism and ferroelectricity.

(iii) Extensive formation of solid solutions: material optimization by composition control and phase transition engineering.

The other important factor which plays a vital role in materials with perovskite structure is the tolerance factor. The stability of BO_6 octahedra can be described by the tolerance factor t using the following relation:

$$t = \frac{R_A + R_O}{\sqrt{2}(R_B + R_O)} \tag{1.20}$$

where R_A, R_B and R_O are the ionic radii of A, B and O ions, respectively. The value of t can be used as a degree of distortion of the perovskite structure from its ideal cubic phase. Therefore, when the structure is closer to the cubic phase, the value of t will be closer to the unity. Generally, the condition to form a stable perovskite structure is $0.9 < t < 1.1$. Above T_C, the materials with perovskite structure have a centrosymmetric structure and therefore, lose all spontaneous polarization. In this state, the material is called paraelectric. Upon cooling through T_C, a phase transition takes place from a paraelectric to a ferroelectric phase. In many ferroelectric materials with perovskite structure, the transition from an ideal cubic phase to the tetragonal, orthorhombic, and rhombohedral phases are well known. These transitions from cubic perovskite structure are the result of a simple distortion of cubic unit cell, or an enlargement of the cubic unit cell, or a combination of both.

In case of many perovskites, A- and B-site ions are substituted by different ionic species with different valences and ionic radii. As a result, the so-called “perovskite solid solution”, with a general formula of $A'_{1-x}A''_xB'_{1-x}B''_xO_3$ appears. The unusual electromechanical properties of lead-oxide perovskite (ABO_3) relaxors such as $Pb(Mg_{1/3}Nb_{2/3})O_3$ (PMN) based $Pb(Mg_{1/3}Nb_{2/3})_{1-x}Ti_xO_3$ (PMN-xPT), $Pb(Zn_{1/3}Nb_{2/3})O_3$ (PZN) based $Pb(Zn_{1/3}Nb_{2/3})_{1-x}Ti_xO_3$ (PZN-xPT) have attracted much attention by their outstanding piezoelectricity. From the technological point of view, PMN-xPT single crystals with the compositions near morphotropic phase boundary (MPB) (x = 0.33-0.37%) are the most attractive in the application of piezoelectric devices due to their superior piezoelectric properties [40]. The PMN-xPT single crystals with composition near the MPB show the maximum dielectric and piezoelectric responses which have a broad range of temperature dependencies [40-42]. These high electrical responses are necessary to increase the efficiency and reduce the size of the various devices such as condensers, actuators, and transducers.

1.6.2 Tetragonal tungsten bronze type structure

Recently, a great interest of the research on Pb-free materials has been growing owing to the emerging demand of such materials in green sustainable technology. Uniaxial RFEs with tetragonal tungsten bronze (TTB) structure such as $Sr_xBa_{1-x}Nb_2O_6$ (SBN) are Pb-free and very attractive materials for technological applications and basic research because of their remarkably effective dielectric, piezoelectric, pyroelectric, and photorefractive properties [43-50]. These outstanding physical properties of TTB relaxors are useful for modern applications such as sensors, data storage [46,49,51-54] lasers, and holography [55,56].

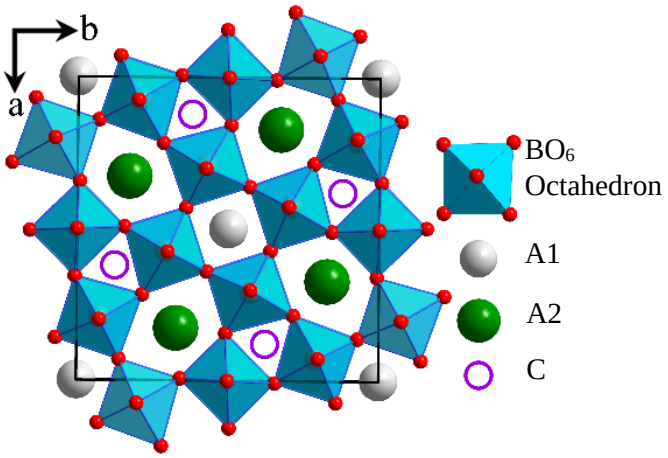

Fig. 1.10. Schematic representation of tetragonal tungsten bronze structure.

The unique combination of colossal functional features and Pb-free nature make TTB relaxors the crucial materials for research. Upon cooling from high temperatures, TTB relaxors show a ferroelectric phase transition from a paraelectric nonpolar 4/*mmm* to a low-temperature ferroelectric polar 4*mm* tetragonal symmetry owing to the loss of inversion center [43]. Therefore, the spontaneous polarization of TTB relaxors has only one single component, which is directed along the tetragonal c-axis. The crystal structure of TTB system is shown in Fig. 1.10. The general formula have the form $(A1)_2(A2)_4C_4(B1)_2(B2)_8O_{30}$ in which six sites are available for A-type and ten sites for B-type cations with corner sharing distorted BO_6 octahedra [57]. In case of SBN, the degree of distortion of a polar NbO_6 octahedra changes with the degree of disorder at A-sites and their ionic occupancy, which are significantly affected by the size and charge of ions. This distortion of NbO_6 octahedra induces the characteristic dielectric and ferroelectric behaviors in TTB relaxors [58-61], and makes three types of interstitial positions consisting of two square A1-sites, four pentagonal A2-sites, and four trigonal C-sites [62]. A1-sites contain only Sr^{2+} ions and A2-sites contain both Ba^{2+} and Sr^{2+} ions, but C-sites and one-sixth of all the A-sites (A1+A2-sites) remain unfilled. Vacancies at A-sites are considered to be the main sources of quenched random fields (RFs) in the TTB structure. With the increase of Sr/Ba ratio, an increase of structural disorder in SBN is observed, that increases the strength of RFs and the diffuseness of the ferroelectric phase transition, and decreases T_C [46,63,64]. It is believed that the quenched RFs create polar nonoregions (PNRs) in the structure which play the vital role in the precursor phenomena of the ferroelectric phase transition and results the relaxor-like behavior [65].

The $Ca_xBa_{1-x}Nb_2O_6$ (CBN) compounds also have the TTB structure with much higher T_C and show quite similar physical properties as the SBN [66-70]. Therefore, their excellent optical and ferroelectric properties make them potential candidates for relatively high temperature applications. In case of CBN, most of the Ca^{2+} ions exclusively occupy A1-sites owing to their smaller ionic radius (1.34 Å), while the relatively larger Ba^{2+} ions (1.61 Å) predominantly occupy A2-sites [71,72]. As a result, the lower degree of disorder of Ca^{2+} and Ba^{2+} ions in CBN causes weak RFs, which prefers the long range order and results the weakly first-order phase transition at T_C [65]. Therefore, the diffusive nature of the phase transition of CBN is less pronounced than that of SBN, and hence, the dielectric constant shows a sharp peak near T_C [73].

With the increase of Ca content, T_C decreases and the ferroelectric phase transition becomes diffusive because of the increase of disorder that indicates the enhancement of RFs [74].

1.7 Polar nanoregions in relaxor ferroelectrics

Some disorder is possessed in the structure of both the perovskite and uniaxial TTB relaxors [51,75], which plays the dominant role to exhibit their excellent physical properties [76]. The quenched RFs are induced by the charged compositional fluctuations [77] which cause the critical slowing down and freezing into nanometric polar domains below the maximum dielectric temperature T_m. The sources of RFs in perovskite relaxors are the chemical disorder and differences in ionic charge and radius between different cations [78], while in TTB relaxors, RFs arise because of the unfilled cation sites [79]. The coupling between RFs and ferroelectric degrees of freedom such as soft lattice modes is suggested to generate polar nanoregions (PNRs) [80] which are believed to induce all the outstanding properties of REFs [77].

Generally in REFs, upon cooling from high temperatures, RFs induce the dynamic PNRs at a certain temperature so called Burns temperature T_B, at which a deviation of the refractive index from its linear temperature dependence is observed [81]. The deviation of acoustic phonons from their high temperature linearity was also observed at T_B [82]. Upon cooling from T_B, the size of PNRs begins to grow and the interaction among PNRs is initiated, which results the slowing down of their dynamics and forms the quasistatic PNRs. Consequently, a dynamic-to-static transition of PNRs takes place at the intermediate temperature T^*, below which a rapid increase of PNRs is observed. As a result, PNRs are considered to play a dominant role in the relaxor behavior by inducing the frequency-dispersive dielectric anomalies, diffuseness of the ferroelectric phase transition, and various precursor phenomena [30,83]. Upon further cooling, most of the PNRs become frozen into a nonequilibrium nanodomain state at T_C or T_m, whereas RFs restrict the growth into macrodomains [67]. Finally, below a certain temperature called the freezing temperature T_f which is below T_C or T_m, all PNR dipoles become frozen into a nonergodic state similar to some kind of glass-like state [84]. The freezing of PNRs attributes to the large and broad peak in the temperature dependence of the dielectric permittivity which shows the characteristic frequency dispersion in both the perovskite and TTB relaxors [30,85]. The temperature evolution of PNRs and characteristic temperatures of REFs are shown in Fig. 1.11.

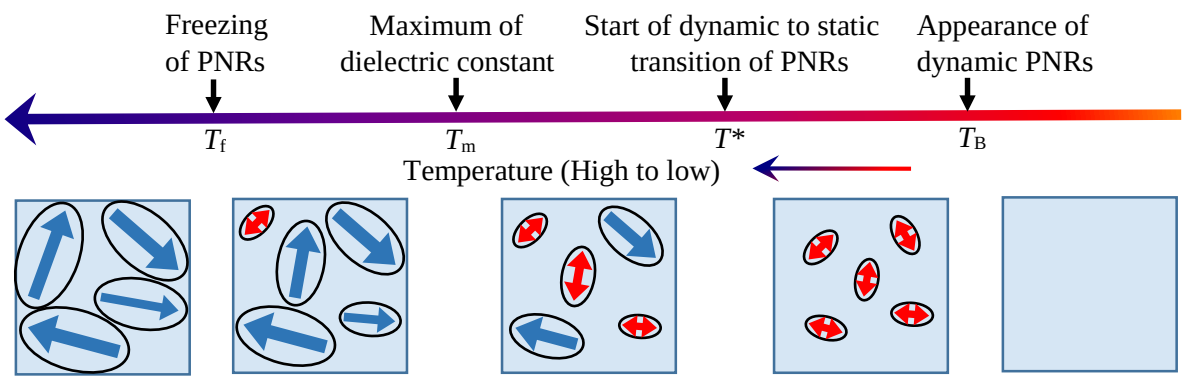

Fig. 1.11. Temperature evolution of PNRs and characteristic temperatures. Ellipses with red and blue arrow represent the dynamic and static PNRs respectively.

The schematic representation of the size of a crystal, nanoregions, and unit cell of relaxor ferroelectric materials is shown in the Fig. 1.12. In perovskite relaxors, the symmetry of PNRs is rhombohedral (R*3m*), while in TTB relaxors, it is tetragonal (4*mm*).

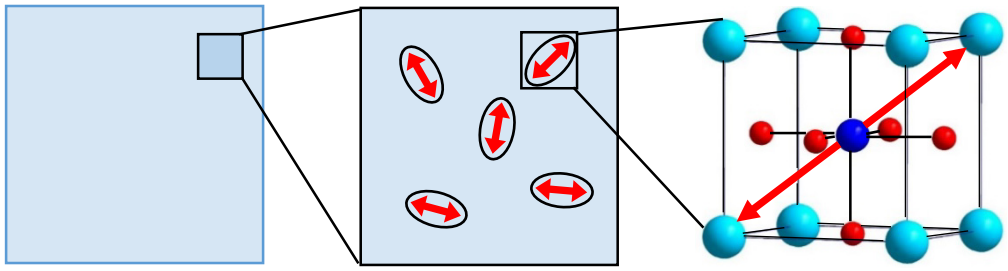

Fig. 1.12. Schematic representation of the size of a (a) crystal, (b) nanoregions, and (c) unit cell of REFs.

1.9 Cluster-glass state in relaxor ferroelectrics

In a disordered magnetic system, the cluster-glass is a state at which the small cluster of spins randomly orient similar to the atomic spins in the spin-glass system where the magnetic spins of the component atoms are randomly oriented. Below the ferromagnetic ordering temperature, the cluster-glass system also exhibits the spin-glass behavior [86].Therefore, cluster-glass is a kind of spin-glass system. However, in a cluster-glass system, groups of spins are locally ordered and form the small domains which interact with each other similar to the single spins in simple spin-glass system. A typical cluster-glass system exhibits the following characteristics: (a) A large difference is observed between zero field cooling and field cooling magnetization, (b) at low temperatures and at a very high magnetic fields, magnetic saturation is not observed, and (c) zero field cooling magnetization exhibits long-time relaxation effect which is not observed in ferromagnetic systems [87].

In case of REFs, a cluster-glass state is formed below T_C, where the small ferroelectric clusters/domains are induced inside the crystal by the interaction among PNRs and induce a spin glass-type random ordering similar to a magnetic system. It was proposed that the cluster-glass state is the ground state of all REFs [84]. In normal ferroelectrics, cumulative aging such as the growth into ordered domains is observed and does not show any memory and rejuvenation effects. While in dipole/spin glass systems, an aging hole is observed in the susceptibility, which shows memory and rejuvenation effects [88].

1.9 Goals of the present study

Most of the perovskite relaxors with a general structural formula ABO_3 such as PMN, PMN-*x*PT, PZN, PZN-*x*PT, and $Pb(Sc_{1/2}Ta_{1/2})O_3$ are Pb-based. They have been intensively studied owing to their great variety of physical properties which are suitable in a wide range of technological applications. From the technological view point, PMN-*x*PT single crystals with compositions near morphotropic phase boundary (MPB) (x = 0.33-0.37%) are most promising materials in the application of piezoelectric devices because of

their superior piezoelectric properties [40]. The PMN-*x*PT single crystals with composition (x = 0.30, PMN-30PT) near the MPB show the maximum dielectric and piezoelectric responses and have a broad range of temperature dependencies [40-42]. Such a high electrical responses are essential to enhance the efficiency and reduce the size of the various devices such as condensers, actuators, and transducers. Up to present, many theoretical and experimental efforts have been given to study PMN-*x*PT system to clarify their colossal functional properties, structures, origin of the relaxor nature, and its composition dependences. Recently, the electric field dependent dielectric measurements of REFs in relation with the critical end point (CEP) have been performed [89-91]. It is observed that their colossal functional properties can be enhanced more by applying an external electric field along a certain crystallographic direction. However, till now, the origin of the enhancement of these physical properties is an intriguing topic for research.

Therefore, in this study, the acoustic and dielectric properties of PMN-30PT single crystals have been investigated by applying an external dc electric field using Brillouin scattering and dielectric spectroscopy to clarify the origin of the field-induced enhancement of dielectric responses. In addition, a field-induced memory effect was observed in the dielectric measurement after removing the external field. Therefore, the origin of this memory effect induced by the external electric field and the process of erasing this memory have also been clarified using dielectric spectroscopy.

Although the Pb-based REFs show very unique physical properties, the Pb may affect the environment because of its high toxicity. Therefore, from the environmental point of view, the development of Pb-free REFs is necessary. Recently, the interest of the research on Pb-free materials has been triggered because of their great demand in green sustainable technology. The uniaxial TTB relaxors such as SBN and CBN are Pb-free and the research on these REFs is still insufficient and till now, the understanding of their intrinsic mechanism is unclear. For modern technological applications and basic research, SBN and CBN are the most promising materials because of their markedly effective dielectric, piezoelectric, pyroelectric, and photorefractive properties. Up to present, most of the research on uniaxial TTB relaxors have been conducted mainly focusing on the composition dependent functional properties and corresponding structures features, sources of RFs and the relaxor nature. The stability of ferroelectric domain patterns under local electric fields has also been investigated. However, the detail study of the effect of external electric field on PNRs is even now insufficient, and the role of PNRs in the paraelectric phase and the ferroelectric domain states is still a puzzling issue of materials science.

The PNRs in the paraelectric phase and the nanodomain state/static PNRs in the ferroelectric phase are greatly affected by the external electric field and aging by which they gradually switch into a macro/single domain state. As a result, the variation of acoustic properties of the materials such as sound velocity and sound attenuation is expected. The Brillouin scattering is an advanced tool to identify the frequency shift and width of acoustic phonon modes which are proportional to the sound velocity and sound attenuation respectively. Therefore, the application of Brillouin scattering spectroscopy to study the aging and electric field effect of the ferroelectric materials is a new initiative of an experimental technique. On the other hand, because of the uniaxial spontaneous polarization, SBN and CBN single crystals are suitable to

study the effect of an electric field on PNRs above and below T_C. Therefore, in this study, the acoustic properties of SBN70 (x = 0.70), SBN40 (x = 0.40) and CBN30 (x = 0.30) single crystals have been investigated under zero and externally applied dc electric field using the Brillouin scattering to clarify the critical nature and related functionality of PNRs and domain states in the uniaxial REFs with TTB structure. In addition, experiments on aging below T_C and its temperature dependence have also been carried out, which will disclose more insights into the understanding of microscopic nature of domain state in a ferroelectric phase.

References

[1] P. Chandra and P. Littlewood, Piezoelectricity, (McGraw-Hill, 1946).

[2] M. E. Lines and A. M. Glass, *Principles and Applications of Ferroelectrics and Related Materials*, (Oxford, 1977).

[3] A. Zeleny and J. Valasek, Phys. Rev. **46**, 0450 (1934).

[4] J. Valasek, Phys. Rev. **24**, 560 (1924).

[5] J. Valasek, Phys. Rev. **65**, 235 (1927).

[6] J. Valasek, Phys. Rev. **20**, 639 (1922).

[7] J. Valasek, Phys. Rev. **19**, 478 (1922).

[8] J. Valasek, Phys. Rev. **17**, 475 (1921).

[9] R. Pease and G. Bacon, Nature **173**, 443 (1954).

[10] R. Pease and G. Bacon, Proceedings of the Royal Society of London Series A - Mathematical and Physical Sciences, **230**, 359 (1955).

[11] F. Wu, Phys. Rev. **168**, 243 (1968).

[12] S. Miller, R. Blinc, M. Brenman, and J. Waugh, Phys. Rev. **126**, 528 (1962).

[13] A. Sawada and Y. Takagi, J. Phys. Soc. Jpn. **31**, 952 (1971).

[14] A. Sawada and Y. Takagi, J. Phys. Soc. Jpn., **33**, 1071 (1972).

[15] B. Wull and L.M. Goldmann, C. R. Acad. Sci. USSR **46**, 139 (1945).

[16] J. C. Slater, J. Chem. Phys. **9**, 16 (1941).

[17] B. M. W. P. Mason, Phys. Rev. **74**, 1622 (1948).

[18] H. H. Wieder, J. Appl. Phys. **26**, 1479 (1955).

[19] P. V. H. F. Kay, Philo. Mag. **40**, 1019 (1949).

[20] T. R. Shrout, H. Chen, L. E. Cross, Ferroelectrics **74**, 317 (1987).

[21] C. Li, R. Guo, A. S. Balla, Ferroelectrics **339**,103 (2006).

[22] Y. Xu, *Ferroelectric Materials and Their Applications*, (North-Holland, London, 1991).

[23] A. K. Muller and H. Thomas, *Structural Phase Transitions I*, (Springer-Verlag, Berlin and New York, 1981).

[24] W. G. Cady, *Piezoelectricity* (McGraw Hill, New York, 1946).

[25] B. Jaffee, W. R. Cook, and H. Jaffee, *Piezoelectric Ceramics*, (London and New York, 1971).

[26] R. E. Newnham, *Properties of Materials: Anisotropy, Symmetry, Structure*, (Oxford, New York, 2005).

[27] I. Rivera, A. Kumar, N. Ortega, R. S. Katiyar, and S. Lushikov, Solid State Commun. **149**, 172 (2009).

[28] U. Kaatze, Metrologia, **47,** S91 (2010).

[29] A. A. Bokov and Z.-G. Ye, Solid State Commun. **116,** 105 (2000).

[30] A. A. Bokov and Z.-G. Ye, J. Mater. Sci., **41,** 31 (2006).

[31] L. D. Landau, Phys. Z. Sowjetunion **11,** 26 (1937).

[32] V. L. Ginzberg, Zh. Eksp, and T. Fiz, **15,** 739 (1945).

[33] A. F. Devonshire, Philos. Mag. **40,** 1040 (1949).

[34] A. F. Devonshire, Adv. Phys. **3,** 85 (1954).

[35] T. Mitsui, I. Tatsuzaki, and E. Nakamura, *An Introduction to the Physics of Ferroelectrics*, (Gordon and Breach, London, 1976).

[36] A. F. Devonshire, Philos. Mag. **40,** 1040 (1949).

[37] F. S. Galasso, Structure, *Properties and Preparation of Perovskite-Type Compounds Pergamon*, (Elmsford, NY, USA, 1969).

[38] A. M. Glazer, Acta Crystallogr. B- Struct. Sci. **28**, 3384 (1972).

[39] P. M. Woodward, Acta Crystallogr. B- Struct. Sci. **53**, 32 (1997).

[40] S. E. Park and T. R. Shrout, J. Appl. Phys. **82**, 1804 (1997).

[41] S. Zhang and F. Li, J. Appl. Phys. **111**, 031301 (2012).

[42] H. Ohwa, M. Iwata, H. Orihara, N. Yasuda, and Y. Ishibashi, J. Phys. Soc. Jpn. **70**, 3149 (2001).

[43] J. R. Oliver, R. R. Neurgaonkar, and L. E. Cross, J. Appl. Phys. **64**, 37 (1988).

[44] W. H. Huang, D. Viehland, and R. R. Neurgaonkar, J. Appl. Phys. **76**, 490 (1994).

[45] R. R. Neurgaonkar, W. F. Hall, J. R. Oliver, W. W. Ho, and W. K. Cory, Ferroelectrics **87**, 167 (1988).

[46] A. M. Glass, J. Appl. Phys. **40**, 4699 (1969).

[47] B. Fischer, M. Cronin-Golomb, J. O. White, A. Yariv, and R. Neurgaonkar, Appl. Phys. Lett. **40**, 863 (1982).

[48] R. R. Neurgaonkar, W. K. Cory, J. R. Oliver, M. D. Ewbank, and W. F. Hall, Opt. Eng. **26**, 265392 (1987).

[49] F. Kahmann, J. Höhne, R. Pankrath, and R. A. Rupp, Phys. Rev. B **50**, 2474 (1994).

[50] M. Wesner, C. Herden, R. Pankrath, D. Kip, and P. Moretti, Phys. Rev. E **64**, 036613 (2001).

[51] R. Blinc, Advanced Ferroelectricity (Oxford University Press, Oxford, U.K., 2011) International Series of Monographs on Physics, Vol. 151, p. 144.

[52] A. M. Glass, Appl. Phys. Lett. **13**, 147 (1968).

[53] M. H. Francombe, Acta Crystallogr. **13**, 131 (1960).

[54] W. Kleemann, J. Dec, V. V. Shvartsman, Z. Kutnjak, and T. Braun, Phys. Rev. Lett. **97**, 065702 (2006).

[55] M. O. Ramírez, D. Jaque, L. E. Bausá, J. G. Solé, and A. A. Kaminskii, Phys. Rev. Lett. **95**, 267401 (2005).

[56] Y. Qiao, S. Orlov, D. Psaltis, and R. R. Neurgaonkar, Opt. Lett. **18**, 1004 (1993).

[57] A. Torres-Pardo, R. Jiménez, J. M. González-Calbet, and E. García- González, Inorg. Chem. **50**, 12091 (2011).

[58] K. Li, X. L. Zhu, X. Q. Liu, and X. M. Chen, Appl. Phys. Lett. **102**, 112912 (2013).

[59] L. Wei, Z. Yang, H. Ren, and X. Chen, J. Am. Ceram. Soc. **93**, 3986 (2010).

[60] K. Li, X. L. Zhu, X. Q. Liu, and X. M. Chen, Appl. Phys. Lett. **101**, 042906 (2012).

[61] S. Lanfredi, C. Darie, F. S. Bellucci, C. V. Colin, and M. A. L. Nobre, Dalton Trans. **43**, 10983 (2014).

[62] W. L. Zhong, Physics of Ferroelectrics (Science Press of China, Beijing, 1996).

[63] V. V. Shvartsman, J. Dec, S. Miga, T. Łukasiewicz, and W. Kleemann, Ferroelectrics **376**, 1 (2008).

[64] C. David, T. Granzow, A. Tunyagi, M. Wöhlecke, T. Woike, K. Betzler, M. Ulex, M. Imlau, and R. Pankrath, Phys. Status Solidi A **201**, R49 (2004).

[65] K. Suzuki, K. Matsumoto, J. Dec, T. Łukasiewicz, W. Kleemann, and S. Kojima, Phys. Rev. B **90**, 064110 (2014).

[66] M. Eßer, M. Burianek, D. Klimm, and M. Mühlberg, J. Cryst. Growth **240**, 1 (2002).

[67] K. Matsumoto and S. Kojima, Jpn. J. Appl. Phys. **54**, 10NC04 (2015).

[68] H. Song, H. Zhang, X. Xu, X. Hu, X. Cheng, J. Wang, and M. Jiang, Mater. Res. Bull. **40**, 643 (2005).

[69] H. Song, H. Zhang, Q. Jiang, X. Xu, C. Lu, X. Hu, J. Wang, and M. Jiang, J. Cryst. Growth **290**, 431 (2006).

[70] U. Heine, U. Völker, K. Betzler, M. Burianek, and M. Mühlberg, New J. Phys. **11**, 083021 (2009).

[71] K. Lin, H. Wu, F. F. Wang, Y. C. Rong, J. Chen, J. X. Deng, R. B. Yu, L. Fang, Q. Z. Huang, and X. R. Xing, Dalton Trans. **43**, 7037 (2014).

[72] A. Niemer, R. Pankrath, K. Betzler, M. Burianek, and M. Muehlberg, World J. Condens. Matter Phys. **2**, 80 (2012).

[73] Y. J. Qi, C. J. Lu, J. Zhu, X. B. Chen, H. L. Song, H. J. Zhang, and X. G. Xu, Appl. Phys. Lett. **87**, 082904 (2005).

[74] K. Suzuki, K. Matsumoto, J. Dec, T. Łukasiewicz, W. Kleemann, and S. Kojima, Proc. 34th Symp. Ultrasonic Electronics, 2013, p. 29.

[75] L. E. Cross, Ferroelectrics **76**, 241 (1987).

[76] W. Kleemann, J. Mater. Sci. **41**, 129 (2006).

[77] B. P. Burton, E. Cockayne, and U. V. Waghmare, Phys. Rev. B **72**, 064113 (2005).

[78] V. Westphal, W. Kleemann, and M. D. Glinchuk, Phys. Rev. Lett. **68**, 847 (1992).

[79] W. Kleemann, J. Dec, P. Lehnen, R. Blinc, B. Zalar, and R. Pankrath, Europhys. Lett. **57**, 14 (2002).

[80] J.-H. Ko, D. H. Kim, and S. Kojima, Phys. Rev. B **77**, 104110 (2008).

[81] G. Burns and F. H. Dacol, Phys. Rev. B **28**, 2527 (1983).

[82] S. Tsukada and S. Kojima, Jpn. J. Appl. Phys. **49**, 09ME03 (2010).

[83] R. Pirc and R. Blinc, Phys. Rev. B **76**, 020101(R) (2007).

[84] W. Kleemann, J. Dec, and S. Miga, Phase Transitions **88**, 234 (2015).

[85] J. Dec, W. Kleemann, Th. Woike, and R. Pankrath, Eur. Phys. J. B **14**, 627 (2000).

[86] Y. Nakai and Y. Tsunoda, *Spin glass, cluster glass, mictomagnetism and reentrant spin glass*, (SpringerMaterials, Springer-Verlag Berlin Heidelberg, 1999).

[87] P. S. Anil Kumar, P. A. Joy, and S. K. Date, J. Phys.: Condens. Matter **10**, L487 (1998).

[88] L. K. Chao, E. V. Colla and M. B. Weissman, Phys. Rev. B **72** 134105 (2005).

[89] Z. Kutnjak, J. Petzelt, and R. Blinc, Nature **441**, 956 (2006).

[90] Z. Kutnjak, R. Blinc, and Y. Ishibashi, Phys. Rev. B **76**, 104102 (2007).

[91] T. Imai, S. Toyoda, J. Miyazu, J. Kobayashi, and S. Kojima, Jpn. J. Appl. Phys. **53**, 09PB02 (2014).

Chapter 2

Inelastic Light Scattering and Dielectric Spectroscopy

2.1 Light scattering

In a solid material, light is scattered by the fluctuations in the dielectric tensor. The fluctuations of certain physical quantities are coupled with the fluctuations in the dielectric tensor. The fluctuations of some physical quantities become significant in the vicinity of a phase transition temperature, and provide some useful information regarding the dynamical aspect of a structural phase transition. Therefore, the use of light scattering is a powerful technique to investigate the structural phase transition phenomena. The obtained integrated scattered intensity gives the necessary information related to the total fluctuations of the appropriate physical quantity which coherently corresponds to a phase transition. Whereas, the measured peak frequency and line width of the spectral power density provide the information about the structure and dynamics of the solid materials undergoing the structural phase transition [1-7].

In a light scattering experiment, an incident light with angular frequency ω_0, which coming from an intense monochromatic light source (usually a laser), interacts with the collective excitations exist in the medium. These interactions give rise to the scattered light with a wide range of spectral distribution of frequencies as shown in Fig. 2.1.

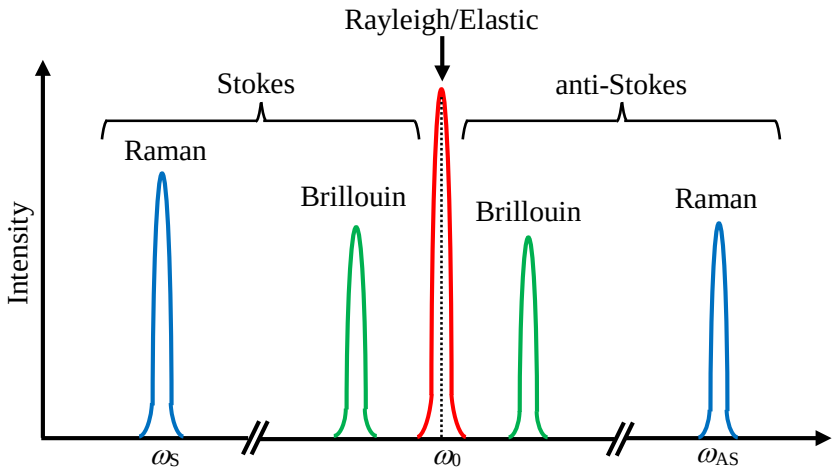

Fig. 2.1. Schematic spectra of scattered light.

The peak at the center position of the spectra corresponds to the incident photons which have been scattered elastically or quasi-elastically without change in frequency. This is known as Rayleigh/elastic scattering. The remaining peaks in the spectra correspond to the inelastic scattering of light and their shifts from ω_0 normally occur in two separate ranges of frequency. One of them is called Brillouin scattering component and the other is Raman scattering component as shown in Fig. 2.1. The inelastic scattering of light by low frequency acoustic phonons give rise to Brillouin scattering spectra which occurs very close to ω_0. The typical frequency shifts in Brillouin scattering components are approximately 3~60 GHz (0.1~2 cm^{-1}). Whereas, the inelastic scattering of photon by internal vibrations of molecules or optic vibrations in crystals

gives rise to Raman spectra which lie at a higher frequency region normally in the range of 10 ~ 4000 cm^{-1}. The spectra of inelastic light scattering can be subdivided into two events namely Stokes and anti-Stokes components correspond to the creation and annihilation of the excitation quanta, respectively.

The kinematics of the scattering of light can be derived either from the quantum mechanical or classical viewpoint. Classically, it is assumed that each lattice vibration, ($\mathbf{q}$, ω) perturbs the dielectric constant ε in such a way that it can be represented by the following relation [8]:

$$\varepsilon = \varepsilon_0 + \sum_{q,\omega} \varepsilon_{k\omega} \exp i\left(\mathbf{q}\cdot\mathbf{r} - \omega t\right) = \varepsilon_0 + \delta\varepsilon \tag{2.1}$$

or, in the tensor form

$$\varepsilon_{ij}(\mathbf{r},t) = \hat{e}_i \cdot \boldsymbol{\varepsilon}(\mathbf{r},t).\hat{e}_j = \varepsilon_{ij}^0 + \delta\varepsilon_{ij}(\mathbf{r},t)\ . \tag{2.2}$$

When a plane of monochromatic light wave $E(\mathbf{r},t) = E_0 \exp i\ (\mathbf{k}_0\cdot\mathbf{r}-\omega_0 t)$ traverses through a crystal, there will be an "excess polarization" $\delta p_{ij} = \delta\varepsilon_{ij}E_0/4\pi$, which will give rise to a scattered field $E_s(\mathbf{r},t)$. This scattered field can be represented in the following form

$$E_s(\mathbf{r},t) = \delta\varepsilon_{ij}(\mathbf{r},t) \propto \sum_{k,\omega_q} \exp i\ [\mathbf{k}_s\cdot\mathbf{r} - \left(\omega_0 \pm \omega_q\right)t] \int_V \exp i\ (\mathbf{k}_0 \pm \mathbf{q} - \mathbf{k}_s).\mathbf{r}'\mathrm{d}V'. \tag{2.3}$$

The volume integral in Eq. (2.3) provides a δ-function in ($\mathbf{k}_0 \pm \mathbf{q} - \mathbf{k_s}$), which imposes the wave vector conservation. Therefore, there are 3sN normal modes in a crystal, where s is the number of atoms in a unit cell and N is the number of unit cell. Kinematically, 3s of the modes (one on each branch) can give the light scattering with frequency ω_0 in a certain direction. Thus, the scattered field will consist of components at $\omega_0 \pm \omega_q$, where ω_q are the 3s frequencies at which a vertical line at $|\mathbf{q}| = |\mathbf{k}_0-\mathbf{k}_s| \approx 2|\mathbf{k}_0|\sin\frac{1}{2}\varphi$ intersects the 3*s* branches of the dispersion curve. It is necessary to decompose $\delta\varepsilon_{ij}(\mathbf{r},t)$ in terms of Fourier components in frequency ω and in wave vector $\mathbf{q}$ according to

$$\delta\varepsilon_{ij}(\mathbf{q},\omega) = \frac{1}{2\pi V}\iint_{-\infty}^{\infty} \delta\varepsilon_{ij}(\mathbf{r},t)\exp(i\mathbf{q}.\mathbf{r} - i\omega t)\, d^3\mathbf{r}dt$$

$$= \frac{1}{2\pi}\int_{-\infty}^{\infty} \delta\varepsilon_{ij}(\mathbf{q},t)\mathrm{e}^{-i\omega t}dt\ . \tag{2.4}$$

The similar results can be obtained from the second-quantized theory of lattice dynamics, where each normal mode $\{\mathbf{q},\omega\}$ can be expressed in terms of a number of quanta (phonons) with energy of $\hbar\omega$ and crystal momentum $\hbar\mathbf{q}$.

Fig. 2.2. Typical diagram for the first order photon-phonon scattering.

The light scattering event is induced by the creation or annihilation of a phonon as shown in Fig. 2.2. The conservation of momentum and energy between the phonons and photons provide for Stokes event

$$\begin{aligned} \mathbf{k}_s &= \mathbf{k}_0 - \mathbf{q} \\ \omega_s &= \omega_0 - \omega_q \end{aligned} \tag{2.5}$$

In case of anti-Stokes event

$$\begin{aligned} \mathbf{k}_s &= \mathbf{k}_0 + \mathbf{q} \\ \omega_s &= \omega_0 + \omega_q \end{aligned} \tag{2.6}$$

From Eq. (2.4), the spectral power density of the scattered light can be determined as

$$\begin{aligned} I_{ij}(\mathbf{q},\omega) \propto \left|\delta\varepsilon_{ij}(\mathbf{q},\omega)\right|^2 &\propto \frac{1}{2\pi}\int_{-\infty}^{\infty} dt\, e^{-i\omega t}\langle\delta\varepsilon_{ij}(\mathbf{q},t)\delta\varepsilon_{ij}(\mathbf{q},0)\rangle \\ &\propto [n(\omega)+1]\mathrm{Im}\delta\chi_{ij}(\mathbf{q},\omega). \end{aligned} \tag{2.7}$$

The second identity in Eq. (2.7) is the result of Wiener-Khinchin theorem and the angle brackets express ensemble (thermal) average. The third identity is the fluctuation-dissipation theorem in which χ_{ij} is the dielectric susceptibility, $n(\omega)$ is the Bose-Einstein population factor at frequency ω, which is given by

$$n(\omega) = \frac{1}{\exp\left(\frac{\hbar\omega}{k_B T}\right)-1}, \tag{2.8}$$

where k_B is the Boltzmann constant and $\hbar$ is the Dirac constant.

It is observed from Eq. (2.7) that the spectral power density of scattered light is proportional to the Fourier transform of the time correlation function of the fluctuation of dielectric tensor $\delta\varepsilon_{ij}(\mathbf{q},t)$. Therefore, the mechanism underlying the structural phase transition in a solid material is contained in the time correlation function $\langle\delta\varepsilon_{ij}(\mathbf{q},t)\delta\varepsilon_{ij}(\mathbf{q},0)\rangle$. The order parameter, polarization P in case of ferroelectric materials, can be approximately characterized by the quantities coherence length and correlation time. It is necessary to mention that the spectral intensity is proportional to the imaginary part of dielectric susceptibility. It is very useful for analyzing a spectrum.

2.2 Brillouin scattering

2.2.1 Theory of Brillouin scattering

As the values of wave vector **q** are very small, therefore, the components because of the acoustic phonon modes appear at very low frequencies compared to those of optic phonon modes, and are measured by Brillouin scattering. While, the optic phonon modes are measured by Raman scattering. The basic difference between Brillouin and Raman scattering arises from the dispersion relation of quasi-particle generated. The Brillouin process is considered when the frequency is zero for $\mathbf{q} = 0$, while the Raman process is considered when $\omega(\mathbf{q} = 0) \neq 0$. Since the long wavelength acoustic phonon modes involve in-phase

motion of all atoms in a unit cell, the atomic displacements are almost unchanged over the distances in the order of ≈ 100 unit cells, therefore, one may discuss these phonon modes in terms of an elastic continuum mode.

In Brillouin scattering, the Stokes and anti-Stokes doublet are symmetrically located about the unshifted line appears due to the Bragg-like scattering by propagating sound waves in a solid medium. The condition of the Bragg-like scattering is as follows

$$\lambda = 2\Lambda \sin\frac{\phi}{2}\,, \tag{2.9}$$

where λ, ϕ, and Λ are the wavelength of light in a medium, scattered angle, and wavelength of the propagating sound wave, respectively. The components of Brillouin scattering are then because of a Doppler shift $\Delta\omega$ due to the movement of atomic grating via the propagation of sound wave. Hence, $\Delta\omega$ is given by

$$\begin{aligned}\Delta\omega = \omega_s - \omega_0 &= \pm 2\frac{cv\omega_0}{n}\sin\frac{1}{2}\phi \\ &= \pm 2\, vn|\mathbf{k}_0|\sin\tfrac{1}{2}\phi = \pm 4\,\frac{\pi n}{\lambda_0} v \sin\tfrac{1}{2}\phi\,,\end{aligned} \tag{2.10}$$

where ω_0 and ω_s are the incident and scattered light frequencies, respectively, n is the refractive index of the medium, and $\mathbf{k}_0$ is the wave vector of incident light. The above Eq. (2.10) was first derived by Brillouin in 1922, and it was observed that the frequency shifts are linear function of $\sin\frac{1}{2}\phi$, and a maximum shift can be obtained for the back scattering geometry ($\phi = \pi$). In the long wavelength limit, for a particular **q**, the polarization and frequencies of three acoustic modes can be obtained from elastic constants C_{iklm} using the following equation of motion:

$$\rho\ddot{\mathbf{u}} = C_{iklm}\frac{\partial^2 \mathbf{u}_m}{\partial \mathbf{r}_k \partial \mathbf{r}_l}\,,\ (1 \le i, k, l, m \le 3), \tag{2.11}$$

where $\mathbf{u}(\mathbf{r},t)$ is the local displacement vector. The solution of Eq. (2.11) can be simplified by the restrictions placed on the elastic constants by crystal symmetry [9]. The plane wave solutions to Eq. (2.11) can be obtained for a given **q**, and one can find 3 modes, usually of mixed polarization. Only for a particular direction of **q**, one pure longitudinal and two pure transverse modes can be found.

One can solve the optical coupling between dielectric tensor and strain completely in terms of Poockel's elasto-optic or photoelastic constants P_{mn} [9]. In 6-component notation, the strain field X_n distorts the reciprocal dielectric tensor (or dielectric impermeability tensor, 2nd rank polar tensor) B_m by following the relation

$$\Delta B_m = P_{mn} X_n\,,\ m, n = 1 \sim 6, \tag{2.12}$$

However, in Brillouin scattering, $\mathbf{q}\rightarrow 0$ limit of acoustic modes attribute to the rigid translation of the crystal as a whole, and does not perturb the dielectric constant. The Brillouin effect is observed only in the limit $\mathbf{q} \neq 0$. Therefore, unlike Raman scattering, Brillouin scattering tensors depend on the direction of **q** as well

as $\boldsymbol{E}_0$ and $\boldsymbol{E}_s$. As a result, one cannot generate a single set of scattering tensors comparable to Raman scattering tensors, but can be compelled to calculate the scattering tensors for each direction of **q**. For all crystal systems, Brillouin scattering tensors for different directions of **q** were reported in Ref. 10.

2.2.2 Brillouin scattering tensors and selection rules

By assuming the plane wave solutions $\mathbf{u}_i = \mathbf{u}_i^0 \exp i(\mathbf{q}\cdot\mathbf{r}-\omega t)$, and substituting this in Eq. (2.11) we have

$$\left|C_{iklm}\mathbf{q}_k\mathbf{q}_l-\rho\omega^2\delta_{im}\right|\mathrm{u}_m^0 = 0\ . \tag{2.13}$$

This equation have non-trivial solutions only if the secular determinant vanishes:

$$\left|C_{iklm}\mathbf{q}_k\mathbf{q}_l-\rho\omega^2\delta_{im}\right| = 0\ , \tag{2.14}$$

where $\mathbf{q}_k$ and $\mathbf{q}_l$ are the components of **q**.

In case of long wavelength acoustic modes, $\omega = vq$ where v is the appropriate velocity of sound. Hence

$$\left|C_{iklm}\mathbf{q}_k\mathbf{q}_l-\rho v^2\delta_{im}\right| = 0\ . \tag{2.15}$$

If the elastic constants C_{iklm} of the crystal are known, Eq. (2.15) can be solved for every direction of **q**, which will give three eigenvalues of velocity v_i (i = 1, 2, 3). If each of v_i can be put back in Eq. (2.15), the displacement eigenvectors corresponding to each v_i can be determined. When **q** is selected in the high symmetry direction, the displacement eigenvectors will be parallel or perpendicular to **q**, which corresponds to one longitudinal (L) and two transverse (T) modes. For general directions of **q**, the displacement vectors can be neither parallel nor perpendicular to **q**, which results in the mixed polarization modes. The mixed polarization modes in this case are indicated by QL (quasi-longitudinal) or QT (quasi-transverse) in order to show that displacement vector is more nearly parallel or perpendicular to **q**.

In case of long wavelength limit, the distortion of local dielectric constant is caused by the local strain through elasto-optic or photo-elastic effects. By multiplying the 6-component stain with the 6 × 6 Pockel's tensor gives the 6-component ΔB which can be converted to 3 × 3 forms of $\Delta B_{\alpha\beta}$. When xyz-axes are selected to correspond to principle axes of the dielectric tensor, ΔB_ij are related to the change in dielectric tensor ε_ij which can be expressed as [8]:

$$\delta\varepsilon_\mathrm{ij} = -\varepsilon_{0\mathrm{ii}}\varepsilon_{0\mathrm{jj}}\Delta B_\mathrm{ij}\ . \tag{2.16}$$

Hence, one can get the distortion in dielectric tensor induced by an acoustic wave by a tensor

$$\left|\delta\varepsilon_\mathrm{ij}\right| = \mathbf{qu}\boldsymbol{T}\ , \tag{2.17}$$

where the element T_ij of the tensor $\boldsymbol{T}$ is $\varepsilon_\mathrm{ii}\varepsilon_\mathrm{jj}$ times $\Delta B_\mathrm{ij}/\mathbf{qu}$. The Rayleigh ratio, which is the differential cross section per unit volume, can be derived from excess dipole moment per unit volume $p_\mathrm{i}(\mathbf{r}) = \delta\varepsilon_\mathrm{ij}E_\mathrm{j}^0/4\pi$.

If we consider that the excitation of each acoustic mode is in the thermal equilibrium at temperature T, then:

$$<(\mathbf{qu})^2> = k_B T/2V\rho v^2. \quad (2.18)$$

Therefore, for Rayleigh ratio of the j-th acoustic mode (j = 1, 2, 3) with velocity v_j, by considering e_0 and e_s as unit vectors in the direction of the polarization of incident and scattered fields [5,11,12], we have

$$R^j = \frac{kT\pi^2}{2\lambda_s^4 \rho v_j^2} \left[e_s . T^j . e_0\right]^2 \left(\frac{n_s}{n_0}\right), \quad (2.19)$$

where λ_s denotes the wavelength of the scattered light.

For scattering geometries at which sound waves propagate along high symmetry directions, the structure of the $\boldsymbol{T}$-tensors is sufficiently simple so that selection rules can be derived without specifying the numerical values of elastic constants. Scattering tensors for a number of high symmetry directions in each of the crystal classes have been reported previously in the literature [5,7,11,13].

2.3 Dielectric spectroscopy

In case of an isotropic and linear dielectrics, the time dependent polarization $\boldsymbol{P}(t)$ and dielectric displacement $\boldsymbol{D}(t)$ are related to the time dependent electric field $\boldsymbol{E}$(t) and the susceptibility χ by the relations:

$$\boldsymbol{P}(t) = \chi \boldsymbol{E}(t), \quad (2.20a)$$

$$\boldsymbol{D}(t) = \varepsilon \boldsymbol{E}(t), \quad (2.20b)$$

where $\varepsilon = 4\pi\chi+1$, is the dielectric constant. In dynamical case, the polarization and dielectric displacements are ceased from Eq. (2.20) when the frequency ω of time dependent electric field with amplitude $\boldsymbol{E}^0$ [$\boldsymbol{E}(t) = \boldsymbol{E}^0 \cos\omega t$] is very high, because the motions of the microscopic particles cannot follow the changes in the filed fast enough. At this condition, $\boldsymbol{D}(t)$ can also be expressed in terms of ω, an amplitude, $\boldsymbol{D}^0$, and a phase difference, δ, with respect to the electric field as:

$$\boldsymbol{D}(t) = \boldsymbol{D}^0 \cos(\omega t - \delta), \quad (2.21)$$

Therefore, the value of phase difference varies with the change in frequency of the electric field. For very low frequency, δ becomes zero approaching to quasi-static state. $\boldsymbol{D}(t)$ can be divided into two parts, one is the in phase with $\boldsymbol{E}(t)$ and other having the phase difference of $\pi/2$, by the relation

$$\boldsymbol{D}(t) = \boldsymbol{D}^0 \cos\delta \cos\omega t + \boldsymbol{D}^0 \sin\delta \sin\omega t, \quad (2.22)$$

By defining $\cos\delta = \frac{\varepsilon'(\omega)\boldsymbol{E}^0}{\boldsymbol{D}^0}$ and $\sin\delta = \frac{\varepsilon''(\omega)\boldsymbol{E}^0}{\boldsymbol{D}^0}$, $\boldsymbol{D}(t)$ can be written as

$$\boldsymbol{D}(t) = \varepsilon'(\omega)\boldsymbol{E}^0 \cos\omega t + \varepsilon''(\omega)\boldsymbol{E}^0 \sin\omega t, \quad (2.23)$$

where the quantities $\varepsilon'(\omega)$ and $\varepsilon''(\omega)$ are the real and imaginary parts of the frequency dependent complex dielectric constant $\varepsilon^*(\omega)$. Equations (2.22) and (2.23) will be equivalent when, $D^0 = \sqrt{\varepsilon'^2+\varepsilon''^2}$ and $\tan\delta = \frac{\varepsilon''}{\varepsilon'}$. $\varepsilon'(\omega)$ is considered as the generalization of dielectric constant for sinusoidally varying fields and $\varepsilon''(\omega)$ describes the energy loss in the dielectrics. The typical frequency dependence of $\varepsilon'(\omega)$ and $\varepsilon''(\omega)$ for all polar compounds in a condensed phase is shown in Fig. 2.3.

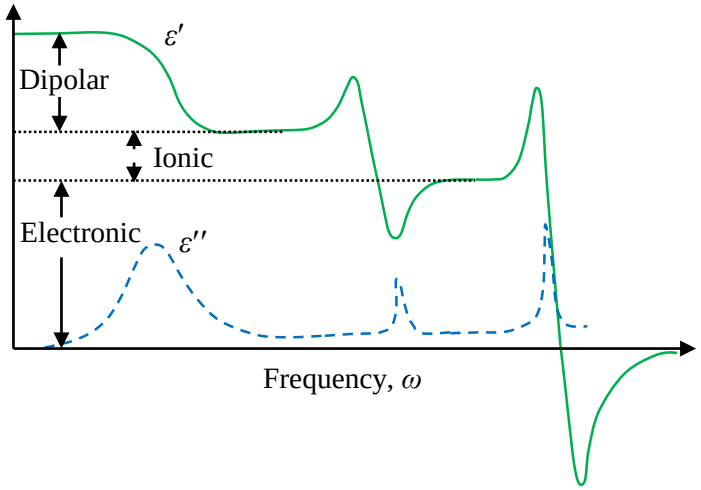

Fig. 2.3. Typical illustration of dielectric dispersion and loss tangent of polar compound.

The frequency dependence dielectric constant and loss factor are different in different frequency ranges. At low frequency regions, $\varepsilon'(\omega)$ is equal to static dielectric constant ε' and $\varepsilon''(\omega)$ is zero. With the increase of frequency, at first, $\varepsilon'(\omega)$ decreases rather slowly, while there are sharp increases followed by a decrease in the higher frequencies of the electromagnetic waves such as IR, visible light, and UV. The $\varepsilon''(\omega)$ shows a peak in the neighborhood of the frequencies where $\varepsilon'(\omega)$ varies. The non-equilibrium effects, appear with the increase in frequency, arise from the electric polarization which consists of three parts *i.e.*, the electronic, atomic, and orientational polarization. Each part corresponds to the motions of electrons, atoms, and molecules and ions, respectively, with different characteristic times. In orientational polarization region, the broad absorption peaks as shown in Fig. 2.3 indicate that there is no discrete energy level exist for the rotational motion of molecules because of the manifold interactions. Therefore, the orientationl polarization is characterized by the relaxation process and the polarization induced by a number of relaxation processes. The complex dielectric constant can be represented in terms of relaxation (with relaxation time τ) as:

$$\varepsilon^*(\omega) = \varepsilon_\infty + \frac{\varepsilon - \varepsilon_\infty}{1+i\omega\tau} \tag{2.24}$$

with real and imaginary part as:

$$\varepsilon'(\omega) = \varepsilon_\infty + \frac{\varepsilon - \varepsilon_\infty}{1+\omega^2\tau^2}, \tag{2.25}$$

$$\varepsilon''(\omega) = \frac{(\varepsilon-\varepsilon_\infty)\omega\tau}{1+\omega^2\tau^2}. \tag{2.26}$$

In order to account for broader peaks in $\varepsilon''(\omega)$ more realistically, it is supposed that different parts of orientational polarization decline with distribution of relaxation times with the distribution function $g(\tau)$ as:

$$\varepsilon^* = \varepsilon_\infty + (\varepsilon - \varepsilon_\infty) \int_0^\infty \frac{g(\tau)d\tau}{1+i\omega\tau} \tag{2.27}$$

with $$\int_0^\infty g(\tau)d\tau = 1. \tag{2.28}$$

The existence of dielectric dispersion in a complex dielectric response is one of the important characteristics of relaxor ferroelectric materials. Therefore, it is very important to study the dielectric properties to clarify the relaxor nature of ferroelectric materials.

2.4 Instrumentation

2.4.1 Brillouin scattering spectroscopy

2.4.1.1 Functions of Fabry-Perot interferometer

In 1899, the Fabry-Perot interferometer (FPI) is designed by C. Fabry and A. Perot with a marked improvement over the Michelson interferometer. The FPI is used in a high resolution spectroscopy where MHz to GHz resolution is required. The FPI consists of two plane mirrors which are mounted accurately parallel to each other with the optical spacing L_1 between them. For a given optical spacing L_1, the interferometer transmits only a certain wavelength λ as determined by

$$T = \frac{\tau_0}{1+\left(\frac{4F^2}{\pi^2}\right)\sin^2\left(\frac{2\pi L_1}{\lambda}\right)}, \tag{2.29}$$

where τ_0 (<1) denotes the maximum possible transmission determined by losses in the system, and F is the finesse which is a quality factor depending primarily on the flatness and mirror reflectivity. Equation (2.29) represents that only those wavelengths satisfying the following condition and for an integral values of m, will be transmitted.

$$L_1 = \frac{1}{2} m\lambda. \tag{2.30}$$

The schematic illustration of the condition is shown in Fig. 2.4.

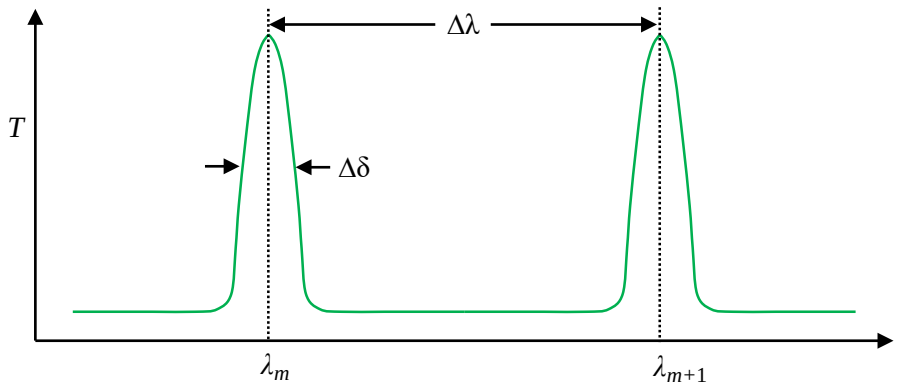

Fig. 2.4. Two successively wavelengths transmitted from a single FPI.

The F is related to the spacing between successive transmitted wavelengths $\Delta\lambda$ which is known as the free spectral range (FSR) and the width $\Delta\delta$ of a given transmission peak, can be represented by the following equation:

$$F = \Delta\lambda/\Delta\delta. \tag{2.31}$$

Since the FPI is used as a spectrometer by changing L_1, therefore it can be used to scan the light intensity at different wavelengths. However, for a certain L_1, the measured intensity will be the sum of intensities for all wavelengths satisfying the Eq. (2.30).

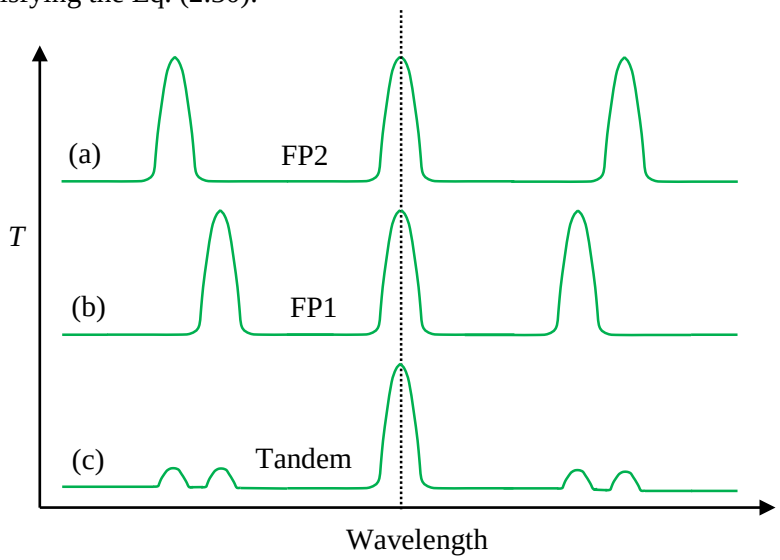

Fig. 2.5. The transmission properties of (a) FP2, (b) FP1, and (c) FPs in series.

Therefore, an unambiguous interpretation of the spectrum is impossible unless it is known a priori that the light spectrum entirely lies within a wavelength spread $<\Delta\lambda$. It is true since

$$\Delta\lambda = \lambda^2/2L_1. \tag{2.32}$$

It is apparent from Eq. (2.32) that $\Delta\lambda$ can be made arbitrarily large by decreasing L_1. However, $\Delta\delta$ increases proportionally with the increase of $\Delta\lambda$ and consequently, the resolution of spectra decreases. In fact Eq. (2.31) represents the finesse F which is just the ratio between FSR $\Delta\lambda$ and the resolution $\Delta\delta$ of the spectra. In practice, because of limitations on the quality of mirror substrates and coatings, F cannot be increased much greater than about 100. Therefore, the relation between FSR and resolution is fixed within the limits which can be determined by the achievable values of F.

2.4.1.2 Tandem Febry-Perot interferometer

Based on the concept of a scanning stage, it is possible to enhance the functionality of FPI by combining two interferometers on a single scanning stage in order to achieve both statically and dynamically stable synchronization. The most convenient arrangement is a Vernier system as shown in Fig. 2.6 where the spacing of second interferometer L_2 is close to L_1. The wavelengths transmitted by the combination obviously satisfy simultaneously the following condition for integral values of m and n:

$$L_1 = \frac{1}{2}m\lambda \text{ and } L_2 = \frac{1}{2}n\lambda. \tag{2.33}$$

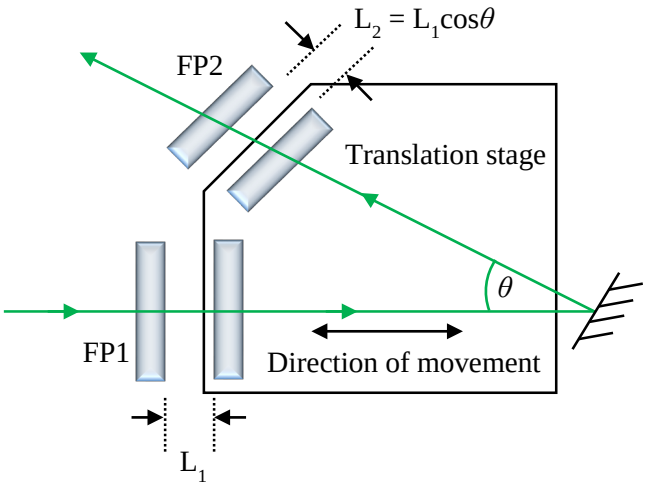

Fig. 2.6. Schematic view of the operation of a tandem Fabry-Perot interferometer.

The combined transmitted light passing successively through both FP1 and FP2 is shown in Fig. 2.6 in a schematic view, where L_1 and L_2 are set independently so that they transmit a given wavelength λ. The neighboring transmission peaks do not coincide; however, FSR of the FP1 form the transmission peaks again coincide after several times. Small "ghosts" of intervening transmission peaks exist because the transmission of either interferometer as show in Eq. (2.29) never falls exactly to zero. Therefore, the FSR of the tandem system is increased by a considerable factor over that of the single interferometer keeping the similar resolution $\Delta\delta$. In order that the first ghost is not too noticeable and one should chose L_1 and L_2 in such a way that $F > L_1/(L_1\text{-}L_2)$. The optimum value of the ratio $L_2/L_1$is around 0.95.

It is important to scan two interferometers synchronously by changing L_1 and L_2 simultaneously in order to use the tandem interferometer system as a spectrometer. It is observed from Eqs. (2.30) and (2.33) that in order to scan a given increment of wavelength, the change of spacing δL_1 and δL_2 must be satisfied by the following condition:

$$\frac{\delta L_1}{\delta L_2} = \frac{L_1}{L_2}. \tag{2.34}$$

The typical values of δL_1 and δL_2 are 1 to a few μm. The operation principle of a practical scanning tandem FP is shown in Fig. 2.6, which was designed by Sandercock. The first interferometer FP1 is arranged in such a way that it lie in the direction of the movement of translation stage, where one mirror sits on translation stage and other on a different angular orientation device. The second interferometer FP2 lies on its axis with an angle θ to the direction of scan, where one mirror is placed on the translation stage in a close proximity to the mirror of FP1 and the other mirror is for adjustment purposes. The relative spacing between the mirrors is set so that that the movement of the translation stage to the left would bring both set of mirrors into the simultaneous contact. While, the movement of translation stage to the right sets the spacing to L_1 and $L_1\cos\theta$. As a result, a scan of δL_1 of the translation stage creates the change of spacing δL_1 in FP1 and $\delta L_1\cos\theta$ in FP2. In other words, Eq. (2.34) is satisfied in which the two interferometers scan synchronously.

2.4.1.3 Optics for a six-pass tandem Febry-Perot interferometer

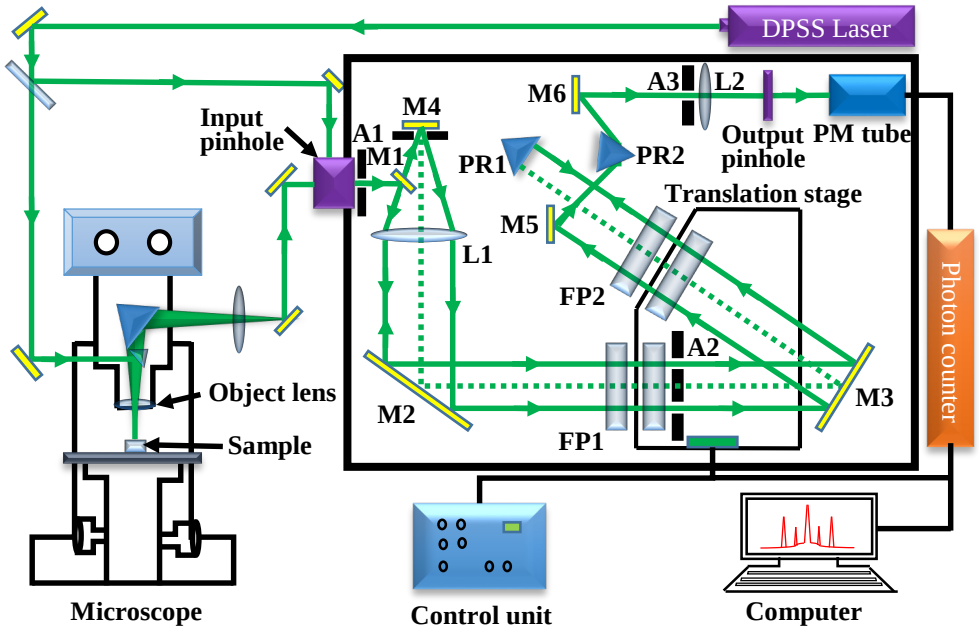

Fig. 2.7. Optics for a Sandercock type 3+3 pass tandem interferometer equipped with microscope and photo multiplier.

Schematic illustration of the optical arrangement of Brillouin scattering system, which was designed by Sandercock [14,15] using the combination of two interferometers FP1 and FP2, is shown in Fig. 2.7. In the present study, an optical microscope used for the backward scattering geometry [16]. A diode pumped solid state (DPSS) laser with the wavelength of 532 nm is employed into the optical microscope with the aid of a small mirror to focus the sample. The scattered light is collected by the objective lens, which enter into the FP interferometer via the adjustable pinhole P1. The aperture A1 then determines the cone of light which is accepted. Mirror M1 reflects the light towards the lens L1, and after the collimation, the reflected light redirects to FP1 via the mirror M2. The redirected light is then passed through aperture 1 of the mask A2, and is entered into FP2 via the mirror M3. After transmission through FP2, the light is reflected back from the 90^{o} prism PR1 and directed towards FP2 in parallel. Then the reflected light continues along FP1 through the aperture 2 of A2 via mirror M3. After passing through FP1 and the lens L1, the light is focused onto the mirror M4 through the underneath of the mirror M1. The light is then returned back from the mirror M4 and collimated by the lens L1. After collimation, the light is directed towards FP1 via the mirror M2. The combination of lens L1 and mirror M4 which lie on the focus of L1 is known as a catseye, and is optically equivalent to a corner cube but has the advantage that it also acts as a spatial filter which can remove undesirable beams such as beams reflected from the rear surfaces of mirrors of interferometer. After final transmission through interferometers, the light is directed towards the prism PR2 via the mirror M5. The combination of prism PR2, lens L2, and the output pinhole forms a bandpass filter with a width which is determined by the size of pinhole. The mirror M6 sends the light into the photomultiplier via the aperture A3, lens L2 and output pinhole. Finally, the resultant scattered signal is recorded by a multi-channel analyzer

(MCA). However, every optical component including two FPs inside the box of interferometer has adjustable screws for convenient operation, and thus we have followed the six (3+3) pass light optics without detail explanation of the optical adjustments. Special techniques such as stabilization, isolation of vibration, and assurance of linear scan are employed and realized by the control unit.

2.4.2 Dielectric spectroscopy

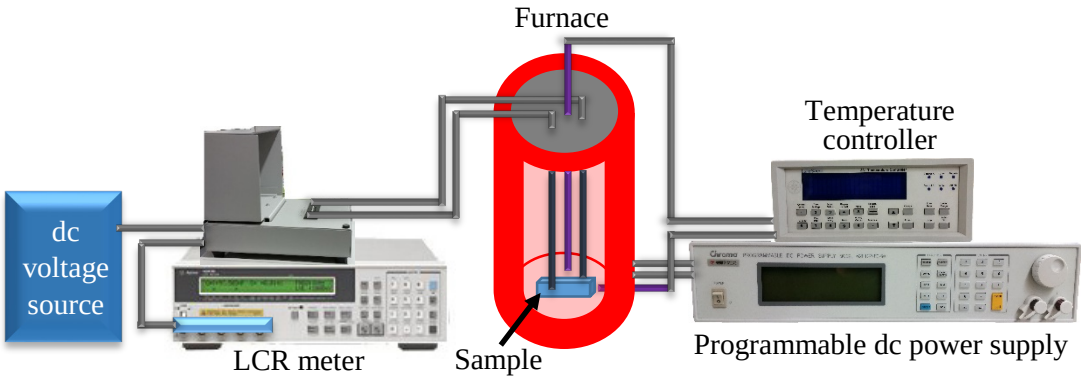

Fig. 2.8. Schematic diagram of dielectric measurement system.

The schematic diagram of the dielectric measurement system is shown in Fig. 2.8. The sample is placed in a home-made box furnace. The temperature of the furnace is controlled within a range from room temperature to 1000 K by a LakeShore 331 temperature controller with a Chroma 62012P-80-60 programmable dc power supply. The dielectric constant of the sample is measured by using a LCR meter (Agilent 4263B). A dc electric field is applied to the sample by using a power supply (Matsusada P4K-80H) with the help of an external bias text fixture. The data are collected with the aid of a PC by using NI LabVIEW^{TM} software in terms of capacitance and dielectric loss. The real ε' and imaginary ε'' part of the dielectric constant are determined by the following equations:

$$\varepsilon' = \frac{C_P\, d}{\varepsilon_0\, A} \quad \text{and} \quad D = \frac{\varepsilon''}{\varepsilon'}, \tag{2.35}$$

where C_P and D are the experimentally measured quantities, capacitance and dielectric loss, respectively. ε_0, d, and A denote the permittivity of free space (8.85×10^{-12} F/m), thickness of the sample, and the surface area of electrodes of the sample, respectively.

References

[1] R. Loudon, Adv. Phys. **13**, 423 (1964).

[2] Z. Iqbal and F. J. Owens, *Vibrational Spectroscopy of Phase Transitions*, (Academic press, 1981).

[3] W. Hayes and R. Loudon, *Scattering of Light by Crystals*, (Dover Pulications, Inc. Mineola, New York, 1978).

[4] Blink and B. Zeks, *Soft Modes in Ferroelectrics and Anti-ferroelectrics*, (American Elsevier Publishing Company, 1974).

[5] H. Z. Cummins and P. E. Schoen, *Laser Handbook*, (North-Holland, 1972).

[6] H. Z. Cummins and A. P. Levanyuk, *Light Scattering Near Phase Transitions*, (North Holland, Amsterdam, 1983).

[7] W. Cochran, Adv. Phys. **9,** 387 (1960); **10,** 401 (1961).

[8] M. Born and K. Huang, *Dynamical Theory of Crystal Lattices*, (Oxford University Press, London, 1962).

[9] J. F. Nye, *Physical Properties of Crystals*, (Oxford University Press, London, 1957).

[10] R. Vacher and L. Boyer, Phys. Rev. B **6**, 639 (1972).

[11] I. L. Fabelinskii, *Molecular Scattering of Light*, (Plenum Press, New York, 1968).

[12] D. F. Nelson and M. Lax, Phys. Rev. B **3**, 2778 (1971).

[13] M. E. Line and A. M. Glass, *Principles and Applications of Ferroelectrics and Related Materials*, Clarendon, Oxford 1977).

[14] JRS scientific instruments *Tandem Fabry-perot Interferometer: Operating Manual*.

[15] J. R. Sandercock, *Light Scattering in Solids III: Recent Results*, (Spinger-Verlag Berlin, New York, 1982).

[16] S. Kojima, Jpn. J. Appl. Phys. **49**, 07HA01 (2010).

Chapter 3

Effect of Electric Field on Relaxor Ferroelectric 0.30Pb($Mg_{1/3}Nb_{2/3}$)O_3-0.70$PbTiO_3$ Single Crystals with Strong Random Fields

3.1 Introduction

According to the differences in frustration and randomness, there are several families of relaxor ferroelectrics (REFs) and the physical properties of each family are different from other. As for example, $Pb(Mg_{1/3}Nb_{2/3})O_3$ (PMN) does not undergo a ferroelectric phase transition due to the suppression of the percolation of polar clusters by strong random fields (RFs). While $Pb(Zn_{1/3}Nb_{2/3})O_3$ (PZN) undergoes a ferroelectric phase transition around 140 K and the long range order is observed in the ferroelectric phase. In addition, the REFs (1-*x*)$Pb(Mg_{1/3}Nb_{2/3})O_3$-*x*$PbTiO_3$ (PMN-*x*PT) are more important than (1-*x*)$Pb(Zn_{1/3}Nb_{2/3})O_3$-*x*$PbTiO_3$ (PZN-*x*PT) for the application to the piezoelectric devices. The PMN-*x*PT single crystals with ABO_3-type perovskite structure are the solid solution of relaxor PMN and normal ferroelectric $PbTiO_3$ (PT), and have been extensively studied during the last several decades owing to their exceptional piezoelectric and electromechanical responses [1-4]. From technological viewpoint, the PMN-*x*PT single crystals are very attractive and important REFs for device application and basic research, because they exhibit a great variety of physical properties which will give new insights into REFs with high efficiency that are necessary for further advanced applications. In REFs, it is suggested that the polar nanoregions (PNRs) appears due to the coupling of ferroelectric degrees of freedom such as the soft lattice mode with RFs induced by off-centering of A and B site cations [5]. It is believed that the dynamics of PNRs, which are originated at the Burns temperature T_B, play the vital role to exhibit the very high dielectric constant, piezoelectric and electromechanical coefficients of REFs. In order to clarify the role of PNRs in REFs, many theoretical and experimental investigation have been carried out [6-10]. However, the behavior of the dynamics of PNRs is still a long way to understand. The PMN-*x*PT single crystal with composition near the morphotropic phase boundary (MPB) *i.e.*, x = 30% (PMN-30PT) exhibits the maximum dielectric and piezoelectric coefficients which have a broad range of temperature dependencies [11]. These high electrical responses are extremely necessary to enhance the efficiency of the various devices such as actuators, transducers, and condensers, which require a large capacitance/mechanical strain along with the small size.

Many experimental efforts have been paid to investigate the origin of the huge electrical response of REFs near MPB compositions. The observation of stabilized monoclinic (M) symmetry [12-14] is one of the most important findings for REFs with the composition near MPB [15-18]. The importance of polarization rotation in M phases was explained by Devonshire-Landau phenomenological theory and also first-principles calculations to clarify the large electrical responses [16,17]. The compositions near the MPB, the energy states of different phases are very close to each other. As a result, different phases may coexist in a crystal and can be switched from one to another phase via polarization switching/rotations by the

application of an external electric field. Therefore, a lot of experiments have been performed on the field induced phase changes in PMN-*x*PT single crystals with compositions near the MPB. In the tetragonal (T), rhombohedral (R), and orthorhombic (O) phases, the spontaneous polarization appears along the [001], [111], and [101] directions, respectively. While in the monoclinic A (M_A), B (M_B) and C (M_C) phases, the polarization vectors appear on the (110), (100) and (010) planes, respectively [13,16,17], and can be rotated more easily than that in the R and T phases even under a small external electric field [15,18]. However in PZN-*x*PT REFs family, PZN-8%PT single crystal with composition near the MPB, a successive rotation of the spontaneous polarization was observed by applying an external electric field along the [001] direction. The spontaneous polarization of the zero-field R phase, which is directed along the [111] direction, starts to follow the polarization path to the T phase with [001] direction of polarization via an intermediate M_A phase, and after that jumps irreversibly to an alternative path of the M_C. As a result, a successive phase transition path $R \rightarrow M_A \rightarrow M_C \rightarrow T$ was observed [18]. A similar phase transition path was observed by increasing the strength of electric field along [001] direction in a zero field cooling condition of the PMN-30PT single crystal, which belongs to PMN-*x*PT REFs family. After removing the external electric field, the M_A phase was observed instead of R phase [19], while in PZN-8%PT, the M_C phase was observed which was different from the PMN-30PT [18]. However, the inhomogeneity in REFs was also discussed by multidomain states [20], the coexisting states of R and T phases [21,22], an adaptive phase consisting of nanodomains [23], and the local polarization rotation [24] to clarify the very large electrical responses. It was suggested that by applying an external electric field, the effective domain-wall size increases in the crystal with composition near the MPB, and the regions of metastable R (T) phase transforms to the thick domain walls of the stable T (R) phase in the coexisting states [21,22]. A strong negative correlation of the crystal coherence length at sub-μm scale with the electrical response was also reported [25].

In most recent, the electric field dependent measurements of REFs in relation to the critical end point (CEP) were studied, and it was suggested that the high electrical responses in REFs can be enhanced more by applying an external electric field along a certain crystallographic direction [26-28]. However, the origin of these enhancement of the physical properties is still an intriguing topic for research. Near the MPB composition, the intermediate M and O phases were observed between R and T phases of PMN-*x*PT depending on the applied field direction [19,26,27,29-32], and their influence on the acoustic properties is currently under extensive investigations [33,34]. Owing to the coupling of strain with polarization fluctuations, acoustic properties of the material show anomalous behaviors during the structural phase transitions. Brillouin scattering spectroscopy is a very powerful tool to observe the change in acoustic properties of the material by measuring the frequency shift and width of the acoustic phonons which are proportional to the sound velocity and sound attenuation, respectively.

Therefore, in present study, the acoustic and dielectric properties of PMN-30PT single crystals were investigated under zero and external dc electric field using Brillouin scattering and dielectric spectroscopy to clarify the origin of the field-induced enhancement of dielectric responses.

3.2 Experimental methods

A (001)-oriented plate of (1-*x*)Pb($Mg_{1/3}Nb_{2/3}$)O_3-*x*$PbTiO_3$ (*x* = 0.30, PMN-30PT) single crystal with 7x7 mm^2 surfaces and 0.5 mm thickness was used for measurements. In order to apply an external *dc* electric field (*E*) along the [001] direction, the gold plate electrodes were coated on larger surfaces of the crystal. Brillouin scattering spectra were measured at the back scattering geometry with mirror spacing of 2 mm and a free spectral range of 75 GHz by using a six pass Sandercock-type tandem Fabry-Perot interferometer (JRS TFP-1) with the combination of a reflection optical microscope (Olympus BX-60) [35]. As an excitation source, a diode pumped solid state (DPSS) laser such as a single frequency green Yttrium aluminium garnet (YAG) laser (Coherent Compass 315M-100) with a wavelength of 532 nm and 100mW output was used. The sample was placed inside a heating/cooling stage (Linkam HTMS600) and the temperature was controlled within a range from room temperature to 873 K with the stability of ±0.1 K.

A LCR meter (Agilent 4263B) with an external bias text fixture was used to measure dielectric constant of the sample. For the application of external dc electric field along [001] direction, a power supply (Matsusada P4K-80H) was used. The sample was placed in a home-made furnace and the temperature of the sample was controlled by a temperature controller (LakeShore 331) with a programmable dc power supply (Chroma 62012P-80-60). Before the start of every measurement, the electrodes of the sample were short-circuited at a high enough temperature for 15 min to remove any memory effect exist from the previous treatments.

3.3 Results and discussion

3.3.1 Effects of temperature

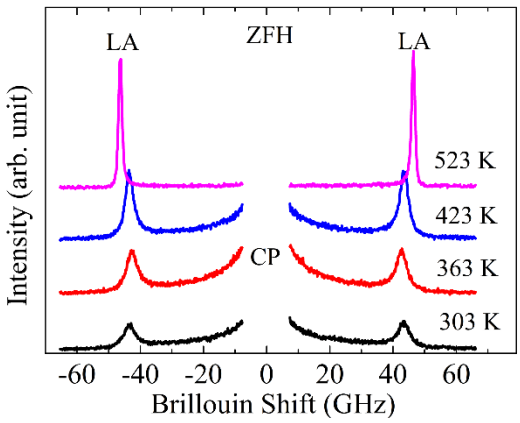

Fig. 3.1. Brillouin scattering spectra of a PMN-30PT single crystal at some selected temperatures on ZFH.

The typical Brillouin scattering spectra of the PMN-30PT single crystal at some selected temperatures on zero filed heating (ZFH) process are shown in Fig. 3.1. These spectra consist of the Brillouin peak doublet which is attributed to the scattered longitudinal acoustic (LA) phonon near the Brillouin zone center, and a central peak (CP) related to the relaxation processes. The observed Brillouin spectra were fitted by using Voigt functions, a convolution of Lorentzian and Gaussian functions where the width of the Gaussian function was fixed as an instrumental function, to obtain the Brillouin shift ν_B, the full width at half maximum (FWHM) Γ_B,

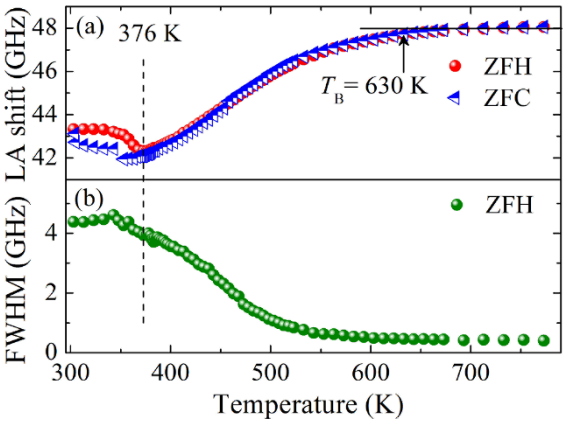

Fig. 3.2. Temperature dependences of (a) the LA shift on ZFH and ZFC and (b) the LA FWHM on ZFH.

and the peak intensity of phonon modes. Temperature dependences of ν_B and Γ_B of the LA mode were plotted in Figs. 3.2(a) and 3.2(b), respectively. The ν_B shows a clear deviation from the high temperature linear dependency near T_B = 630 K, and this acoustic anomaly is due to the appearance of dynamic PNRs which scatter the LA phonon. A significant thermal hysteresis was observed in ν_B between ZFH and zero field cooling (ZFC) processes as shown in Fig. 3.2(a), and the ν_B demonstrate a much sharper minimum at about 376 K on the ZFH, that reflecting the relaxor nature of PMN-30PT single crystal. Similar acoustic hysteresis behavior were reported in other REFs [36-41]. To confirm the relaxor nature of PMN-30PT, the temperature dependence of the relaxation time of LA mode τ_{LA} was determined from ν_B and Γ_B by using the following equation [42]:

$$\tau_{LA}=\frac{\Gamma_B-\Gamma_\infty}{2\pi\left(\nu_\infty^2-\nu_B^2\right)}\ , \tag{3.1}$$

where Γ_∞ is the background damping estimated from FWHM at the highest temperature in Fig. 3.2(b), and ν_∞ is the LA shift in the very high temperature region ($>T_B$), where it shows a linear temperature dependence.

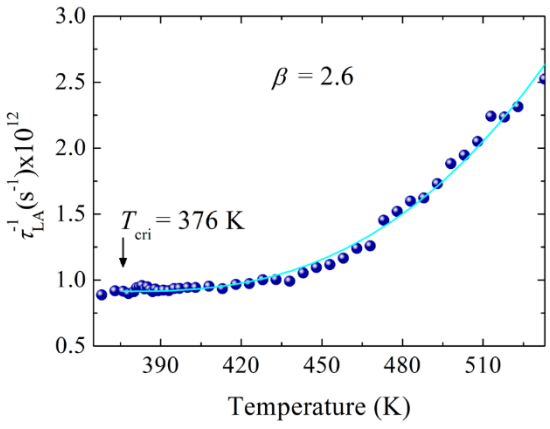

Fig. 3.3. Temperature dependence of inverse relaxation time shows the stretched slowing down of Eq. (3.2).

The inverse of τ_{LA} as a function of temperature is shown in Fig. 3.3, where the solid line represents the best fitted curve using the following equation [43]:

$$\frac{1}{\tau_{LA}}=\frac{1}{\tau_0}+\frac{1}{\tau_1}\left(\frac{T-T_C}{T_C}\right)^{\beta},\ (1\le\beta)\ \text{for}\ T>T_C\ , \tag{3.2}$$

where the stretched index $\beta = 1.0$ indicates a normal critical slowing down in the absence of RFs, while $\beta > 1.0$ indicates the stretched slowing down of the relaxation time with increase of the strength of RFs [35]. In Fig. 3.3, $\beta = 2.6$ indicates that PMN-30PT single crystal exhibits the stretched slowing down of PNRs with the presence of strong RFs.

In dielectric measurements, the clear thermal hysteresis of dielectric constants ε' and its weak frequency dependence were also observed, which signify the first order nature of the ferroelectric phase transition with the presence of RFs [44]. In Fig. 3.4(a), a deviation of the inverse dielectric constant from

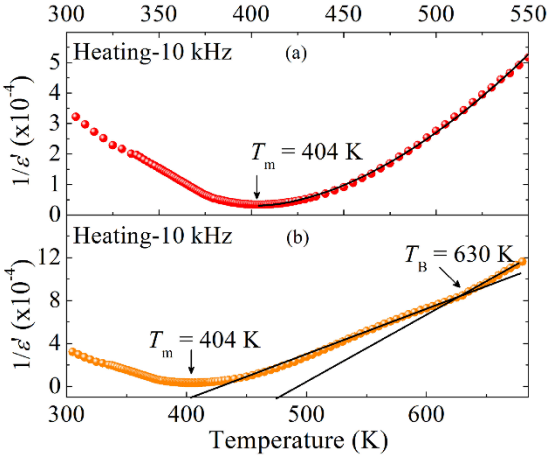

Fig. 3.4. Temperature dependence of the inverse dielectric constant at 10 kHz on ZFH.

the Curie-Weiss law, and a broad and diffused phase transition at the maximum dielectric temperature T_m = 404K were observed. Therefore, the following "extended Curie-Weiss law" [45] were used to fit the dielectric data in a paraelectric phase:

$$\frac{1}{\varepsilon} = \frac{1}{\varepsilon_m}\left[1 + \frac{(T-T_m)^\gamma}{2\delta^2}\right], (T > T_m), 1 < \gamma \le 2, \qquad (3.3)$$

where ε_m denotes the maximum dielectric constant, γ and δ represent the fitting parameters which indicating the degree of diffuseness of the phase transition. For normal ferroelectrics, the exponent $\gamma = 1$, while in case of typical REFs, $\gamma = 2$. Figure 3.4(a) shows the best-fitted curve by using Eq. (3.3), where the fitting parameters $\varepsilon_m = 32288$, $\gamma = 1.74$ and $\delta = 13.35$ were obtained. The observed value of $\gamma = 1.74$ signifies that PMN-30PT single crystal is highly relaxor with strong RFs. From Fig. 3.4(b), it was clearly observed that the inverse dielectric constant starts to deviate from its high-temperature linear dependency from 630 K which was identified as T_B in Brillouin scattering measurement. Therefore, the results obtained from dielectric measurements were consistent with Brillouin scattering measurements.

3.3.2 Effects of external electric field

3.3.2.1 Temperature dependences under constant electric field

The temperature dependence of the Brillouin scattering spectra under external *dc* E = 0.5 kV/cm and 1.0 kV/cm along the [001] direction on cooling are shown in Fig. 3.5. On cooling under E = 0.5 kV/cm,

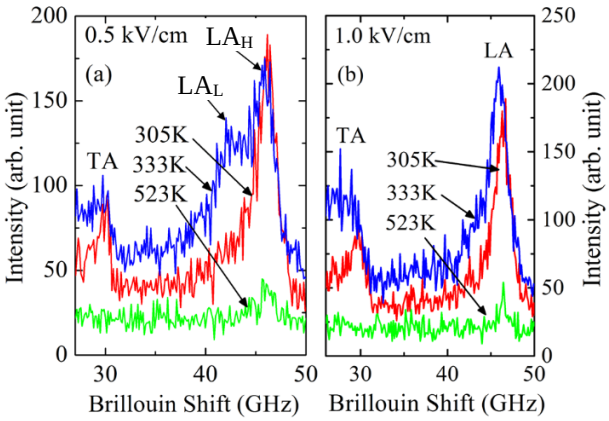

Fig. 3.5. Brillouin scattering spectra measured under (a) E = 0.5 kV/cm and (b) E = 1.0 kV/cm along the [001] direction on cooling.

a very interesting feature is that the frequency shift of the LA mode exhibits splitting below a specific temperature at about 351 K as shown in Fig. 3.5(a). Consequently, an additional weak peak of transverse acoustic (TA) mode appears at about 29 GHz. The splitting of LA mode and the appearance of TA mode clearly indicate that the PMN-30PT single crystal undergoes a ferroelectric phase transition at 351 K under E = 0.5 kV/cm. The splitting of LA mode disappears under higher electric field $E \geq$ 1.0 kV/cm as shown in Fig. 3.5(b). It indicates that under the lower E the crystal consists of two states, one is the ferroelectric macrodomain with high-frequency LA (LA_H) mode induced by external E and the other is the nanodomain state with low-frequency LA (LA_L) mode caused by RFs. Under higher E, the crystal possesses only single domain with LA_H mode, which signifies a complete switching of nanodomain to a macro/single domain states. This observation is supported by the fact that under E = 0.5 kV/cm, LA_L mode corresponds to the nanodomain state caused by RFs and its frequency shift is very similar to that of under the ZFC process. While, the frequency shift of LA_H mode under E = 0.5 kV/cm is almost similar to that of under E = 1.0 kV/cm at which the splitting of LA mode disappears by a complete switching of nanodomain into the macro/single domain states. Hence, LA_H mode corresponds to the field-induced ferroelectric macro/single domain states. Therefore, under E = 0.5 kV/cm, an incomplete switching of the nanodomain state causes the

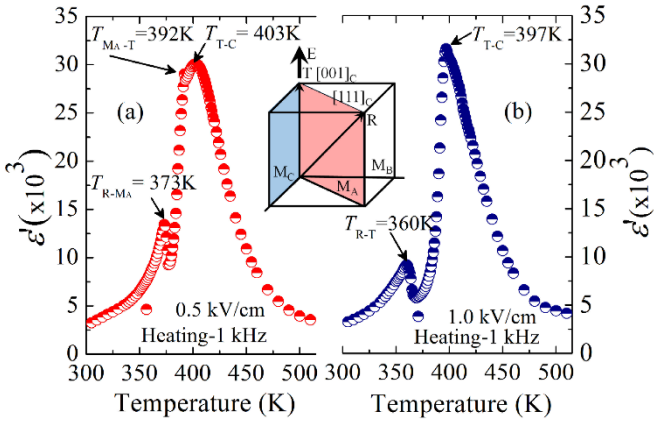

Fig. 3.6. Temperature dependence of ε' under (a) E = 0.5 kV/cm and (b) E = 1.0 kV/cm along the [001] direction on heating.

coexistence with a macrodomain state, which results the appearance of two LA modes at the same time below 351 K on cooling process. Similar phenomena were reported in PMN-17PT single crystal [36] and the strontium barium niobate, a uniaxial tungsten bronze relaxor, under the field cooling process [41,46].

Similar results were also observed in dielectric measurements. The M and T phases are absent in PMN-30PT single crystal under E = 0 [32], and the R to cubic (C) phase transition was observed at T_{R-C} = 404 K on heating. Under E = 0.5 kV/cm as shown in Fig. 3.6(a) and 0.8 kV/cm (figure not shown), the M and T phases coexist and the observed successive phase transitions become R→M_A→T→C and R→M_C→T→C, respectively [19,32]. While, under E = 1.0 kV/cm as shown in Fig. 3.6(b), the M phase disappears and the phase transition sequences R→T→C were observed [47]. This observation indicates that under the lower E the multidomain/mixed state appears by the coexistence of M and T phases. Under the higher electric field *i.e.*, $E \geq 1.0$ kV/cm, the M phase disappears and the multidomain/mixed state changes to a single domain state and the T phase becomes stable due to the complete switching of polarization from rhombohedral [111] to tetragonal [001] directions [47].

3.3.2.2 Critical end point

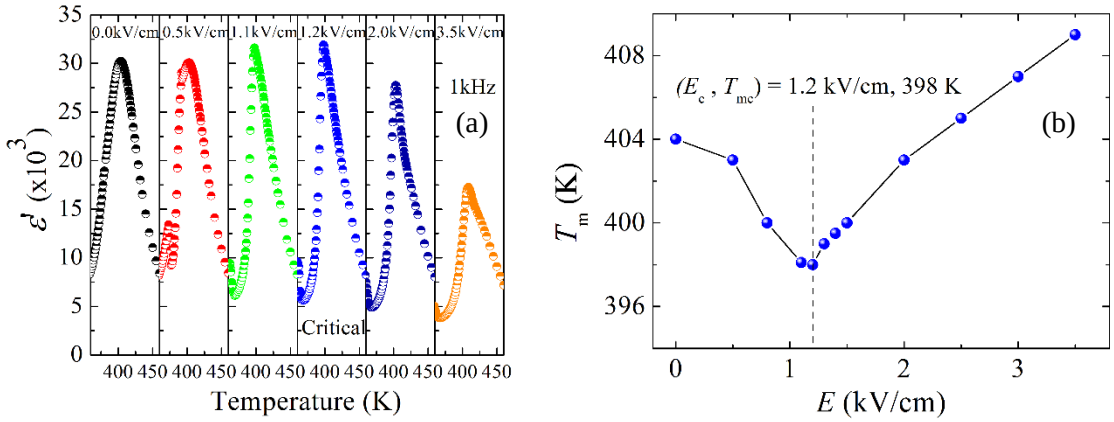

Fig. 3.7. (a)Temperature dependence of dielectric constants under various E at 1 kHz, and (b) T_m - E phase diagram of PMN-30PT single crystal.

The CEP is the upper limit of the critical E at which the energy of polarization rotation is decreased significantly [26]. At the CEP a giant electromechanical response of REFs can be observed. As shown in Fig. 3.7(a), the CEP was observed at 1.2 kV/cm and at 398 K. The highest dielectric constant was observed at the CEP, and above which the dielectric constant starts to decrease and phase transition become second order. The observed T_m–E phase diagram of the PMN-30PT single crystal is shown in Fig. 3.7(b).

In this study, below the CEP, the LA mode splitting was observed in Brillouin scattering spectra. Consequently, M and T phases appear between R and C phases in dielectric spectra. This observation signifies the existence of multidomain/mixed states. Above the CEP, the splitting of LA mode and M phase disappear, and consequently, T phase becomes stable which indicates that the multidomain/mixed states changes into the single domain state. From this result, it is clear that the CEP is the boundary line between the multidomain/mixed and single domain states. Therefore, it was suggested that at CEP, the transition

from multidomain/mixed states to a single domain state is the origin of the maximum electric responses in the PMN-30PT single crystal with the composition near the MPB [48].

3.3.2.3 Electric field dependences at constant temperature

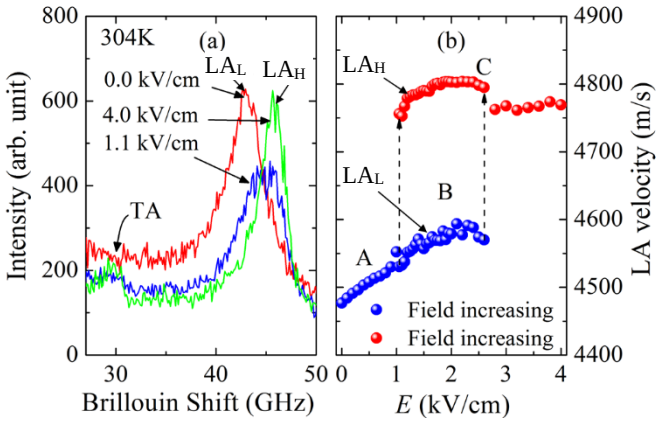

Fig. 3.8. (a) Electric field dependence of (a) Brillouin scattering spectra and (b) LA velocity at 304 K.

Figure 3.8(a) shows the electric field dependence of Brillouin scattering spectra at some selected electric fields just after ZFC and at 304 K. As shown in Fig. 3.8(b), the LA velocity (V_{LA}) was determined from ν_B using the relation $V_{LA} = \lambda \nu_B/2n_o$, where λ is the wavelength of laser light used (532 nm) and n_o is the ordinary refractive index of the crystal at λ. The reported value of n_o is 2.544 for the PMN-30PT single crystal at the wavelength of 532 nm [49]. In a ferroelectric phase below T_C, by applying external E to the ZFC crystal, a discontinuous transition of V_{LA} from a nonequilibrium nanodomain state-A induced by RFs to an intermediate state-B of coexisting nano- and macrodomains was observed at 1.05 kV/cm. With further increase of E, the state-B changes into the equilibrium state-C at 2.6 kV/cm, which mainly comprises a single domain state owing to the complete switching of nonequilibrium nanodomains into the equilibrium macro/single domain states. Similar behavior was also observed in TTB relaxor [41].

3.4 Conclusions

A remarkable thermal hysteresis between ZFH and ZFC was observed which reflects the relaxor nature of PMN-30PT single crystal. The Burns temperature $T_B = 630$ K was reported from the temperature dependences of the frequency shift of LA mode and the dielectric constant. The fitting of the temperature dependence of inverse relaxation time shows the stretched index $\beta = 2.6$, which indicates that PMN-30PT single crystal is a relaxor with strong RFs. The effect of the external dc electric field along the [001] direction was clearly observed. Under the low electric field, the splitting of LA mode was observed owing to the mixed state consisting of field-induced macrodomains and nanodomains caused by RFs. Under sufficiently high electric filed, the nonequilibrium nanodomain state changes into the equilibrium macro/single domain states. The CEP was reported at 1.2 kV/cm and at 398K which is the boundary line between the multidomain/mixed and a single domain states. At the CEP, the transition from multidomain/mixed state to

a single domain state was suggested to be the origin of the maximum electric responses in PMN-30PT single crystal with composition near the MPB. Therefore, the CEP can be a new driving mechanism for the polarization rotation and the related giant electromechanical response of REFs. The above findings can be helpful in searching for the new materials with ultrahigh performance.

References

[1] E. Sun and W. Cao, Prog. Mater. Sci. **65**, 124 (2014).

[2] S. Zhang and F. Li, J. Appl. Phys. **111**, 031301 (2012).

[3] C. Okawara and A. Amin, Appl. Phys. Lett. **95**, 072902 (2009).

[4] T. Wu, P. Zhao, M. Bao, A. Bur, J. L. Hockel, K. Wong, K. P. Mohanchandra, C. S. Lynch, and G. P. Carman, J. Appl. Phys. **109**, 124101 (2011).

[5] J. H. Ko, D. H. Kim, and S. Kojima, Phys. Rev. B **77**, 014110 (2008).

[6] B. Noheda, Z. Zhong, D. E. Cox, G. Shirane, S. -E. Park, and P. Rehrig, Phys. Rev. B. **65**, 224101 (2002).

[7] J. Hilinka, S. Kamba, J. Petzelt, J. Kulda, C. A. Randall, and S. J. Zhang, J. Phys.: Condens. Matter **15**, 4249 (2003).

[8] M. H. Kuok, S. C. Ng, H. J. Fan, M. Iwata, and Y. Ishibashi, Solid State Commun. **118**, 169 (2001).

[9] M. Iwata, H. Hoshino, H. Orihara, H. Ohwa, N. Yasuda, and Y. Ishibashi, Jpn. J. Appl. Phys. **39**, 5691 (2000).

[10] V. Bovtun, S. Veljko, M. Savinov, A. Pashkin, S. Kamba, and J. Petzelt, Ferroelectrics **318**, 179 (2005).

[11] T. R. Shrout and J. Fielding, Jr., In Proc. IEEE Ultrasonic Symp. 1990, Vol. 2, p. 711.

[12] B. Noheda, J. A. Gonzalo, L. E. Cross, R. Guo, S. -E. Park, D. E. Cox, and G. Shirane, Phys. Rev. B **61**, 8687 (2000).

[13] B. Noheda, D. E. Cox, G. Shirane, S. -E. Park, L. E. Cross, and Z. Zhong, Phys. Rev. Lett. **86**, 3891 (2001).

[14] B. Noheda, D. E. Cox, G. Shirane, J. Gao, and Z. -G. Ye, Phys. Rev. B **66**, 054104 (2002).

[15] K. Hirota, S. Wakimoto, and D. E. Cox, J. Phys. Soc. Jpn. **75**, 111006 (2006).

[16] D. Vanderbilt and M. H. Cohen, Phys. Rev. B **63**, 094108 (2001).

[17] H. Fu and R. E. Cohen, Nature **403**, 281 (2000).

[18] K. Ohwada, K. Hirota, P. W. Rehrig, Y. Fujii, and G. Shirane, Phys. Rev. B **67**, 094111 (2003).

[19] F. Bai, N. Wang, J. Li, and D. Viehland, J. Appl. Phys. **96**, 1620 (2004).

[20] S. -E. Park and T. R. Shrout, J. Appl. Phys. **82**, 1804 (1997).

[21] M. Iwata and Y. Ishibashi, Jpn. J. Appl. Phys. **52**, 09KF07 (2013).

[22] M. Iwata andY. Ishibashi, Jpn. J. Appl. Phys. **51**, 09LE03 (2012).

[23] Y. M. Jin, Y. U. Wang, A. G. Khachaturyan, J. F. Li, and D. Viehland, Phys. Rev. Lett. **91**, 197601 (2003).

[24] Y. Tomita and T. Kato, J. Phys. Soc. Jpn. **82**, 063002 (2013).

[25] D. Shimizu, S. Tsukada, M. Matsuura, J. Sakamoto, S. Kojima, K. Namikawa, J. Mizuki, and K. Ohwada, Phys. Rev. B **92**, 174121 (2015).

[26] Z. Kutnjak, J. Petzelt, and R. Blinc, Nature **441**, 956 (2006).

[27] Z. Kutnjak, R. Blinc, and Y. Ishibashi, Phys. Rev. B **76**, 104102 (2007).

[28] T. Imai, S. Toyoda, J. Miyazu, J. Kobayashi, and S. Kojima, Jpn. J. Appl. Phys. **53**, 09PB02 (2014).

[29] M. Davis, D. Damjanovic, and N. Setter, Phys. Rev. B **73**, 014115 (2006).

[30] Z. Li, Z. Xu, X. Yao, and Z. -Y. Cheng, J. Appl. Phys. **104**, 024112 (2008).

[31] X. Liu, D. Wu, B. Fang, J. Ding, X. Li, X. Zhao, H. Luo, J. –H. Ko, and C. W. Ahn, Appl. Phys. A **119**, 1469 (2015).

[32] D. Lin, Z. Li, S. Zhang, Z. Xu, and X. Yao, J. Appl. Phys. **108**, 034112 (2010).

[33] Z. -G. Ye, B. Noheda, M. Dong, D. Cox, and G. Shirane, Phys. Rev. B **64**, 184114 (2001).

[34] D. Viehland, J. F. Li, and E. V. Colla, J. Appl. Phys. **96**, 3379 (2004).

[35] S. Kojima, Jpn. J. Appl. Phys. **49**, 07HA01 (2010).

[36] T. H. Kim, S. Kojima, and J.-H. Ko, Curr. Appl. Phys. **14**, 1643 (2014).

[37] S. Tsukada, Y. Ike, J. Kano, T. Sekiya, Y. Shimojo, R. Wang, and S. Kojima, J. Phys. Soc. Jpn. **77**, 033707 (2008).

[38] M. Algueró, B. Jiménez, and L. Pardo, Appl. Phys. Lett. **87**, 082910 (2005).

[39] S. Tsukada, T. H. Kim, and S. Kojima, APL Mater. **1**, 032114 (2013).

[40] T.-H. Kim, J.-H. Ko, and S. Kojima, Jpn. J. Appl. Phys. **52**, 09KC01 (2013).

[41] K. Matsumoto and S. Kojima, Jpn. J. Appl. Phys. **54**, 10NC04 (2015).

[42] S. Tsukada and S. Kojima, Phys. Rev. B **78**, 144106 (2008).

[43] S. Kojima and S. Tsukada, Ferroelectrics **405**, 32 (2010).

[44] G. Shabbir, C. Feng, and S. Kojima, Trans. Mater. Res. Soc. Jpn. **29**, 1131(2004).

[45] Z.-Y. Cheng, R. S. Katiyar, X. Yao, and A. Guo, Phys. Rev. B **55**, 8165 (1997).

[46] J. -H. Ko, T. H. Kim, S. Kojima, K. -S. Lim, T. -Y. Koo, Appl. Phys. Lett. **99,** 212902 (2011).

[47] K.-P. Chen, X.-W. Zhang, and H.-S. Luo, J. Phys.: Condens. Matter **14**, L571 (2002).

[48] M. Aftabuzzaman and S. Kojima, Jpn. J. Appl. Phys. **55**, 07KB03 (2016).

[49] X. Wan, H. L. W. Chan, C. L. Choy, X. Zhao, and H. Luo, J. Appl. Phys. **96**, 1 (2004).

Chapter 4

Field-Induced Memory Effect of Relaxor Ferroelectric $0.30Pb(Mg_{1/3}Nb_{2/3})O_3$-$0.70PbTiO_3$ Single Crystal Studied by Dielectric Spectroscopy

4.1 Introduction

The (1-*x*)$Pb(Mg_{1/3}Nb_{2/3})O_3$-*x*$PbTiO_3$ (PMN-*x*PT) single crystals are the most attractive relaxor ferroelectrics (REFs) for technological applications and fundamental research owing to their outstanding physical properties. They demonstrate a very high values of dielectric, piezoelectric, and electromechanical coefficients [1-5], which are extremely required to reduce the size and enhance the efficiency of the various electromechanical devices such as condensers, actuators, and transducers. Therefore, during last several decades, many experimental efforts have been paid to study (PMN-*x*PT) relaxor family as a functions of temperature and external electric field to clarify the origin of these exceptional physical properties. Recently, the electric field dependent experiments on REFs in relation to the critical end point were carried out [6-9], and an increase of the above properties under electric field was reported. Upon the application of an external electric field (*E*) along the [001] direction to a (001)-oriented PMN-30PT (x = 0.30) single crystal, an intermediate monoclinic (M) phase was observed between rhombohedral (R) and field-induced tetragonal (T) phases [9-11]. However, after removing the external *E*, the M and T phases were still existed [10]. Similar behaviour were reported in other REFs $Pb[(Zn_{1/3}Nb_{2/3})_{0.92}Ti_{0.08}]O_3$ (PZN-8PT) [12]. After poling the PZN-8PT single crystal in a paraelectric phase, an internal bias field was observed on zero field cooling process, consequently an increase of the polarization in a T phase and a decrease of the T-R phase transition temperature were reported [13]. It was reported that the field cooling process actually leave a memory of dipolar defect alignment in the crystal which acts as an internal bias. This internal bias make tetragonal domains preferable with a [001] polar vector. Similar phenomena were also observed in a Ce-doped $Sr_{0.61}Ba_{0.39}Nb_2O_6$ relaxor poled in a paraelectric phase where external *E* induces a preferred orientation for polar vector that exists even after cyclic heating and cooling through phase transition temperature [14]. Based on the neutron diffuse scattering of PZN-8PT crystal, G. Xu *et al*. reported that the effect of external *E* disappears above the Curie temperature (T_C) and reappears again after zero field cooling below T_C and even persists after the extensive thermal cyclic measurements through T_C [15]. It was also speculated that the effect of *E* may be kept in memory by phonons associated with polar nanoregions (PNRs).

It is believed that dynamic PNRs induced by random fields, appear at the Burns temperature T_B, begin to grow on cooling, and a dynamic-to-static transition of PNRs occurs at the intermediate temperature T^* below which PNRs grow rapidly. By further decrease in temperature, most of the dynamic PNRs are frozen into nanodomains at T_C. When the crystal is poled above T_C, the dynamic PNRs try to be aligned along the field direction, and on subsequent cooling below T_C, PNRs can be frozen with a preferred orientation induced by the external *E*. It can also be expected that the field induced preferred orientation can exist up to T^* above which all the PNRs become dynamic. It can be speculated that there must be a relation of field-induced memory

with the dynamics of PNRs in REFs. Therefore, for the application in devices, it is extremely required to reveal the cause of this memory effect and the actual process to complete erase of this memory.

In the present study, the dielectric properties of PMN-30PT single crystal were investigated under zero and external *E* in various conditions by using the dielectric spectroscopy to clarify the origin of the field-induced memory and the process of erasing this effect.

4.2 Experimental methods

The (1-*x*)Pb($Mg_{1/3}Nb_{2/3}$)O_3-*x*$PbTiO_3$ (*x* = 0.30, PMN-30PT) single crystals with (001)-oriented plate and 0.5 mm thickness were used for the dielectric measurements. For application of external *E* along the [001] direction, gold plate electrodes were coated on the 7×7 mm^2 surfaces of the crystal. In order to measure the dielectric constant ε′, the Agilent 4263B LCR meter with an external bias text fixture was employed. The temperature of the sample was controlled in a home-made furnace by using LakeShore 331 controller along with a programmable dc power supply (Chroma 62012P-80-60). A dc power supply (Matsusada P4K-80H) was used as a source of external *E*.

4.3 Results and discussion

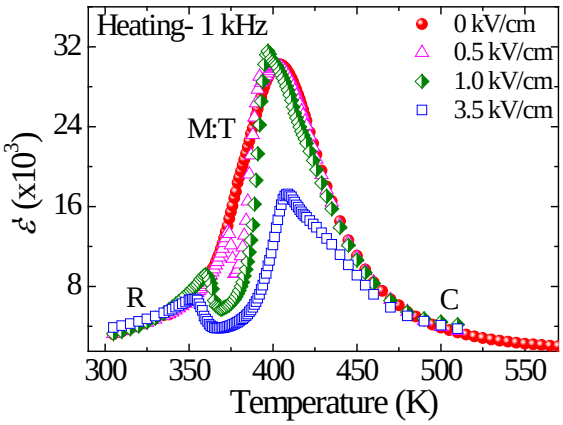

Fig. 4.1. Temperature dependences of ε′ of a PMN–30PT single crystal under constant electric fields along the [001] direction on heating.

The temperature dependent ε′ of the PMN-30PT single crystal under constant electric fields along the [001] direction on heating are shown in Fig. 4.1. For each of the measurements, a zero field cooled crystal with completely erased memory was employed. It was reported that under zero electric field, the T and M phase are absent in PMN-30PT single crystal, and the observed phase transition is R–cubic (C) at $T_{R\text{-}C}$ = 404 K on heating [9,11,16]. In temperature dependent dielectric measurements under *E* = 0.5 kV/cm, M and T phases were observed between R and C phases, and three successive phase transitions were reported at $T_{R\text{-}M}$ = 373 K, $T_{M\text{-}T}$ = 392 K and $T_{T\text{-}C}$ = 403 K on heating [9-11]. When the field strength was increased at *E* = 1.0 kV/cm and above, M phase disappeared and the observed phase transitions were R → T → C, where T phase becomes stable because of the complete switching of polarization from rhombohedral [111] to tetragonal

[001] direction [9,16]. After removing the external *E*, the observed dielectric spectra measured on ZFH were different from the initial ZFH spectra without field treatment. This fact indicates the presence of a strong memory effect of *E* in PMN-30PT single crystals.

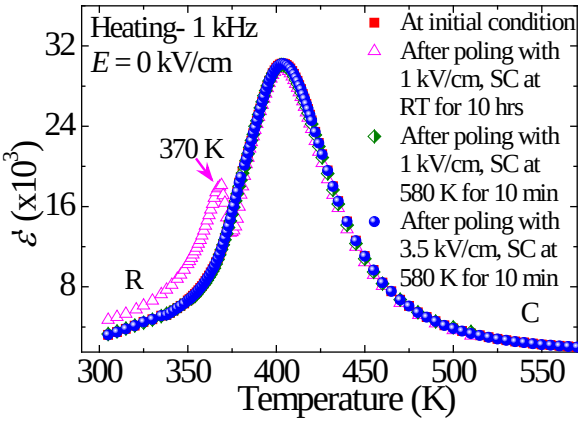

Fig. 4.2. Temperature dependences of ε′ under *E* = 0 on heating after poling the crystal and SC at different conditions.

Figure 4.2 shows the temperature dependences of ε' measured under *E* = 0 kV/cm on heating after the following processes: (1) apply *E* in a paraelectric phase, (2) cooling down to the room temperature (RT) and remove the *E*, and (3) short-circuiting (SC) the electrodes of the sample at different temperatures for different duration of time and cooling down to RT. After applying *E* = 1.0 kV/cm at 580 K and removing the field at RT, the electrodes were first short-circuited at RT for 10 hrs. An additional peak at 370 K was observed in the dielectric spectra on ZFH *i.e.*, under *E* = 0 (pink curve in Fig. 4.2) which was similar to that spectra measured under *E* = 0.5 kV/cm as shown in Fig. 4.1 (pink curve). When the external *E* is applied on the crystal at higher temperature in a paraelectric C phase and cooled down to RT, PNRs are frozen with the preferred orientation induced by the external *E* [14]. This preferred orientation of frozen PNRs can act as an internal bias field, which results the dielectric spectra similar to that of under *E* = 0.5 kV/cm. When the electrodes of the sample were short-circuited for 10 min at 580 K (close to T_B = 630 K [9]) where all PNRs become dynamic, the shape of the spectra was completely recovered [17]. Similar results were also observed when the sample was poled with higher *E* up to 3.5 kV/cm (blue curve in Fig.4.2).

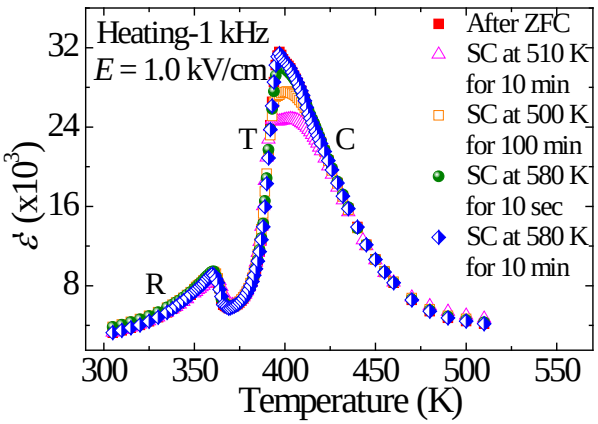

Fig. 4.3. Temperature dependences of ε′ under *E* = 1.0 kV/cm on heating after poling the crystal and SC at different conditions.

In order to clarify the correlation between memory effect and PNRs, this effect was also studied by dielectric measurements under E = 1.0 kV/cm after SC the electrodes of a poled crystal for a different duration of time in different high temperature regions as shown in Fig. 4.3. Under E = 1.0 kV/cm, a complete switching of nanodomain into the macro/single domain states was observed in Brillouin scattering measurements [9]. Therefore, E = 1.0 kV/cm is sufficient to complete switching of not only the dynamic PNRs above T_C but also nanodomains or frozen PNRs near T_C. When the electrodes were short-circuited for 10 min at 510 K which is below T^* = 523 K [9] where dynamic-static transition of PNRs starts, the shape of dielectric spectra was slightly recovered (pink curve in Fig. 4.3). When the electrodes were short-circuited at 500 K for longer period of time (100 min), the recovery of the shape of dielectric spectra was slightly enhanced (orange curve in Fig. 4.3). This observation indicates that below T^*, the field-induced memory in REFs decays with a very small rate. When the electrodes of the sample were short-circuited only for 10 sec at 580 K, the shape of dielectric spectra were almost similar to the initial zero field cooled crystal under 1.0 kV/cm.

Therefore, the following process was confirmed: after (1) applying the external E above T^*, (2) cooling down to RT, and (3) removal of the external E, all the dynamic PNRs become frozen with the preferred orientation induced by external E. As a result, after SC the electrodes of the poled sample at RT, the memory effect of E still exists. When the SC temperature increases towards T^*, the probability of the erase of memory effect also increases. Above T^*, all PNRs become dynamic and as a result, SC the electrodes above this temperature erases the preference of the previous orientation of PNRs. Therefore, the shape of the dielectric spectra is completely recovered which indicates the complete recovery from the memory effect [17]. This observation is quite important and useful not only for the field-dependent experiments on REFs but also their application in devices.

4.4 Conclusions

Dielectric properties of REFs PMN-30PT single crystals were investigated under the external electric field along the [001] direction. The strong memory effect of an electric field was observed in a field cooled crystal owing to the freezing of dynamic PNRs with a preferred orientation of polarization induced by external electric field. The decay rate of this memory effect is very slow below T^*, while it increases rapidly with the increase of the sample temperature towards T_B. A strong correlation between the memory effect and freezing of the dynamics of PNRs was observed. Short-circuiting the electrodes near T_B for a very short duration of time removes the preference of the previous orientation of PNRs, and this fact signifies the complete recovery from the field-induced memory effect. These observations provide a new insight into the REFs that can be helpful for the advancement of the device applications.

References

[1] E. Sun and W. Cao, Prog. Mater. Sci. **65**, 124 (2014).

[2] S. Zhang and F. Li, J. Appl. Phys. **111**, 031301 (2012).

[3] C. Okawara and A. Amin, Appl. Phys. Lett. **95**, 072902 (2009).

[4] T. Wu, P. Zhao, M. Bao, A. Bur, J. L. Hockel, K. Wong, K. P. Mohanchandra, C. S. Lynch, and G. P. Carman, J. Appl. Phys. **109**, 124101 (2011).

[5] S. E. Park and T. R. Shrout, J. Appl. Phys. **82**, 1804 (1997).

[6] Z. Kutnjak, J. Petzelt, R. Blinc, Nature **441**, 956 (2006).

[7] Z. Kutnjak, R. Blinc, Y. Ishibashi, Phys. Rev. B **76**, 104102 (2007).

[8] T. Imai, S. Toyoda, J. Miyazu, J. Kobayashi, S. Kojima, Jpn. J. Appl. Phys. **53**, 09PB02 (2014).

[9] M. Aftabuzzaman, S. Kojima, Jpn. J. Appl. Phys. **55**, 07KB03 (2016).

[10] F. Bai, N. Wang, J. Li, and D. Viehland, J. Appl. Phys. **96**, 1620 (2004).

[11] D. Lin, Z. Li, S. Zhang, Z. Xu, and X. Yao, J. Appl. Phys. **108**, 034112 (2010).

[12] K. Ohwada, K. Hirota, P. W. Rehrig, Y. Fujii, and G. Shirane, Phys. Rev. B **67**, 094111 (2003).

[13] M. Shen and W. Cao, Appl. Phys. Lett. **86**, 192909 (2005).

[14] T. Granzow, T. Woike, M. Wöhlecke, M. Imlau, W. Kleemann, Phys. Rev. Lett. **89**, 127601 (2002).

[15] G. Xu, P. M. Gehring, G. Shirane, Phys. Rev. B **72**, 214106 (2005).

[16] K-P. Chen, X-W. Zhang, H-S. Luo, J. Phys.:Condens. Matter **14**, L571 (2002).

[17] M. Aftabuzzaman and S. Kojima, Ferroelectrics **513**, 38 (2017).

Chapter 5

Effect of Electric Field on Acoustic Properties of Uniaxial Relaxor $Sr_{0.70}Ba_{0.30}Nb_2O_6$ Single Crystals with Strong Random Fields

5.1 Introduction

Most of the perovskite relaxors such as $Pb(Mg_{1/3}Nb_{2/3})O_3$ (PMN), $(1\text{-}x)Pb(Mg_{1/3}Nb_{2/3})O_3\text{-}xPbTiO_3$ (PMN-*x*PT), $Pb(Zn_{1/3}Nb_{2/3})O_3$ (PZN), $(1\text{-}x)Pb(Zn_{1/3}Nb_{2/3})O_3\text{-}xPbTiO_3$ (PZN-*x*PT), and $Pb(Sc_{1/2}Ta_{1/2})O_3$ are Pb-based and have been extensively studied owing to their great variety of physical properties which are suitable in a wide range of technological applications. Although the Pb-based relaxor ferroelectrics (REFs) demonstrate excellent physical properties, they contain Pb which may affect the natural environment because of its toxicity. Therefore, from the environmental point of view, the development of Pb-free REFs is now indispensable matter in applied physics. Due to the emerging demand of Pb-free materials in green sustainable technology, a great interest of the research on Pb-free materials has been growing.

Uniaxial RFEs with tetragonal tungsten bronze (TTB) structure such as $Sr_xBa_{1-x}Nb_2O_6$ (SBN) are Pb-free and fascinating materials for technological applications and fundamental research because they demonstrate markedly effective dielectric, piezoelectric, pyroelectric, and photorefractive properties [1-8]. These colossal physical properties of TTB relaxors are extremely essential for applications in modern devices such as sensors, data storage [4,7,9-12] lasers, and holography [13,14]. The unique combination of outstanding physical features, uniaxial spontaneous polarization and Pb-free nature provides SBN single crystals an extra dimension of research interest. However, most of the REFs with TTB structure are Pb-free, but till now the detail study on these REFs is not sufficient and the understanding of their insight mechanism is still unclear.

Up to the present, many experiments have been carried out on uniaxial TTB REFs to discuss their different structural features, functional properties, origin of the relaxor nature and its composition dependence. The relaxor nature of SBN61 (x = 0.61) was studied by using Brillouin scattering, dielectric and pyroelectric measurements, and from nonlinear dielectric responses, the growth of polar nanoregions (PNRs) into the long-range ferroelectric domains was reported near and below the Curie temperature T_C [15-17]. The appearance of quasistatic PNRs near T_C in a paraelectric phase was reported by piezoresponse force microscopy (PFM) and Raman scattering experiments [15-19]. The existence of characteristic temperatures namely, Burns temperature T_B and intermediate temperature T^* of SBN75 (x = 0.75) were confirmed by acoustic emission experiments, and the effect of external electric field on the ferroelectric phase transition temperature was reported [20]. The electric field-induced orthorhombic phase was also identified within a modulated incommensurate tetragonal structure of SBN75 by low-temperature acoustic emission [21]. The single domain state induced by the electric field and its spontaneous back switching were observed in SBN61 by using Brillouin scattering spectroscopy and PFM [22,23]. Recently, an automated electron diffraction tomography with beam precession was employed to confirm the room-temperature tetragonal symmetry of SBN and $Ca_xBa_{1-x}Nb_2O_6$ (CBN) single crystals [24]. The dielectric response of

SBN81 (x = 0.81) single crystals were studied in a wide frequency range of 10^3 to 10^{13} Hz, and several relaxations corresponding to the fast polarization mechanisms below the phonon frequencies were observed which play the vital role in the dielectric response of the crystal [25]. It was also reported that the main contribution to the dielectric permittivity comes from a strong relaxation present in a GHz range at high temperature region, which slows down on cooling. The stability of ferroelectric domain patterns induced by local electric fields in pure and Ce-doped SBN61 and SBN75 were reported by PFM [26]. However, the detail study of the effect of external electric field on acoustic properties of TTB REFs in relation to the dynamics of PNRs is even now insufficient, and under external electric field, the role of PNRs in the states above and below T_C is still an unsolved issue of materials science.

Therefore, in the present study, the acoustic properties of SBN70 single crystals with strong RFs were investigated by using Brillouin scattering spectroscopy as functions of temperature and external electric field to clarify the critical nature and related functionality of PNRs above and below T_C.

5.2 Experimental methods

$Sr_xBa_{1-x}Nb_2O_6$ (x = 0.70, SBN70) single crystals were grown by the Czochralski method [27]. A (001)-oriented plate (c-plate) crystals with 5 × 5 mm^2 surfaces and 1 mm thickness were used for experiments, where the surfaces of the crystal were polished to optical quality. For the application of an external dc electric field along the [001] direction, silver paste electrodes were coated on larger surfaces and a hole of 1 mm radius was created on one of the surfaces of the crystal for entering the laser beam. A Brillouin scattering system with a high-contrast six pass Sandercock-type tandem Fabry-Perot interferometer (JRS TFP-1) combining with of a reflection optical microscope (Olympus BX-60) was employed to measure the Brillouin spectra in a back scattering geometry with a mirror spacing of 2 mm and a free spectral range of 75 GHz [28]. For excitation source, a single frequency green Yttrium aluminium garnet (YAG) laser (Coherent Compass 315M-100) with output power of 100mW and wavelength of 532 nm was used. In order to control the temperature of the sample a heating/cooling stage (Linkam THMS600) with a stability of ± 0.1°C was used. Prior to the each measurement, electrodes of the sample were short-circuited and heated for 30 min at a sufficiently high temperature to remove any memory effect of electric field retained from previous treatments.

5.3 Results and discussion

5.3.1 Effects of temperature

The typical Brillouin scattering spectra of a c-plate SBN70 single crystal measured in the $c(a,a+b)\bar{c}$ scattering geometry at some selected temperatures on zero field heating (ZFH) process are shown in Figure 5.1(a). The observed scattering intensity vs temperature and frequency shift was plotted in a contour map as shown in Fig. 5.1(b), where the elastic scattering was removed in the vicinity of 0 GHz. The obtained Brillouin spectra consist of the Brillouin peak doublets which correspond to the scattered longitudinal acoustic (LA) and

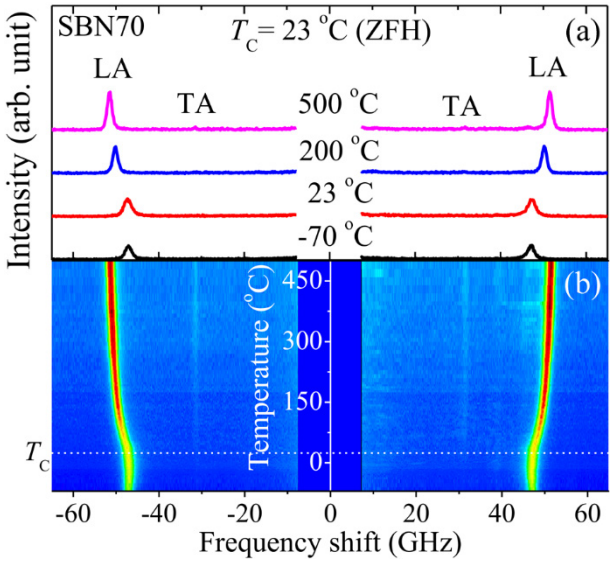

Fig. 5.1. (a) Brillouin scattering spectra of a *c*-plate SBN70 single crystal at some selected temperatures on ZFH. (b) Contour map of the scattering intensity vs temperature and LA frequency shift (red and blue colors indicate the high and low intensities, respectively). The elastic scattering near 0 GHz was removed.

transverse acoustic (TA) phonon modes near the center of Brillouin zone. It was clearly observed that a very weak TA peak persists in the entire temperature range of -70 to 500 °C as shown in Figs. 5.1(a) and 5.1(b). According to the selection rules, the TA mode is forbidden in backward scattering geometries for the tetragonal 4*mm* or 4/*mmm* point group except in the $c(ab)\bar{c}$ scattering geometry [15], that is included in the $c(a,a+b)\bar{c}$ geometry. Therefore, the presence of the TA mode above and below T_C observed in the $c(a,a+b)\bar{c}$ geometry signifies that SBN70 single crystals belong to tetragonal symmetry in both the high-temperature paraelectric and low-temperature ferroelectric phases. To obtain the frequency shift ν_B, full width at half maximum (FWHM) Γ_B and peak intensity of the phonon modes, the measured Brillouin spectra were fitted by Voigt functions, which are convolutions of Lorentzian and Gaussian functions where the Gaussian function

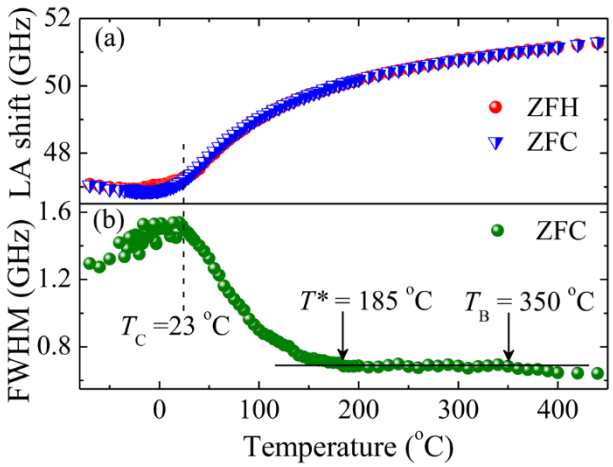

Fig. 5.2. Temperature dependences of (a) the LA shift on ZFH and ZFC and (b) the LA FWHM on ZFC.

was fixed as an instrumental function. The temperature dependence of ν_B and FWHM of the LA mode obtained from fitting were plotted in Figs. 5.2(a) and 5.2(b), respectively. In Fig. 5.2(a), a marked diffuseness

was observed in the LA shift near T_C on both ZFH and zero field cooling (ZFC) processes. In addition, a remarkable thermal hysteresis in the LA shift between ZFH and ZFC was also observed below T_C. These results signify that SBN70 single crystals undergo a diffused ferroelectric phase transition because of the incomplete switching of nanodomains caused by the presence of strong quenched random fields (RFs) on ZFC. Similar acoustic phenomena were also observer in other typical REFs [22,29-32].

The acoustic properties such as sound velocity and sound attenuation become very sensitive at the characteristic temperatures of PNRs and show anomalous behavior via the scattering of LA phonons by PNRs [33]. Therefore, FWHM of the LA mode was measured as a function of temperature in a wide range of temperature between -70 and 500 ºC on ZFC as shown in Fig. 5.2(b), which is proportional to the sound attenuation. From Fig. 5.2(b), upon cooling from high temperature, a deviation of FWHM from its linear temperature dependence in the high-temperature region was observed near 350 ºC because of the nucleation of dynamic PNRs that scatter the LA phonons and result in an increase of the LA width. Upon further cooling, a rapid increase in the LA width was also observed below 185 ºC owing to the start of dynamic-to-static transition of PNRs, where the scattering of LA phonons by these static PNRs dominates [34]. Subsequently at T_C, most of the PNRs become static/frozen within a ferroelectric nanodomain state. As a result, the increase in the scattering of LA phonons by PNRs is stopped at T_C. Therefore, the characteristic temperatures of PNRs correspond to the SBN70, *i.e.*, T_B = 350 ºC, T^* = 185 ºC, and T_C = 23 ºC, were determined from the temperature dependence of the LA width on ZFC as shown in Fig. 5.2(b) [35]. It was interesting that, the obtained T_B and T^* were similar to those of SBN61 and SBN75 [20,22], and seem to be common for all possible compositions of SBN. A similar composition-independent behavior of T_B and T^* was also reported in other Pb-based relaxor with perovskite structure [36]. In order to confirm the relaxor nature of SBN70, the temperature dependence of the relaxation time of LA mode τ_{LA} was estimated from ν_B and Γ_B by using the following equation [37]:

$$\tau_{LA}=\frac{\Gamma_B-\Gamma_\infty}{2\pi\left(\nu_\infty^2-\nu_B^2\right)}, \tag{5.1}$$

where Γ_∞ is the background damping determined from FWHM at the highest temperature in Fig. 5.2(b),

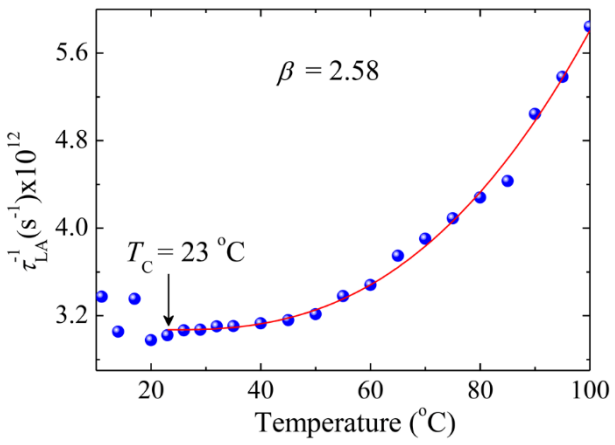

Fig. 5.3. Temperature dependence of inverse relaxation time obeys the stretched slowing down.

and ν_∞ is the LA shift in the very high temperature region ($>T_B$), where a linear temperature dependence of ν_B is observed. The temperature dependence of the inverse of τ_{LA} is shown in Fig. 5.3, where the solid line shows the best fitted curve using the following equation [38]:

$$\frac{1}{\tau_{LA}} = \frac{1}{\tau_0} + \frac{1}{\tau_1}\left(\frac{T-T_C}{T_C}\right)^{\beta}, (1 \le \beta) \text{ for } T > T_C, \qquad (5.2)$$

where the exponent $\beta = 1.0$ corresponds to a normal critical slowing down in the absence of RFs, and $\beta > 1.0$ corresponds to the stretched slowing down of relaxation time with the increased strength of RFs [28]. After fitting of the data shown in Fig. 5.3, $\beta = 2.58$, $\tau_0 = 0.33$ ps, and $\tau_1 = 8.3$ ps were obtained, which indicate the stretched critical slowing down of PNRs, and such a high value of β indicates that SBN70 single crystal is a relaxor with strong RFs. The typical value of $\beta = 3.0$ was reported for the Pb-based relaxor PZN-7PT [38].

5.3.2 Effects of external electric field

The LA velocity (V_{LA}) was calculated from ν_B by using the relation $V_{LA} = \lambda \nu_B / 2n_o$, where λ and n_o are the wavelength of laser light used (532 nm) and the ordinary refractive index of the crystal at λ, respectively. For SBN70 single crystal, $n_o = 2.359$ at $\lambda = 532$ nm was reported [39]. Since nanodomains in REFs are very sensitive to the external electric field (E), the related anomalies of V_{LA} can be expected from its temperature dependence under the external field. The temperature dependences of V_{LA} under $E = 0$ and 2.0 kV/cm dc field along the [001] direction on heating and cooling processes are shown in Figure 5.4. On

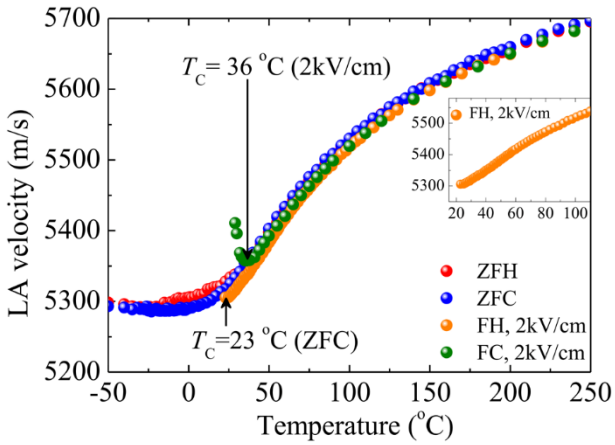

Fig. 5.4. Temperature dependences of LA velocity of a SBN70 single crystal under $E = 0$ and 2 kV/cm along the [001] direction on heating and subsequent cooling.

field heating (FH) from 23 ºC under $E = 2.0$ kV/cm, no anomaly was observed in V_{LA} as shown in the inset of Fig. 5.4. The temperature dependence of V_{LA} under $E = 2.0$ kV/cm shows a similar fashion to that of ZFH curve (red curve in Fig. 5.4) with a small decrease in magnitude. On subsequent continuous field cooling (FC) from 250 ºC under the same E, T_C (=23 ºC) was shifted to 36 ºC, below which a marked increase of V_{LA} was observed as shown in the olive curve of Fig. 5.4. This anomaly of V_{LA} was due to a complete suppression of RFs by an external electric field on cooling from the high-temperature region, and hence

forming macro/single domains in the ferroelectric phase. The most of PNRs become static/frozen in a low-temperature ferroelectric phase and a glass-like nonergodic state is formed by RFs [40], while in a high-temperature paraelectric phase below T^*, the most of PNRs are quasistatic and interaction between themselves is very weak. Therefore, E = 2.0 kV/cm is not sufficient to align nanodomains on FH in a ferroelectric phase, whereas the same E can easily align most of the quasistatic PNRs along the field direction in a paraelectric phase. On first FH under E = 3.0 kV/cm as shown in the inset of Fig. 5.5, a rapid

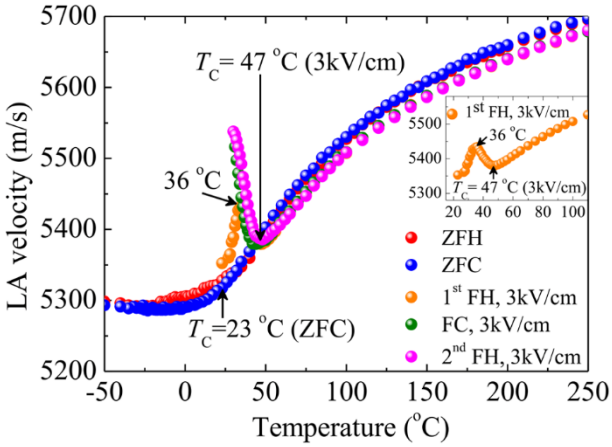

Fig. 5.5. Temperature dependences of LA velocity of a SBN70 single crystal under E = 0 and 3 kV/cm along the [001] direction.

increase of V_{LA} was observed and a sharp peak was found at about 36 ºC owing to a complete switching/alignment of nanodomains into a field-induced macro/single domain state. Beyond the maximum, a marked decrease of V_{LA} was observed towards T_C. By increasing the strength of E to 3.0 kV/cm, T_C was shifted towards a higher value (47 ºC), at which a sharp minimum of V_{LA} was observed. This indicates that by applying the external E, the long-range ferroelectric order is enhanced and therefore T_C shifts towards the higher value. On subsequent continuous FC and second FH under E = 3.0 kV/cm (olive and magenta curves in Fig. 5.5, respectively), the observed minima of V_{LA} were identical to that of the first FH process, whereas the anomaly of V_{LA} at 36 ºC was absent. Consequently, a marked decrease of diffuseness of the phase transition and remarkable increase of V_{LA} were observed in the ferroelectric phase owing to the complete suppression of nanodomains by the external E during the previous FH process. From Figs. 5.4 and 5.5, it was clearly seen that, by increasing the strength of E, the suppression of V_{LA} was enhanced in the paraelectric phase. Obviously, the quasistatic PNRs in a paraelectric phase are also aligned and stabilized by the strong E. As a result, the electrostrictive coupling between the local polarization of PNRs and the strain becomes stronger and therefore, V_{LA} becomes smaller than those on ZFH and ZFC above T_C under strong E. When the strength of E decreases, the difference in V_{LA} also decreases.

By applying an external E to a ZFC crystal near T_C along the ferroelectric c-axis, *i.e.*, along the [001] direction, a splitting of the LA mode was observed at 3.4 kV/cm as shown in Fig. 5.6. As a result, a discontinuous transition of V_{LA} from a nonequilibrium nanodomain state induced by quenched RFs to an intermediate/mixed state with coexisting nano- and macrodomains was observed. Where, the low-frequency

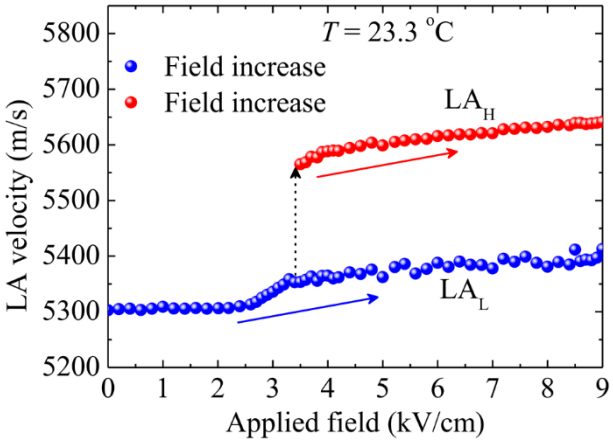

Fig. 5.6. Electric field dependence of LA velocity at 23.3 ºC.

LA (LA_L) mode corresponds to the nanodomain state induced by quenched RFs and the high-frequency LA (LA_H) mode corresponds to the macrodomain state induced by the external *E*. Due to the existence of strong RFs, this coexisting state persists up to 9.0 kV/cm by an incomplete switching of the nonequilibrium nanodomain into the equilibrium macro/single domain states. A similar phenomena were also reported in the CBN30 single crystal [41].

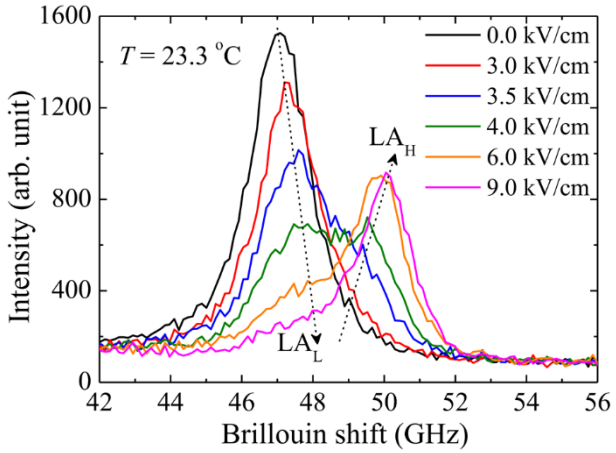

Fig. 5.6. Electric field dependence of Brillouin scattering spectra of the LA mode at 23.3 ºC.

Figure 5.7 shows the electric field dependence of Brillouin scattering spectra of the LA mode of a SBN70 single crystal at some selected electric fields at 23.3 ºC. By increasing *E* from zero to 3.4 kV/cm, a gradual decrease in the intensity of the LA_L mode was observed, consequently, another peak of the LA_H mode was appeared at a higher frequency. The intensities of the LA_L and LA_H modes are related to the volumes of nonodomain and macrodomain states, respectively. The intensities of both peaks become equal at *E* = 4.0 kV/cm, indicating that the volumes of nanodomain and macrodomain states are nearly equal. Upon further increase of *E*, the peak of the LA_H mode dominates and the double-peak state persists up to *E* = 9.0 kV/cm, while the peak of the LA_L mode does not disappear completely owing to the incomplete switching of nanodomains caused by strong quenched RFs. After removing the external *E*, the double-peak state still persists, but this strong memory effect of *E* can be erased by short-circuiting the electrodes of the sample and heating above *T** for more than 30 min.

5.4 Conclusions

The effects of temperature and external electric field on the acoustic properties of a SBN70 single crystal with strong RFs were studied by using Brillouin scattering spectroscopy. A marked diffuseness of the ferroelectric phase transition was observed on both ZFH and ZFC, and a remarkable thermal hysteresis between ZFH and ZFC was also observed near T_C, which signifies the relaxor nature of the SBN70 single crystal. The characteristic temperatures of PNRs in SBN70 single crystal, namely, T_B = 350 ºC, T^* = 185 ºC, and T_C = 23 ºC, were identified from the temperature dependence of the LA width on ZFC. A stretching exponent β = 2.58, observed from the fitting of temperature dependence of the inverse relaxation time, indicates that the SBN70 single crystal exhibits a stretched critical slowing down of PNRs owing to the presence of strong RFs. The effect of an external electric field along the [001] direction was clearly observed. On FH under 3.0 kV/cm, a complete alignment of nanodomains and enhancement of the long-range ferroelectric order were observed below T_C. Under sufficiently strong electric field, the alignment and stabilization of quasistatic PNRs in a paraelectric phase were also observed. In the field-dependent measurements in a ferroelectric phase, a mixed state consisting of macro- and nanodomains was observed at 3.4 kV/cm. The mixed state was observed up to 9.0 kV/cm owing to the incomplete switching of nanodomains being stabilized by strong RFs into the macro/single domain states. After removing the external electric field, a strong field-induced memory effect was also observed; such a memory effect can be erased by short-circuiting the electrodes of the sample and heating above T^* for more than 30 min.

References

[1] J. R. Oliver, R. R. Neurgaonkar, and L. E. Cross, J. Appl. Phys. **64**, 37 (1988).

[2] W. H. Huang, D. Viehland, and R. R. Neurgaonkar, J. Appl. Phys. **76**, 490 (1994).

[3] R. R. Neurgaonkar, W. F. Hall, J. R. Oliver, W. W. Ho, and W. K. Cory, Ferroelectrics **87**, 167 (1988).

[4] A. M. Glass, J. Appl. Phys. **40**, 4699 (1969).

[5] B. Fischer, M. Cronin-Golomb, J. O. White, A. Yariv, and R. Neurgaonkar, Appl. Phys. Lett. **40**, 863 (1982).

[6] R. R. Neurgaonkar, W. K. Cory, J. R. Oliver, M. D. Ewbank, and W. F. Hall, Opt. Eng. **26**, 265392 (1987).

[7] F. Kahmann, J. Höhne, R. Pankrath, and R. A. Rupp, Phys. Rev. B **50**, 2474 (1994).

[8] M. Wesner, C. Herden, R. Pankrath, D. Kip, and P. Moretti, Phys. Rev. E **64**, 036613 (2001).

[9] R. Blinc, Advanced Ferroelectricity (Oxford University Press, Oxford, U.K., 2011) International Series of Monographs on Physics, Vol. 151, p. 144.

[10] A. M. Glass, Appl. Phys. Lett. **13**, 147 (1968).

[11] M. H. Francombe, Acta Crystallogr. **13**, 131 (1960).

[12] W. Kleemann, J. Dec, V. V. Shvartsman, Z. Kutnjak, and T. Braun, Phys. Rev. Lett. **97**, 065702 (2006).

[13] M. O. Ramírez, D. Jaque, L. E. Bausá, J. G. Solé, and A. A. Kaminskii, Phys. Rev. Lett. **95**, 267401 (2005).

[14] Y. Qiao, S. Orlov, D. Psaltis, and R. R. Neurgaonkar, Opt. Lett. **18**, 1004 (1993).

[15] F. M. Jiang, J. -H. Ko, and S. Kojima, Phys. Rev. B **66**, 184301 (2002).

[16] J. -H. Ko, S. Kojima, S. Lushnikov, R. S. Katiyar, T. -H. Kim, and J. -H. Ro, J. Appl. Phys. **92**, 1536 (2002).

[17] J. -H. Ko and S. Kojima, Jpn. J. Appl. Phys. **41**, 7038 (2002).

[18] V. V. Shvartsman, W. Kleemann, T. Łukasiewicz, and J. Dec, Phys. Rev. B **77**, 054105 (2008).

[19] S. Shin, T. H. Kim, J. -H. Ko, S. Kojima, K. -S. Lim, and T. -Y. Koo, Ferroelectrics **488**, 1 (2015).

[20] E. Dul'kin, S. Kojima, and M. Roth, J. Appl. Phys. **110**, 044106 (2011).

[21] E. Dul'kin, S. Kojima, and M. Roth, J. Appl. Phys. **111**, 084101 (2012).

[22] K. Matsumoto and S. Kojima, Jpn. J. Appl. Phys. **54**, 10NC04 (2015).

[23] E. A. Kolchina, M. M. Neradovskiy, V. A. Shikhova, D. V. Pelegov, V. Ya. Shur, L. I. Ivleva, and J. Dec, Ferroelectrics **496**, 149 (2016).

[24] J. Wspaniała-Rak, M. Zubko, D. Stróz, J. Rak, and J. Dec, Acta Phys. Pol. A **130**, 830 (2016).

[25] E. Buixaderas, C. Kadlec, M. Kempa, V. Bovtun, M. Savinov, P. Bednyakov, J. Hlinka, and, J. Dec, Sci. Rep. **7**, 18034 (2017).

[26] V. Ya. Shur, V. A. Shikhova, D. O. Alikin, V. A. Lebedev, L. I. Ivleva, J. Dec, D. C. Lupascu, and V. V. Shvartsman, Sci. Rep. **7**, 125 (2017).

[27] T. Łukasiewicz, M. A. Swirkowicz, J. Dec, W. Hofman, and W. Szyrski, J. Cryst. Growth **310**, 1464 (2008).

[28] S. Kojima, Jpn. J. Appl. Phys. **49**, 07HA01 (2010).

[29] S. Tsukada, T. H. Kim, and S. Kojima, APL Mater. **1**, 032114 (2013).

[30] T. H. Kim, J. -H. Ko, and S. Kojima, Jpn. J. Appl. Phys. **52**, 09KC01 (2013).

[31] T. H. Kim, S. Kojima, and J. -H. Ko, Curr. Appl. Phys. **14**, 1643 (2014).

[32] M. Aftabuzzaman and S. Kojima, Jpn. J. Appl. Phys. **55**, 07KB03 (2016).

[33] J. -H. Ko, T. H. Kim, S. Kojima, K. -S. Lim, and T. -Y. Koo, Appl. Phys. Lett. **99**, 212902 (2011).

[34] K. Suzuki, K. Matsumoto, J. Dec, T. Łukasiewicz, W. Kleemann, and S. Kojima, Phys. Rev. B **90,** 064110 (2014).

[35] M. Aftabuzzaman, M. A. Helal, J. Dec, W. Kleemann, and S. Kojima, Jpn. J. Appl. Phys. **56**, 10PC06 (2017).

[36] M. Roth, E. Mojaev, E. Dul'kin, P. Gemeiner, and B. Dkhil, Phys. Rev. Lett. **98**, 265701 (2007).

[37] S. Tsukada and S. Kojima, Phys. Rev. B **78**, 144106 (2008).

[38] S. Kojima and S. Tsukada, Ferroelectrics **405**, 32 (2010).

[39] J. -H. Ko, T. H. Kim, S. Kojima, K. -S. Lim, and T. -Y. Koo, J. Adv. Dielectr. **1**, 91 (2011).

[40] W. Kleemann, J. Dec, and S. Miga, Phase Transitions **88**, 234 (2015).

[41] M. Aftabuzzaman, J. Dec, W. Kleemann, and S. Kojima, Jpn. J. Appl. Phys. **55**, 10TC01 (2016).

Chapter 6

Electric Field and Aging Effects of Uniaxial Ferroelectric $Sr_{0.40}Ba_{0.60}Nb_2O_6$ with Weak Random Fields Studied by Brillouin Scattering

6.1 Introduction

Static and dynamic heterogeneity of disordered system is one of the present topics in materials science. In disordered ferroelectric materials with random fields (RFs) called relaxor ferroelectrics (REFs), the relaxor nature is characterized by RFs-induced polar nanoregions (PNRs) which play the dominant role in the precursor phenomena of a ferroelectric phase transition. On cooling from high temperature, the dynamic PNRs are induced at the Burns temperature T_B due to the fluctuations of RFs. Upon further cooling from T_B, the size of PNRs begins to grow and a dynamic-to-static transition of PNRs takes place at the intermediate temperature T^*, below which a rapid growth of PNRs is observed. Therefore, it is considered that in REFs, the dynamics of PNRs play the vital role in the relaxor behaviors by inducing the diffusive and frequency-dispersive dielectric anomalies and various precursor phenomena [1,2]. At the Curie temperature T_C where the paraelectric-to-ferroelectric phase transition take place, most of the PNRs become frozen into a nonequilibrium nanodomain state, and consequently, RFs prevent the growth into macrodomains [3]. However, during an aging process of uniaxial tetragonal tungsten bronze (TTB) relaxors below T_C, the nonequilibrium nanodomain state gradually transforms into a metastable macrodomain state with opposite direction of the spontaneous polarization [4,5]. After several years of aging below T_C, a stable/equilibrium macrodomain or even a single domain state can be obtained [3].

Aging is a common observed phenomenon in all disordered systems such as super-cooled liquids, polymers spin glasses, and REFs [6]. After several hours aging of a highly disordered relaxor $Sr_xBa_{1-x}Nb_2O_6$ (x = 0.75, SBN75) with strong RFs, the rejuvenation and memory effects were observed in the susceptibility components, which indicate the possible glassy nature of the low-temperature ground state of REFs [7,8]. The compositional inhomogeneity in the nanoscale regions of these crystals induces RFs, which cause a diffused phase transition and the formation of nanodomain state below T_C, while the growth into the macro/single domain state is prevented by RFs [3]. However, by the application of an external electric field, the single domain state was observed in SBN61 (x = 0.61) single crystal [3,9]. Recently, SBN70 (x = 0.70) and $Ca_xBa_{1-x}Nb_2O_6$ (x = 0.30, CBN30) single crystals were studied by Brillouin scattering under an external dc electric field [10,11]. Under the external field, an incomplete alignment of nanodomains and enhancement of the long-range ferroelectric order were observed in a ferroelectric phase. It was also reported that a coexisting state of nanodomains and macrodomains persists up to a high electric field owing to the incomplete switching/alignment of nanodomains. However, the exact reason of this incomplete switching/alignment of nanodomains below T_C is still unclear.

The nanodomain state below T_C of ferroelectric materials is very sensitive to the external electric field and aging by which it gradually switches into the metastable macrodomain state. Therefore, the

acoustic properties of materials such as sound velocity and sound attenuation are affected. The Brillouin scattering spectroscopy is a powerful and advanced tool to determine the frequency shift and width of acoustic phonon modes which are proportional to the sound velocity and sound attenuation in materials, respectively. Therefore, the use of Brillouin scattering spectroscopy is a new approach of experimental technique to study the effects of external electric field and aging in ferroelectric materials. RFs always try to stabilize the nanodomain state by preventing the formation of macrodomains [3], therefore, the stability of the nanodomain state mainly depends on the strength of RFs. The SBN40 single crystal is a suitable material to study the switching/alignment of nanodomain state below T_C owing to its uniaxial nature of the spontaneous polarization and the presence of weak RFs which can be suppressed by applying a small amount of external electric field.

Therefore, in this study, the acoustic properties of SBN40 single crystals were investigated under zero and externally applied dc electric field by using the Brillouin scattering spectroscopy to clarify the critical nature and related functionality of PNRs and domain states in a ferroelectric phase below T_C. In addition, experiments on aging below T_C and its temperature dependence were also conducted which will give more insights into the understanding of microscopic nature of the domain state in a ferroelectric phase.

6.2 Experimental methods

The Czochralski method [12] was used to grow $Sr_xBa_{1-x}Nb_2O_6$ (x = 0.40, SBN40) single crystals. The *c*-plate crystals with 5 × 5 mm^2 surfaces, which were polished to optical quality, and 1mm thickness were used for measurements. Silver plate electrodes were coated on the larger surfaces of the crystal with a hole of 1 mm radius on one of the surfaces to apply an external dc electric field along the [001] direction *i.e.*, along the crystallographic *c*-direction. Brillouin scattering spectra were measured in back scattering geometry using a high-contrast six (3 + 3) passes Sandercock-type tandem Fabry–Perot interferometer (JRS TFP-1) with combination of an optical microscope (Olympus BX-60) and a single frequency green yttrium aluminium garnet (YAG) laser (Coherent Compass 315M-100) which have a wavelength of 532 nm and output power of 100mW [13]. The mirror spacing and free spectral range were fixed at 2 mm and 75 GHz, respectively. Temperature of the sample was controlled by a Linkam THMS600 heating/cooling stage which has a stability of ± 0.1 °C. Before the start of each experiment, the electrodes of the crystal were short-circuited for 10 min at a high enough temperature to erase any memory effect of external field retained from previous experiments.

An X-ray Bond method [14] with an uncertainty as low as of the order of $\Delta d/d = 10^{-5}$ was used to measure the temperature dependence of the lattice parameters of SBN40 single crystals. X-ray metric value of λ CuKα_1 [15] and high quality single crystals were required to carry out such precise measurement. Lattice parameters were determined from absolute shift of the reflex position (chosen at sufficiently high 2θ angle), which was additionally corrected because of the systematic uncertainties of shifts. The calculations of lattice parameters were based on 16,0,0 reflection (θ = 80.879°) and 0,0,5 reflection (θ = 78.146°) for the orientations parallel and perpendicular to the tetragonal *c*-axis, respectively. More details information

related to the measurement procedure was reported elsewhere [16]. All measurements of lattice parameters were carried out in the air in a temperature range of 20-200 °C. Throughout the measurements, the temperature of the sample was detected using Ni-CrNi thermocouple with a stability of ± 0.1 °C. Based on the temperature dependence lattice parameters, the obtained volume of the SBN40 elementary unit cell as a function of temperature was calculated.

6.3 Results and discussion

6.3.1 Effects of temperature

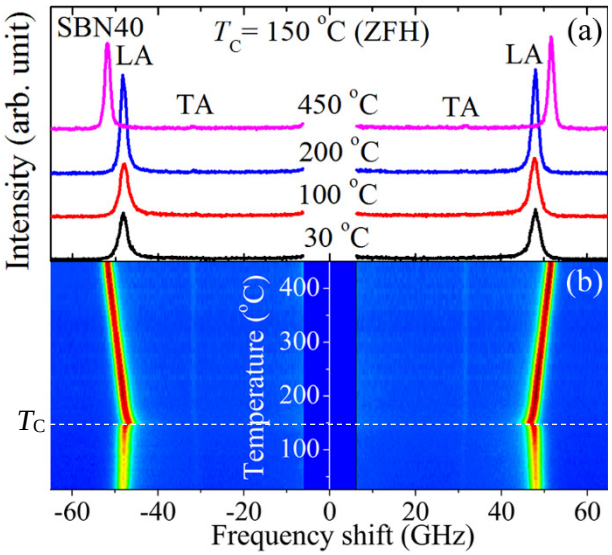

Fig. 6.1. (a) Brillouin scattering spectra of a *c*-plate SBN40 single crystal at some selected temperatures on ZFH. (b) Contour map of the scattering intensity vs temperature and LA frequency shift (red and blue colors indicate the high and low intensities, respectively). The elastic scattering near 0 GHz was removed.

Figure 6.1(a) shows the obtained typical Brillouin scattering spectra of a *c*-plate SBN40 single crystal at some selected temperatures measured at $c(a,a+b)\bar{c}$ scattering geometry on a zero field heating (ZFH) process. The contour map of the scattering intensity vs temperature and frequency shift is shown in Fig. 6.1(b), where the elastic scattering around 0 GHz was removed. These observed spectra consist of the Brillouin peak doublets which attribute to the scattered longitudinal acoustic (LA) and transverse acoustic (TA) phonon modes near the Brillouin zone center. From Fig. 6.1, it is clearly observed that a very weak TA peak exists in the entire temperature range of 26 to 450 °C. Based on the selection rules, the TA mode is not allowed in case of tetragonal 4*mm* or 4/*mmm* point group at back scattering geometries except at $c(ab)\bar{c}$ [17] that is equivalent to the $c(a,a+b)\bar{c}$ scattering geometry. Therefore, the persistence of the TA mode in entire temperature range above and below T_C observed at $c(a,a+b)\bar{c}$ geometry signifies that the SBN40 single crystal belongs to the tetragonal symmetry both in paraelectric and ferroelectric phases. The observed Brillouin spectra were fitted using the Voigt functions, a convolution of Lorentzian and Gaussian functions where the width of Gaussian function was fixed as an instrumental function, to extract the frequency

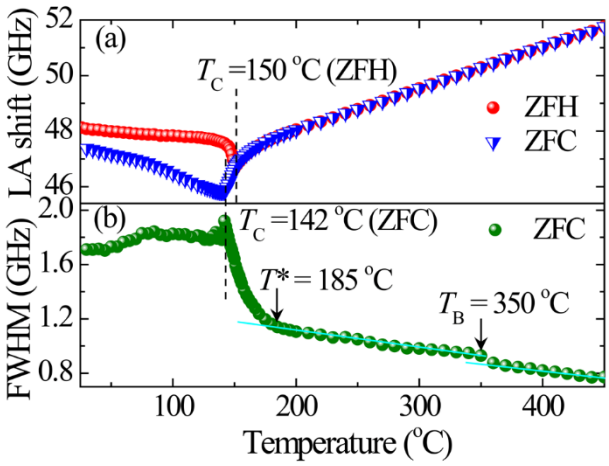

Fig. 6.2. Temperature dependences of (a) the LA shift on ZFH and ZFC and (b) LA FWHM on ZFC.

shift ν_B, the full width at half maximum (FWHM) Γ_B, and the peak intensity of the phonon modes. The obtained ν_B and FWHM of the LA mode were plotted as functions of temperature as shown in Fig. 6.2(a) and 6.2(b), respectively. From Fig. 6.2(a), a much sharper minimum of ν_B was found at 150 ºC on ZFH, while minimum of ν_B was observed at 142 ºC on zero field cooling (ZFC). In a ferroelectric phase below T_C, the marked difference between ZFH and ZFC is due to the metastable irreversible domain structure caused by an incomplete switching/alignment of nanodomains induced by quenched RFs during a cooling process [18,19]. The relatively sharp phase transition on ZFH and a noticeable thermal hysteresis observed in the LA shift between ZFH and ZFC processes indicate the existence of relatively weak RFs in the SBN40 single crystal. Similar acoustic hysteresis behavior was also observed in other REFs [3,19-21].

The acoustic properties become very sensitive at the characteristic temperatures of PNRs and show anomalous behavior at these temperatures via the scattering of LA phonons by PNRs [22]. Therefore, FWHM of the LA mode, which is directly proportional to the sound attenuation, was measured in the wide temperature range of 26 to 450 ºC as shown in Fig 6.2(b). On cooling from very high temperature, a deviation of the FWHM from its linear change was observed near 350 ºC owing to the appearance of dynamic PNRs which scatter LA phonons and result in an increase of the LA width. Another deviation of the FWHM from the linear temperature dependence was also observed at 185 ºC below which a noticeable increase in the LA width was observed owing to the dynamic-to-static transition of PNRs and scattering of the LA phonons by static PNRs [23]. Therefore, these anomalies can be attributed to the characteristic temperatures of PNRs in SBN40 single crystal, *i.e.*, T_B = 350 ºC and T^* = 185 ºC. It was observed that the obtained T_B and T^* were comparable to those of SBN61, SBN70, and SBN75 [3,10,24], and supposed to be common for all possible compositions of SBN. In Pb-based REFs with perovskite structure, a similar composition-independent behavior was also observed [25]. The increase of the scattering of LA mode by PNRs become discontinued at T_C, because most of the PNRs become frozen into the ferroelectric nanodomain state. T_C = 142 ºC and 150 ºC were observed from the temperature dependence of FWHM of the LA mode on ZFC and ZFH, respectively. Fig. 6.3 shows the temperature dependence of unit cell volume of SBN40 single crystal on ZFH. A clear deviation of the unit cell volume from its high-temperature linearity was observed at T = 142 ºC.

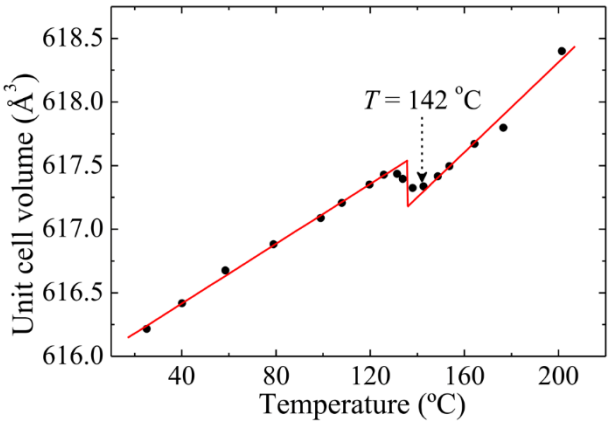

Fig. 6.3. Temperature dependence of unit cell volume of SBN40 single crystal on ZFH.

It indicates that the SBN40 single crystal undergoes a structural transition from the high-temperature nonpolar 4/*mmm* to the low-temperature polar 4*mm* tetragonal symmetry. This result was consistent with the Brillouin scattering measurement, and this temperature was identified as T_C = 142 ºC on ZFC as shown in Fig. 6.2(b), where T_C = 150 ºC was observed on ZFH. A small discrepancy in temperature may be because of the different procedures of experiments.

To confirm the relaxor nature of SBN40 single crystal, the relaxation time of LA mode τ_{LA} was estimated from ν_B and Γ_B using the following equation [26,27]:

$$\tau_{LA}=\frac{\Gamma_B-\Gamma_\infty}{2\pi\left(\nu_\infty^2-\nu_B^2\right)}, \tag{6.1}$$

where Γ_∞ is the background damping estimated from FWHM at the highest temperature in Fig. 6.2(b), *i.e.*, in the present case the value of Γ_∞ is 0.77 GHz at 450 °C, and ν_∞ is the LA shift at a very high temperature region (>T_B), where it shows a linear temperature dependence [27]. In the very high-temperature region above T_B, ferroelectric materials are in a paraelectric phase without having any PNRs. In this high-temperature region, a linear temperature dependence of ν_B is observed only because of the lattice anharmonicity [28]. To determine the ν_∞, the high temperature linear part of ν_B above T_B was fitted by a linear

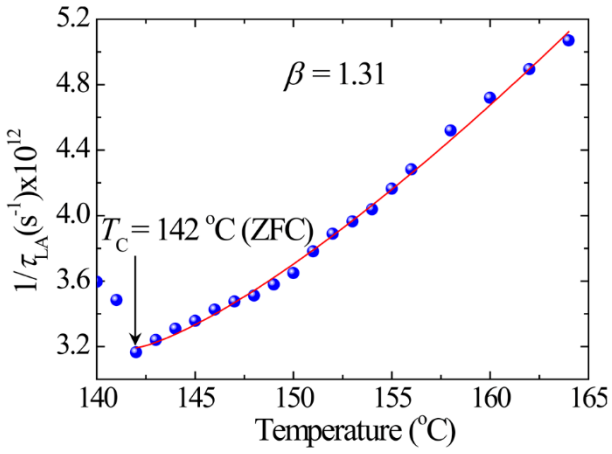

Fig. 6.4. Temperature dependence of the inverse relaxation time shows the stretched slowing down.

function $\nu_\infty(T) = 45.36 + 0.01421 \times T$ (GHz). It should be mentioned that the τ_{LA} is not sensitive to the choice of ν_∞, even if the highest value of ν_B at 450 °C is considered as ν_∞, almost the same value of τ_{LA} is obtained. The temperature dependence of the inverse of τ_{LA} was shown in Fig. 6.4, where the solid line represents the best fitted curve using the following equation [29]:

$$\frac{1}{\tau_{LA}} = \frac{1}{\tau_0} + \frac{1}{\tau_1}\left(\frac{T-T_C}{T_C}\right)^{\beta}, (1 \le \beta) \text{ for } T > T_C, \quad (6.2)$$

where stretching index $\beta = 1.0$ signifies the normal critical slowing down without RFs, while $\beta > 1.0$ indicates the stretched slowing down of the relaxation time owing to the increase of the strength of RFs [13]. From the best fitting of inverse τ_{LA} using Eq. (6.2) (Fig. 6.4) yields $\tau_0 = 0.31$ ps and $\tau_1 = 0.04$ ps, while $\beta = 1.31$ signifies that SBN40 single crystal exhibits the stretched critical slowing down of PNRs. Since $\beta = 3.0$, 2.6, and 2.58 were reported for PZN-7PT [29], PMN-30PT [30], and SBN70 [10], respectively, the SBN40 single crystal is a relaxor ferroelectric with comparatively very weak RFs. Therefore, a very weak frequency dependence was observed in dielectric susceptibility, and as a result, it was suggested that the phase transition is weakly first order and the SBN40 single crystal is a crossover material from normal to REFs [31].

6.3.2 Effects of external electric field

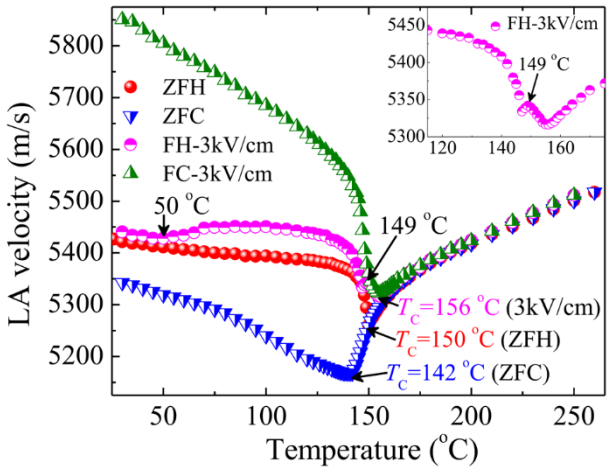

Fig. 6.5. Temperature dependence of LA velocity under 3 kV/cm electric field along the [001] direction.

The LA velocity (V_{LA}) was obtained from ν_B using the equation $V_{LA} = \lambda \nu_B / 2n$, where λ and n are the wavelength of the incident laser light (532 nm at the present case) and the ordinary refractive index of the sample at λ, respectively. $n = 2.363$ was reported for a SBN40 single crystal at the incident laser wavelength of 532 nm [32]. Figure 5 shows the temperature dependence of V_{LA} under electric field $E = 0$ and 3.0 kV/cm along the [001] direction on heating and cooling processes. On field heating (FH) under $E = 3.0$ kV/cm (pink curve in Fig. 6.5), a broad and weak anomaly in V_{LA} was observed at around 50 °C. It suggests an incomplete alignment of nanodomains owing to the formation of cluster-glass type state induced by the interaction among PNRs [7,33]. The formation of the cluster-glass state can be confirmed by observing the memory

and rejuvenation effects after isothermal aging in the ferroelectric phase [7]. Upon further heating, a sharp and small increase in V_{LA} was observed at around 149 °C (inset of Fig. 6.5) owing to a complete switching/alignment of the nanodomain state induced by RFs into the macro/single domain states induced by the external electric field. A similar acoustic anomaly was reported at the low temperature region of CBN30 single crystal [11], while the anomaly near T_C was not observed. Probably the applied electric field was not sufficient for overcoming the RFs and switching the nanodomains. On the other hand, a sharp and strong acoustic anomaly near T_C was observed in SBN70 single crystal under E = 3.0 kV/cm owing to a complete switching/alignment of nanodomains into a field-induced macro/single domain state by the complete suppression of RFs [10]. In the low temperature region of REFs, PNRs are frozen and strongly correlated with each other, hence the alignment of nanodomains under the external E becomes restricted. When the temperature increases towards T_C, the correlation among PNRs becomes very weak. Hence, under a sufficiently high E, the alignment of nanodomains/static PNRs becomes facilitated which enables a complete switching/alignment into the macro/single domain states. Therefore, near T_C, 3.0 kV/cm field align all PNRs along the field direction. As a result, a complete switching/alignment of nanodomains into the macro/single domain states was observed at 149 ºC (inset of Fig. 6.5) [34]. On subsequent FC under the same E (olive curve in Fig. 6.5), the anomaly at 149 ºC was not observed because during previous FH, the nanodomains were completely aligned along the field direction. Since external field suppresses RFs which are responsible for the diffusive phase transition, a marked increase of V_{LA} and the decrease of diffuseness were observed below T_C. Therefore, the FC curve is actually corresponds to the field-induced macro/single domain states.

6.3.3 Effects of aging

Upon cooling, the disordered ferroelectrics containing random ionic radii and random charges such as PMN freeze out into a glassy state [35,36], while SBN containing the random cation vacancies, changes into a metastable domain state caused by RFs below T_C. The metastability of domains and pinning of the domain wall configurations by RFs result a very slow ‘aging’ dynamics of the structure, which drives the system towards the equilibrium [8]. If the disordered materials approach towards the thermal equilibrium, this actually subsides into the states of progressively lower free energy, *i.e.*, states of a lower electrical or magnetic susceptibility [37]. Although aging is a universal feature of disordered materials [6], which results a variety of metastable states, the nature of aging is different for the different types of disordered systems under variant temperature and field histories [38]. It was reported that the dielectric susceptibility of uniaxial relaxor SBN75 shows a hole-like aging in a ferroelectric domain state [8]. After isothermal aging of SBN75 below T_C, both rejuvenation and memory effects were also observed in the cyclic temperature experiments up to T_C, which indicates the existence of cluster glass-like disorder of a complex domain structure owing to strong RFs. At most recent, Kleemann *et al*. [7,36,39] reported the similar effects not only in heterovalent (SBN75, PMN) systems with strong RFs, but also in isovalent $BaTi_{1-x}Zr_xO_3$ (x = 0.35, BTZ35) system with weak RFs. It was also proposed that these effects might be a common signature of all REFs [39].

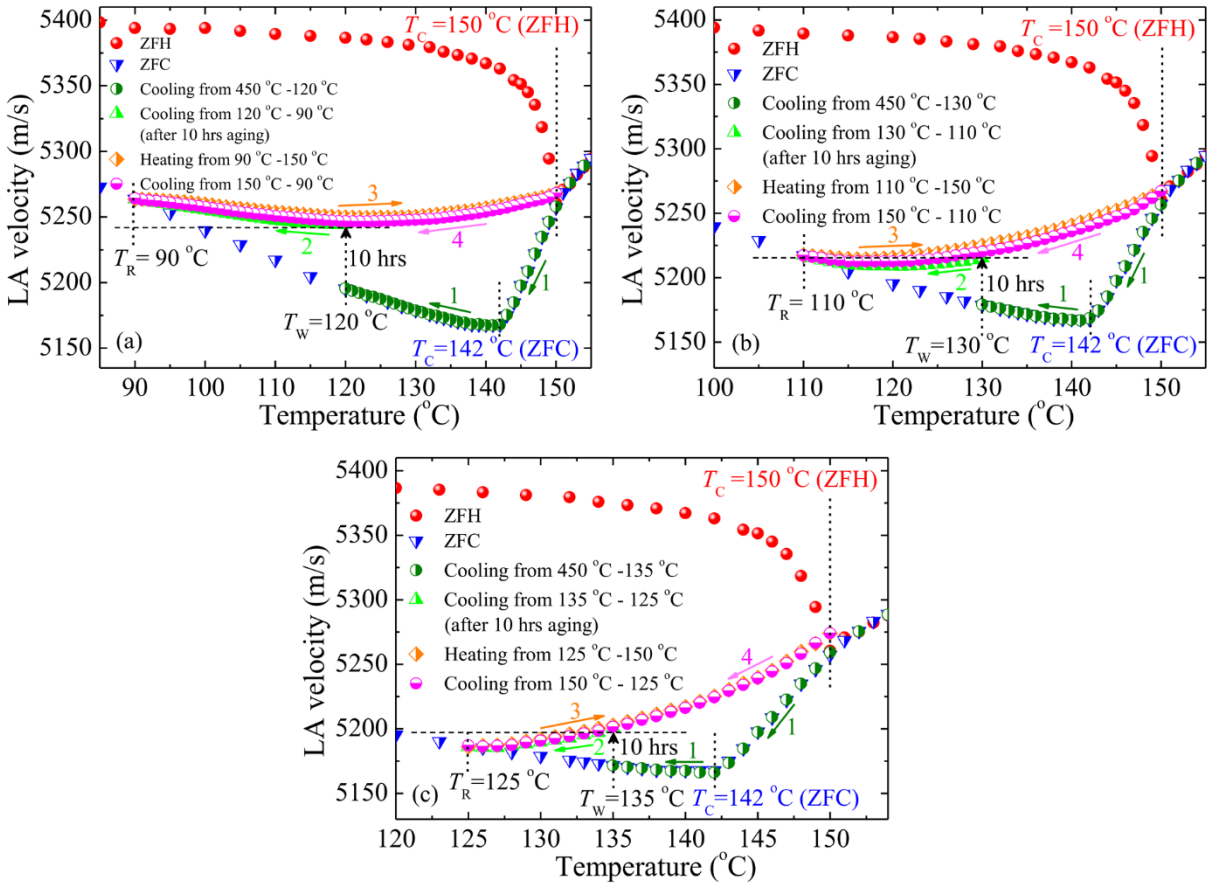

Fig. 6.6. LA velocity of SBN40 vs. temperature after ZFC from 450 °C on first cooling to T_W (curve 1), then aging for 10 h at (a) T_W = 120 °C, (b) T_W = 130 °C, and (c) T_W = 135 °C and cooling down (curve 2) until it merges with a ZFC reference curve at T_R, continuous reheating up to 150 °C (curve 3), and subsequent continuous cooling back to T_R (curve 4). Red circle and blue triangle are reference curves measured on ZFH and ZFC, respectively without aging.

In the present study, the isothermal aging experiments on SBN40 single crystals with weak RFs were conducted in the "ferroelectric" phase below T_C. Since during isothermal aging below T_C the deep 'hole' being burnt at a waiting temperature T_W, which indicates the approach of metastable domain states towards the equilibrium via lowering dielectric susceptibilities [8], it is expected that the aging at T_W will also affect the sound velocity V_{LA}. Figure 6.6 shows V_{LA} of SBN40 vs. temperature measured under the following conditions: (1) first the crystal was cooled from 450 °C to T_W on ZFC (curve 1), (2) then aging at (a) T_W = 120 °C, (b) T_W = 130 °C, and (c) T_W = 135 °C for 10 h and cooling down (curve 2) to a certain temperature T_R, where V_{LA} merges with the ZFC reference curve (blue curve), (3) continuous reheating up to 150 °C (curve 3), and (4) subsequent continuous cooling back to T_R (curve 4). Red and blue curves are the reference curves measured on ZFH and ZFC, respectively without aging. During isothermal aging below T_C, a growth into the macrodomain state from the nonequilibrium nanodomain state was observed [4,5], while RFs try to stabilize the nanodomain state by suppressing the formation of macrodomains [3,11]. As a result, after aging the crystal at T_W for 10 h under zero field, an increase of V_{LA} was observed. From Fig. 6.6 (a), one can presume that this fact is an irreversible growth into ordered domain or cumulative aging as

observed in classical ferroelectrics. But from Figs. 6.6(b) and 6.6(c), it was clearly seen that upon cooling from T_W, V_{LA} at first start to decrease (curve 2), then increase again and recover to the unaged state *i.e.*, rejuvenates at T_R, which excludes the possibility of being cumulative aging. On the other hand, the aged state was unaffected by cyclic temperature experiments up to T_C and merged with the unaged ZFC reference curve outside a narrow temperature range ('aging window') above and below T_W. This stable memory effect of aging, which recovers/rejuvenates at above and below T_W, indicates the existence of cluster-glass type state in the low-temperature region of REFs owing to the interaction among PNRs [34].

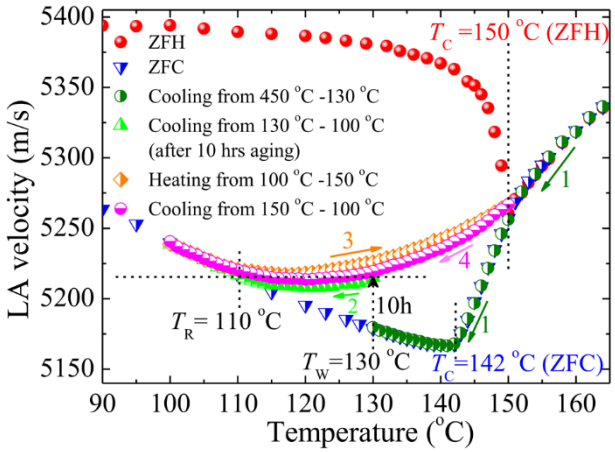

Fig. 6.7. LA velocity of SBN40 vs. temperature after ZFC from 450 °C on first cooling to T_W = 130 °C (curve 1), then aging for 10 h at T_W and cooling down to 100 °C (curve 2), continuous reheating up to 150 °C (curve 3), and subsequent continuous cooling back to 100 °C (curve 4). Red circle and blue triangle are reference curves measured on ZFH and ZFC, respectively without aging.

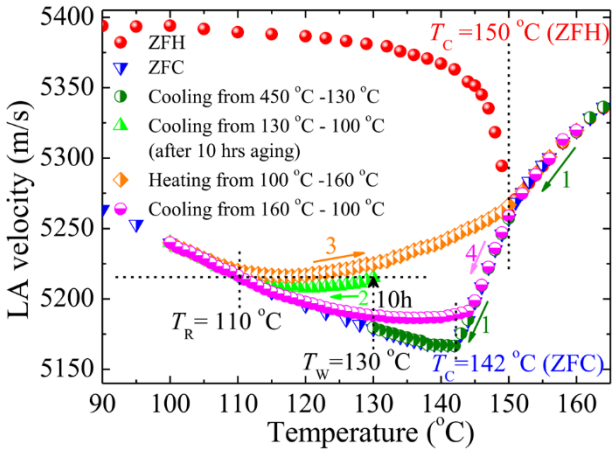

Fig. 6.8. LA velocity of SBN40 vs. temperature after ZFC from 450 °C on first cooling to T_W = 130 °C (curve 1), then aging for 10 h at T_W and cooling down to 100 °C (curve 2), continuous reheating up to 160 °C (curve 3), and subsequent continuous cooling back to 100 °C (curve 4). Red circle and blue triangle are reference curves measured on ZFH and ZFC, respectively without aging.

Figure 6.7 shows the aging experiment at T_W = 130 °C, where the cooling curve 2 had been extended to 10 °C below T_R =110 °C. It was clearly observed that below T_R, all (aged) curves almost completely merge with and follow the 'unaged' ZFC reference curve (blue curve) which confirms the complete

rejuvenation or recovery from the aging memory. In addition, when the heating curve 3 (orange curve) was extended up to 10 °C above T_C (= 150 °C on ZFH) and subsequent continuous cooling back to 100 °C (curve 4, pink curve), about 75% erase of an aging memory at T_W = 130 °C was observed as shown in Fig 6.8. As a result, the sound velocity (cooling curve 4, pink curve in Fig. 6.8) try to follow the unaged cooling curve 1 (olive curve) and merge with the 'unaged' ZFC reference curve (blue curve) at about 5 °C prior to T_R. Upon heating the crystal above T_C, a transition from the frozen/static to the dynamic state of PNRs initiates and consequently, the interaction among PNRs becomes weaker. Upon further heating above T^*, this transition become completed and all PNRs become dynamic and non-interacting and therefore, it was suggested that the memory of isothermal aging can be erased completely by heating the crystal above T^* [34].

From Fig. 6.6, it was clearly seen that the aging window between T_C and T_R markedly decreases to 60, 40, and 25 °C for the increase of T_W as 120, 130, and 135 °C, respectively. Consequently, by increasing T_W, a noticeable suppression of V_{LA} was also observed. Near T_C, the influence of RFs increases, which stabilize nanodomains by pinning of domain walls and prevent the formation of macrodomains. In addition, the fluctuations of local polarization of PNRs become stronger near T_C [11] and, hence, the V_{LA} decreases. On the other hand, when T_W approaches towards T_C, the interaction among PNRs becomes weaker and strong RFs make the nanodomains more stable by preventing the formation of macrodomains. As a result, near T_C, the return of the metastable state of V_{LA} (at T_W after 10h aging) to its initial/unaged nanodomain state (ZFC reference curve) becomes easier by a small temperature change through T_W. Therefore, at lower T_W, the correlation among PNRs is strong to cause a strong memory, which rejuvenates slowly and results in a larger T_C - T_R value. However, at higher T_W this correlation among PNRs becomes weaker and causes a weak memory, which rejuvenates quickly and results in a smaller T_C - T_R value.

6.4 Conclusions

The effect of an external dc electric field and aging on the LA velocity of a SBN40 single crystal were studied using the Brillouin scattering spectroscopy. Three characteristic temperatures of PNRs, namely, the Burns temperature T_B = 350 °C, the intermediate temperature T^* = 185 °C, and the Curie temperature T_C = 150 °C on ZFH and 142 °C on ZFC, were identified from the temperature dependence of the LA width. The temperature dependence of the inverse relaxation time signifies that the SBN40 single crystal exhibits a stretched critical slowing down of PNRs with the presence of RFs. The existence of the thermal hysteresis and the value of stretched index β = 1.31 indicates that the SBN40 single crystal is a relaxor ferroelectric with weak RFs. The effect of an external electric field along the [001] direction was clearly observed. On FH under 3.0 kV/cm, an incomplete alignment of nanodomains at 50 ºC owing to the formation of a cluster-glass state induced by the interaction among PNRs and a complete switching of a nanodomain to a macrodomain state at 149 ºC were observed. On subsequent FC, the anomaly at 149 ºC was not observed due to the complete switching of nanodomains during the previous FH process. As a result, a remarkable increase of LA velocity and decrease of diffuseness were also observed below T_C. A noticeable

thermal hysteresis was observed below T_C in the LA shift between ZFH and ZFC processes. It was also related to an incomplete switching of nanodomains caused by quenched RFs. After isothermal aging at T_W under zero field in a ferroelectric phase, an increase of LA velocity was observed, which was unaffected by the cyclic temperature experiments up to T_C and recovered to the initial unaged state (rejuvenated) within a narrow temperature range above and below T_W. This fact indicates that isothermal aging of SBN40 shows a clear memory and rejuvenation effects, which confirm the formation of a cluster-glass state in the low temperature region below T_C. By increasing T_W, a marked decrease of aging window (T_C - T_R) was observed owing to the weak interaction among PNRs. It was suggested that the memory of aging can be erased completely by heating the crystal above T*.

References

[1] R. Pirc and R. Blinc, Phys. Rev. B **76,** 020101(R) (2007).

[2] A. A. Bokov and Z.-G. Ye, J. Mater. Sci. **41,** 31 (2006).

[3] K. Matsumoto and S. Kojima, Jpn. J. Appl. Phys. **54,** 10NC04 (2015).

[4] V. V. Shvartsman and W. Kleemann, IEEE Trans. Ultrason. Ferroelectr. Freq. Control **53,** 2275 (2006).

[5] V. V. Shvartsman, W. Kleemann, T. Łukasiewicz, and J. Dec, Phys. Rev. B **77,** 054105 (2008).

[6] J.-P. Bouchaud, L. F. Cugliandolo, J. Kurchan, and M. Mézard, *Spin Glasses and Random Fields*, (World Scientific, Singapore, 1997).

[7] W. Kleemann, J. Dec, and S. Miga, Phase Transitions **88,** 234 (2015).

[8] J. Dec, W. Kleemann, S. Miga, V. V. Shvartsman, T. Łukasiewicz, and M. Świrkowicz, Phase Transitions **80,** 131 (2007).

[9] E. A. Kolchina, M. M. Neradovskiy, V. A. Shikhova, D. V. Pelegov, V. Ya. Shur, L. I. Ivleva, and J. Dec, Ferroelectrics **496**, 149 (2016).

[10] M. Aftabuzzaman, M. A. Helal, J. Dec, W. Kleemann, and S. Kojima, Jpn. J. Appl. Phys. **56**, 10PC06 (2017).

[11] M. Aftabuzzaman, J. Dec, W. Kleemann, and S. Kojima, Jpn. J. Appl. Phys. **55**, 10TC01 (2016).

[12] T. Łukasiewicz, M. A. Swirkowicz, J. Dec, W. Hofman, and W. Szyrski, J. Cryst. Growth **310**, 1464 (2008).

[13] S. Kojima, Jpn. J. Appl. Phys. **49**, 07HA01 (2010).

[14] W. L. Bond, Acta Cryst. **13,** 814 (1960).

[15] G. Hölzer, M. Fritsch, M. Deutsch, J. Härtwig, and E. Förster, Phys. Rev. A **56,** 4554 (1997).

[16] R. Paszkowski, K. Wokulska, T. Łukasiewicz, and J. Dec, Cryst. Res. Technol. **48,** 413 (2013).

[17] F. M. Jiang, J. -H. Ko, and S. Kojima, Phys. Rev. B **66**, 184301 (2002).

[18] S. Tsukada, Y. Hidaka, S. Kojima, A. A. Bokov, and Z.-G. Ye, Phys. Rev. B **87,** 014101 (2013).

[19] S. Tsukada, T. H. Kim, and S. Kojima, APL Mater. **1,** 032114 (2013).

[20] T. H. Kim, J. -H. Ko, and S. Kojima, Jpn. J. Appl. Phys. **52,** 09KC01 (2013).

[21] T. H. Kim, S. Kojima, and J. -H. Ko, Curr. Appl. Phys. **14,** 1643 (2014).

[22] J.-H. Ko, T. H. Kim, S. Kojima, K. -S. Lim, and T. -Y. Koo, Appl. Phys. Lett. **99,** 212902 (2011).

[23] K. Suzuki, K. Matsumoto, J. Dec, T. Łukasiewicz, W. Kleemann, and S. Kojima, Phys. Rev. B **90,** 064110 (2014).

[24] E. Dul'kin, S. Kojima, and M. Roth, J. Appl. Phys. **110**, 044106 (2011).

[25] M. Roth, E. Mojaev, E. Dul'kin, P. Gemeiner, and B. Dkhil, Phys. Rev. Lett. **98**, 265701 (2007).

[26] S. Tsukada and S. Kojima, Phys. Rev. B **78**, 144106 (2008).

[27] J.-H. Ko, T. H. Kim, S. Kojima, A. A. Bokov, and Z.-G. Ye, J. Phys.: Condens. Matter **22,** 485902 (2010).

[28] S. Tsukada, Y. Ike, J. Kano, T. Sekiya, Y. Shimojo, R. Wang, and S. Kojima, J. Phys. Soc. Jpn. **77,** 033707 (2008).

[29] S. Kojima and S. Tsukada, Ferroelectrics **405**, 32 (2010).

[30] M. Aftabuzzaman and S. Kojima, Jpn. J. Appl. Phys. **55**, 07KB03 (2016).

[31] S. Miga, W. Kleemann, J. Dec, and T. Łukasiewicz, Phys. Rev. B **80,** 220103R (2009).

[32] C. David, A. Tunyagi, K. Betzler, and M. Wöhlecke, Phys. Stat. Sol. (b) **244,** 2127 (2007).

[33] N. Novak, R. Pirc, M. Wencka, and Z. Kutnjak, Phys. Rev. Lett. **109,** 037601 (2012).

[34] M. Aftabuzzaman, M. A. Helal, R. Paszkowski, J. Dec, W. Kleemann, and S. Kojima, Sci. Rep. **7**, 11615 (2017).

[35] R. Pirc and R. Blinc, Phys. Rev. B **60,** 13470 (1999).

[36] W. Kleemann and J. Dec, Phys. Rev. B **94,** 174203 (2016).

[37] L. K. Chao, E. V. Colla, and M. B. Weissman, Phys. Rev. B **72,** 134105 (2005).

[38] E. Vincent, V. Dupuis, M. Alba, J. Hammann, and J.-P Bouchaud, Europhys. Lett. **50**, 674 (2000).

[39] W. Kleemann, J. Dec, and S. Miga, Ferroelectrics **499,** 72 (2016).

Chapter 7

Effect of Electric Field on Polar Nanoregions of Uniaxial Ferroelectric $Sr_{0.40}Ba_{0.60}Nb_2O_6$ with Weak Random Fields Studied by Brillouin Scattering

7.1 Introduction

Recently, uniaxial relaxor ferroelectrics (REFs) with strong random fields (RFs) such as $Ca_xBa_{1-x}Nb_2O_6$ (x = 0.30, CBN30) and $Sr_xBa_{1-x}Nb_2O_6$ (x = 0.70, SBN70) single crystals were studied under an external *dc* electric field using Brillouin scattering and an enhancement of the long-range order and an incomplete alignment of nanodomains below the Curie temperature T_C were reported [1,2]. In addition, the coexisting state of macrodomains and nanodomains was observed up to a high electric field because of the incomplete switching of nanodomains in both crystals. Most recently, a Brillouin scattering study of the electric field and aging effects on SBN40 single crystal with weak RFs were conducted in a ferroelectric phase below T_C [3]. It was reported that the SBN40 single crystal demonstrates a significant aging memory and rejuvenation effects, and exhibits a stretched critical slowing down of PNRs [3], which are observed in both typical perovskite and uniaxial tetragonal tungsten bronze (TTB) relaxors [4,5]. In addition, a very weak frequency dependence was observed in the dielectric susceptibility and speculated that it is a crossover material from normal to REFs [6]. The effect of an external electric field on nanodomains/static PNRs below T_C was also investigated [3]. However, the detail study of the effect of electric field on PNRs in TTB relaxors is hitherto insufficient and the role of PNRs in the domain states above and below T_C is still a puzzling issue of materials science.

The PNRs in a paraelectric phase and the nanodomain state or static PNRs in a ferroelectric phase are very sensitive to the external electric field by which the nanodomain state gradually switches into a metastable macro- or even a single domain state. Therefore, a variation in the acoustic properties of materials such as the sound velocity and sound attenuation can be expected. The Brillouin scattering spectroscopy is an advanced technique to determine the frequency shift and width of the acoustic phonons which are directly proportional to the velocity and attenuation of sound, respectively. Therefore, the Brillouin scattering spectroscopy is a very effective tool to study the effect of external electric field not only on PNRs in a paraelectric phase but also on the nanodomain state in a ferroelectric phase of relaxor materials. Since RFs try to stabilize the nanodomain state in a ferroelectric phase below T_C by pinning of the domain wall and prevent the growth of macrodomains [7], the stability of the nanodomain state or static PNRs mainly depends on the strength of RFs. In order to study the effect of electric field on PNRs above and below T_C, the SBN40 single crystal is a suitable material owing to its uniaxial spontaneous polarization and weak RFs which can easily be suppressed by a weak external electric field.

Therefore, in this study, the effect of external electric field on the acoustic properties of SBN40 single crystals were investigated using the Brillouin scattering spectroscopy to clarify the critical nature and the related functionality of PNRs and domain states above and below T_C in the uniaxial REFs with TTB structure.

7.2 Experimental methods

In order to grow the $Sr_xBa_{1-x}Nb_2O_6$ (x = 0.40, SBN40) single crystals, the Czochralski method was employed [8]. The *c*-plate crystals with 1 mm thickness and 5 × 5 mm^2 surfaces were used for measurements. The large surfaces of the crystal were polished to optical quality. Silver plate electrodes were coated on the larger surfaces of the crystal with a hole of 1 mm radius on one of the surfaces to apply an external dc electric field along the [001] direction. The Brillouin scattering spectra were collected in backward scattering geometry using a micro-Brillouin scattering system with a high-resolution six passes Sandercock-type tandem Fabry-Perot interferometer (JRS TFP-1) with a mirror spacing of 2 mm and a free spectral range of 75 GHz [9]. A single frequency green yttrium aluminium garnet (YAG) laser (Coherent Compass 315M-100) with a wavelength of 532 nm and 100 mW output power was employed as an excitation source. The temperature of the crystal was controlled with a stability of ± 0.1°C by using a Linkam THMS600 heating/cooling stage. Before the start of each measurement, the electrodes of the crystal were short-circuited for 10 min at a high enough temperature to erase any memory effect of external electric field retained from previous experiments.

7.3 Results and discussion

7.3.1 Effects of field cooling

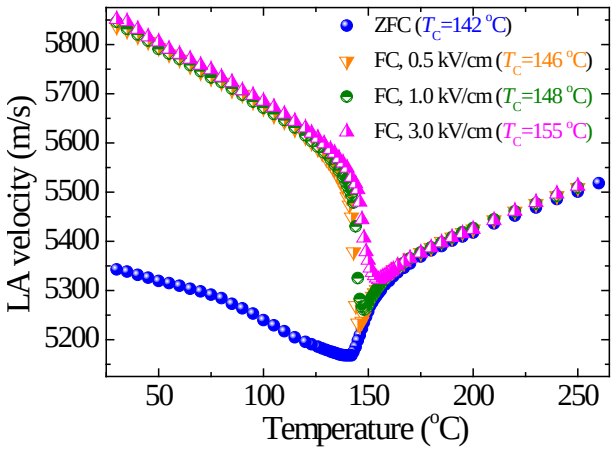

Fig. 7.1. Temperature dependences of LA velocity of a SBN40 single crystal under constant electric fields along the [001] direction on cooling.

The Brillouin spectra of a *c*-plate SBN40 single crystal were measured using $c(a,a+b)\bar{c}$ scattering geometry. To obtain the frequency shift ν_B, full width at half maximum (FWHM), and peak intensity of the acoustic phonon modes, the measured spectra were fitted using Voigt functions which are the convolution of Lorentzian and Gaussian functions, where the width of Gaussian function was fixed as an instrumental function. The LA velocity (V_{LA}) was determined from ν_B using the relation $V_{LA} = \lambda \nu_B / 2n_o$, where λ (= 532 nm) is the wavelength of the incident laser light and n_o (= 2.363 at λ for a SBN40 single crystal [10]) is the ordinary refractive index of the crystal. The characteristic temperatures of PNRs in SBN40 single crystal

such as the Burns temperature T_B = 350 °C, the intermediate temperature T^* = 185 °C, and T_C = 142 °C were reported on zero field cooling (ZFC) [3]. Figure 7.1 shows the temperature dependences of V_{LA} of a SBN40 single crystal on ZFC and field cooling (FC) processes under the external electric field E = 0.5, 1.0 and 3.0 kV/cm along the [001] direction. In the paraelectric phase above T_C, the external E overcomes the quenched RFs and easily aligns PNRs along the field direction owing to the weak interaction among PNRs. Therefore upon FC, PNRs become frozen with a preferred orientation induced by an external E [11] which causes a suppression of disorder in the crystal. As a result, a remarked increase of V_{LA} was observed below T_C on FC as shown in Fig. 7.1. Hence, on FC, the minimum of V_{LA} can be attributed to the field-induced T_C. From Fig. 7.1, it was clearly observed that all FC curves exhibit almost the saturated value of V_{LA} below the temperature T = 120 °C. It signifies that under sufficiently strong E, all PNRs in the paraelectric phase become aligned along the field direction owing to the complete suppression of RFs [12]. In addition, by cooling the crystal under an external E thus leads to the growth into macro/single domain states in a ferroelectric phase. Therefore, the FC states with a high V_{LA} below T = 120 °C actually corresponds to the field-induced macro/single domain states. By increasing the strength of external E, a gradual shift of the minimum of V_{LA} towards the high temperature region was also observed, which indicates an enhancement of the long-range order in a ferroelectric phase below T_C.

7.3.2 Effects of poling field strength and time

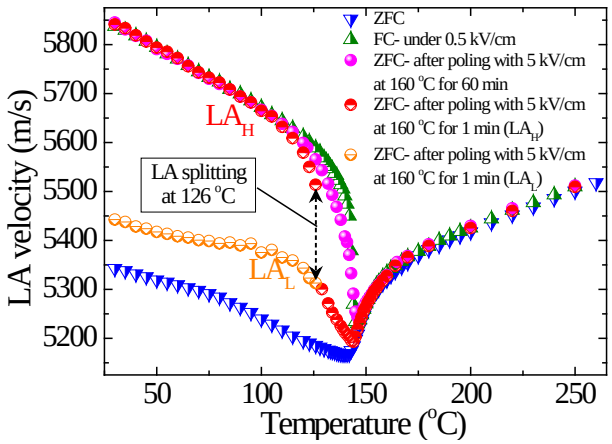

Fig. 7.2. Temperature dependences of LA velocity of a SBN40 single crystal on ZFC after poled the crystal with E = 5.0 kV/cm at 160 ºC for 60 min (pink curve) and 1 min (red and orange curve).

The poling measurements were carried out under the following procedures: (1) at first the crystal was poled with E = 5.0 kV/cm for a certain period of time at 160 ºC in the paraelectric phase below T^* = 185 ºC, (2) then E was removed, and (3) finally, Brillouin scattering spectra were measured on ZFC. The temperature dependences of V_{LA} of a SBN40 single crystal on ZFC after poled the crystal with E = 5.0 kV/cm at 160 ºC for 60 min (pink curve) and 1 min (red and orange curve), respectively, as shown in Fig 7.2. After poled the crystal with E = 5.0 kV/cm for 60 min at 160 ºC, V_{LA} upon ZFC (pink curve) was similar to that on FC with E = 0.5 kV/cm (olive curve in Fig. 7.2). This result indicates that poling the crystal with

such a high E for 60 min is sufficient to align all PNRs in the paraelectric phase along the field direction. As a result, V_{LA} of the poled crystal becomes comparable to that on FC under constant E. When the poling field was kept at E = 5.0 kV/cm and poling time was decreased to 1 min, a splitting of the LA mode below 126 ºC was observed (red and orange curve in Fig. 7.2). When the poling time was decreased to 1 min, some of PNRs switch back to their initial direction, and therefore, a splitting of the LA mode below T_C was observed [12]. In Fig. 7.2, the low-frequency LA (LA_L) mode corresponds to the nanodomains (orange curve) induced by quenched RFs, while the high-frequency LA (LA_H) mode corresponds to the macrodomains (red curve) induced by the external E. The temperature dependence of Brillouin scattering

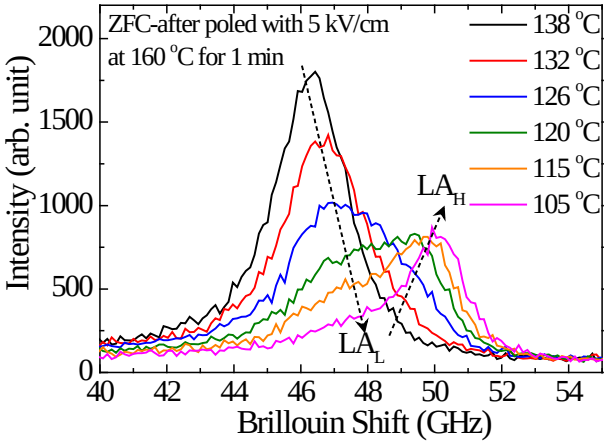

Fig. 7.3. Temperature dependence of Brillouin scattering spectra of the LA mode on ZFC after poled the crystal with E = 5.0 kV/cm at 160 ºC for 1 min.

spectra of the LA mode at some selected temperatures on ZFC after poled the crystal with E = 5.0 kV/cm at 160 ºC for 1 min is shown in Fig. 7.3. Upon decreasing the temperature, a gradual decrease in the intensity of the LA_L mode was observed. Consequently, an additional peak of the LA_H mode appears at the higher frequency. The intensities of the LA_L and LA_H modes are actually corresponds to the volumes of nanodomain and macrodomain states, respectively. It was observed that upon further decrease of temperature, the peak of LA_H mode starts to dominate below 120 ºC and becomes maximum at the room temperature. While a weak peak of the LA_L mode still persists with a very low intensity owing to the incomplete switching of nanodomains caused by quenched RFs. Therefore, from this observation it is clear that upon cooling, the tendency of the switching of nanodomains into the macro/single domain states below T_C is greatly enhanced in a partially poled crystal as compared to the un-poled one (blue curve in Fig. 7.2) [12].

7.3.3 Effects of electric field at constant temperature

Figure 7.4 shows the field dependence of Brillouin scattering spectra of a SBN40 single crystal at some selected E at 80 ºC. The electric field dependent V_{LA} was determined from ν_B obtained by fitting of these spectra, and plotted in the Fig. 7.5. In a ferroelectric phase below T_C, upon the application of an external E at constant temperature of 80 ºC, a coexisting state of nanodomains and macrodomains induced by RFs

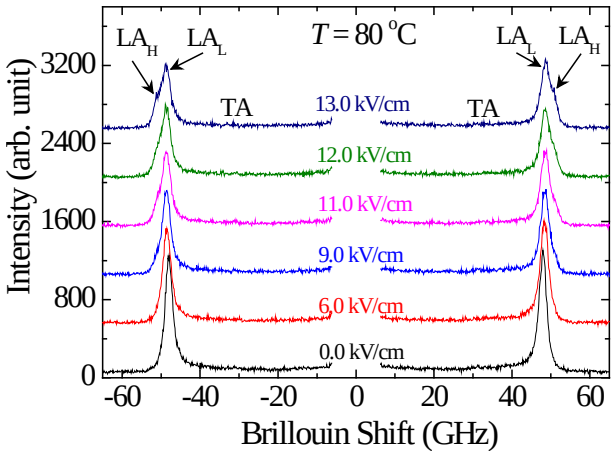

Fig. 7.4. Electric field dependence of Brillouin scattering spectra of a SBN40 single crystal at some selected electric fields at 80 ºC.

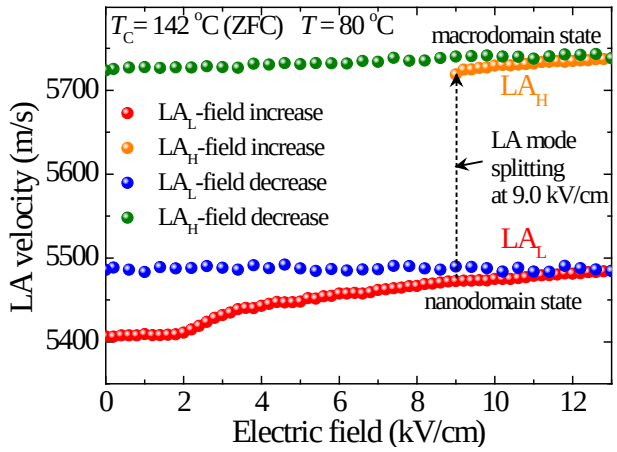

Fig. 7.5. Electric field dependence of V_{LA} of a SBN40 single crystal at 80 ºC.

and an external E, respectively, was also observed at about E = 9.0 kV/cm. Similar behavior of V_{LA} was also reported in other uniaxial REFs CBN30 and SBN70 single crystals with TTB structure [1,2]. The mixed state persists up to E = 13.0 kV/cm owing to the incomplete switching of the nanodomain into the macro/single domain states [12]. Below T_C, PNRs are strongly correlated with each other and therefore, the switching of nanodomains by the external E becomes interrupted [3] which results an incomplete switching. Even after removing the external E, the mixed state was observed. This strong memory effect of an external E can be removed by short-circuiting the electrodes of the crystal at above T* for more than 10 min.

7.4 Conclusions

The electric field effects on the acoustic properties of SBN40 crystals with weak RFs were investigated using Brillouin scattering spectroscopy. The effects of an external E along the [001] direction on PNRs in a paraelectric phase above T_C and nanodomains/static PNRs below T_C were clearly observed. On FC, the alignment of PNRs along the direction of E in a paraelectric phase above T_C and an enhancement of the long-range order in a ferroelectric phase below T_C were observed. After poling the crystal with a high E

for 60 min above T_C, the alignment of all PNRs along the field direction was also observed on ZFC. By decreasing the poling time to 1 min, some of the PNRs switch back which causes a splitting of the LA mode below T_C. In the field-dependent measurement below T_C, a mixed state consisting of macro- and nanodomains was persisted up to a very high E by the incomplete switching of nanodomains owing to the frustrated interaction among PNRs [3]. The mixed state persists even after removing the external E. This strong memory effect of external E can be erased by short-circuiting the electrodes of the crystal above T^* for more than 10 min.

References

[1] M. Aftabuzzaman, J. Dec, W. Kleemann, and S. Kojima, Jpn. J. Appl. Phys. **55**, 10TC01 (2016).

[2] M. Aftabuzzaman, M. A. Helal, J. Dec, W. Kleemann, and S. Kojima, Jpn. J. Appl. Phys. **56**, 10PC06 (2017).

[3] M. Aftabuzzaman, M. A. Helal, R. Paszkowski, J. Dec, W. Kleemann, and S. Kojima, Sci. Rep. **7**, 11615 (2017).

[4] W. Kleemann and J. Dec, Phys. Rev. B **94**, 174203 (2016).

[5] J. Dec, W. Kleemann, S. Miga, V. V. Shvartsman, T. Łukasiewicz and M. Świrkowicz, Phase Transitions **80**, 131 (2007).

[6] S. Miga, W. Kleemann, J. Dec, and T. Łukasiewicz, Phys. Rev. B **80**, 220103R (2009).

[7] K. Matsumoto and S. Kojima, Jpn. J. Appl. Phys. **54**, 10NC04 (2015).

[8] T. Łukasiewicz, M. A. Swirkowicz, J. Dec, W. Hofman, and W. Szyrski, J. Cryst. Growth **310**, 1464 (2008).

[9] S. Kojima, Jpn. J. Appl. Phys. **49**, 07HA01 (2010).

[10] C. David, A. Tunyagi, K. Betzler, and M. Wöhlecke, Phys. Stat. Sol. (b) **244**, 2127 (2007).

[11] M. Aftabuzzaman and S. Kojima, Ferroelectrics **513**, 38 (2017).

[12] M. Aftabuzzaman, J. Dec, W. Kleemann, and S. Kojima, Jpn. J. Appl. Phys. (accepted).

Chapter 8

Electric Field Effect on Acoustic Properties of Uniaxial Relaxor $Ca_{0.30}Ba_{0.70}Nb_2O_6$ Single Crystals with Relatively Strong Random Fields

8.1 Introduction

The uniaxial relaxor ferroelectrics (REFs) $Ca_xBa_{1-x}Nb_2O_6$ (CBN) single crystals with tetragonal tungsten bronze (TTB) structure show the similar physical properties as the $Sr_xBa_{1-x}Nb_2O_6$ (SBN) except their Curie temperatures T_C are much higher [1-5], which make CBN single crystals the potential candidates in relatively high-temperature applications. The CBN single crystals also exhibit a relatively lower degree of structural disorder which induces the relatively weak random fields (RFs), and therefore, the long range ferroelectric order and a weakly first-order phase transition at T_C were observed [6]. As a result, a relatively sharp peak in the dielectric spectra was observed near the phase transition of CBN [7]. By increasing the Ca content in CBN, a decrease of T_C and an increase of the diffuseness of phase transition were observed owing to the increase of disorder which results an enhancement of RFs that induce polar nanoregions (PNRs) at Burns temperature T_B [8,9]. Although the structure of CBN single crystals are similar to SBN, all functional properties of CBN are not exactly the same as SBN owing to the relatively weak RFs and smaller lattice parameters. It was suggested that the exceptional physical properties of SBN are due to the relatively small lattice parameters [10], while CBN crystals actually have lattice parameters smaller than those of SBN. Therefore, for the device applications, CBN crystals can be the better candidates. Recently, many experiments were conducted to study the uniaxial REFs CBN compounds with TTB structure. The effects of Ca content or doping oxides on the dielectric properties, relaxor nature, and the elastic properties of CBN crystals and ceramics were studied [6,11-14]. However, the effect of external electric field on PNRs in the vicinity T_C in a ferroelectric phase and the related acoustic properties of CBN single crystals have not yet been studied in details.

Therefore in the present study, the acoustic properties of CBN30 (x = 0.30) single crystals were investigated using broadband Brillouin scattering spectroscopy to discuss the critical nature of PNRs under the external electric field and the related functionality near T_C which will give the new insights into the uniaxial REFs with TTB structure.

8.2 Experimental methods

The $Ca_xBa_{1-x}Nb_2O_6$ (x = 0.30, CBN30) single crystals were synthesized by employing the Czochralski method [15]. Single crystal plates were cut along [001] (c-plate) with 1mm thickness and optically polished 5mm×5mm surfaces. Silver paste electrodes were attached on the larger faces with a hole of 1mm radius on one of the surfaces for applying a *dc* electric field along the [001] direction. Brillouin scattering spectra were measured in back scattering geometry using a high-contrast six passes tandem Fabry-Perot interferometer where the mirror spacing was set at 2 mm with a free spectral range of 75 GHz [16]. For exciting

source, a single frequency green Yttrium aluminium garnet (YAG) laser (Coherent Compass 315M-100) with a wavelength of 532 nm and output power of 100 mW was employed. A heating/cooling stage (Linkam THMS600) was employed to control the temperature of the specimen with a stability of ± 0.1°C. Before each measurement, the electrodes of the specimen were short-circuited for 15 min at a high enough temperature to erase any memory effect retained from previous treatments.

8.3 Results and discussion

8.3.1 Effects of temperature

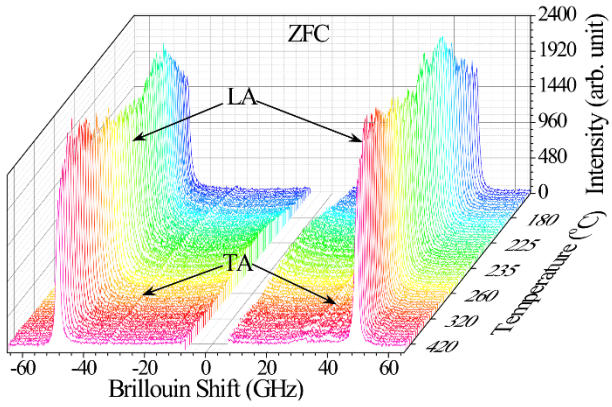

Fig. 8.1. Temperature dependence of Brillouin scattering spectra of a CBN30 single crystal on ZFC. LA and TA denote the longitudinal and transverse acoustic phonon modes, respectively.

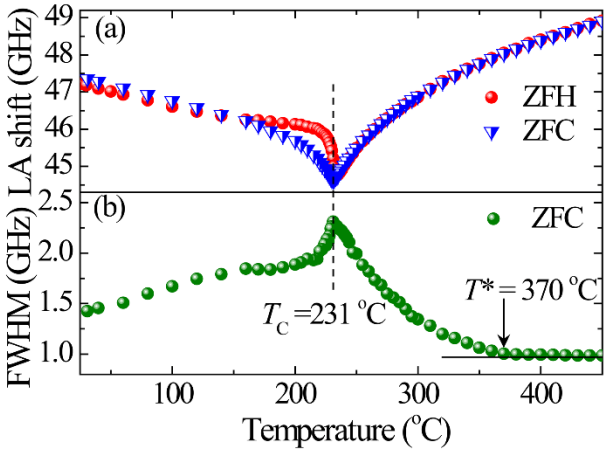

Fig. 8.2. Temperature dependences of (a) the LA shift on ZFH and ZFC and (b) FWHM on ZFC.

Figure 8.1 shows the typical Brillouin scattering spectra of a c-plate CBN30 single crystal observed on zero field cooling (ZFC) process. These spectra consist of the scattered longitudinal acoustic (LA) and transverse acoustic (TA) phonon modes near the the Brillouin zone center. From Fig. 2, it was clearly seen that the TA mode with very small intensity exists in all temperature range of 30 to 450 ºC, which signifies the tetragonal structure of CBN30 single crystals both in ferroelectric and paraelectric phases similar to SBN crystals [17-19]. The Brillouin scattering spectra were fitted using Voigt functions which are the convolution

of Gaussian and Lorentzian functions, where the width of Gaussian functions was considered as an instrumental function. Figure. 8.2 shows the obtained frequency shift ν_B and the full width at half maximum (FWHM) Γ_B of the LA mode plotted as a function of temperature. A marked thermal hysteresis between zero field heating (ZFH) and ZFC processes was observed in ν_B as shown in Fig. 8.2(a), indicating the relaxor nature, where ν_B exhibits a much sharper minimum at 234 ºC on the ZFH and at 231 ºC on ZFC processes. Similar acoustic hysteresis were reported in other REFs [2,20-22]. The acoustic properties of REFs show anomaly at characteristic temperatures of PNRs by scattering of acoustic phonons with PNRs [23]. Therefore, the temperature dependence of FWHM of LA mode was measured in a wide temperature range from 30 to 450 °C as shown in Fig. 8.2(b). On cooling from high temperature, an increase of the LA width owing to the scattering of LA phonons by dynamic PNRs near T_B were observed [18,19]. Since at the intermediate temperature T^*, the dynamic PNRs start to become static, a marked increase in the LA width was observed owing to the scattering of the LA mode by static PNRs [6,18,19]. At T_C, the increase of the scattering of LA mode becomes terminated because at this temperature most of the PNRs become frozen into ferroelectric nanodomain states. T^* = 370 °C, and T_C = 231 °C, were identified from temperature dependence of the LA width on ZFC process [17]. However in CBN28 (x = 0.28), T_B = 517 °C, T^* = 367 °C, and T_C = 254 °C were reported [6]. The T^* in CBN30 is very close to the CBN28 but T_C is 23°C lower owing to the increase of Ca content [8]. According to another high-temperature measurement up to 1023 °C (figure not shown), it was observed that T_B is also very close to the CBN28. Similar composition-independent effect was also reported in SBN crystals [2,18,19,23,24]. Therefore, T_B and T^* are supposed to be unaffected by compositions of Sr and Ca ions in SBN and CBN single crystals, respectively. This is very similar to the case of Pb-based REFs with perovskite structure [25].

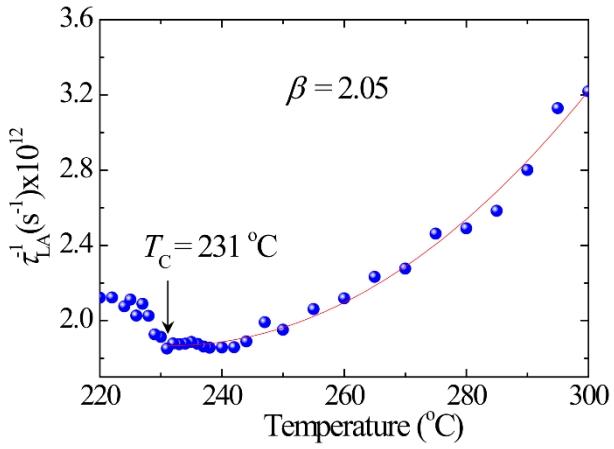

Fig. 8.3. Temperature dependence of inverse relaxation time shows the stretched slowing down.

In order to confirm the relaxor nature in CBN30 single crystal, the temperature dependent relaxation time of the LA mode τ_{LA} was determined by the equation [26,27]:

$$\tau_{LA} = \frac{\Gamma_B - \Gamma_\infty}{2\pi\left(\nu_\infty^2 - \nu_B^2\right)}, \qquad (8.1)$$

where Γ_∞ is the background damping estimated from FWHM at the highest temperature in Fig. 8.2(b), ν_∞ is the LA shift at a very high temperature region ($>T_B$), where it shows a linear temperature dependence [27]. Figure 8.3 shows the inverse relaxation time as a function of temperature, where the solid line represents the best fitted curve using the equation [28]:

$$\frac{1}{\tau_{LA}} = \frac{1}{\tau_0} + \frac{1}{\tau_1}\left(\frac{T-T_C}{T_C}\right)^{\beta}, (1 \le \beta) \text{ for } T > T_C, \tag{8.2}$$

where the stretched index $\beta = 1.0$ denotes to the normal critical slowing down without RFs, while $\beta > 1.0$ denotes the stretched slowing down of relaxation time by the increase of the strength of RFs [16]. From Fig. 8.3, $\beta = 2.05$ was observed, which indicates that CBN30 single crystal shows the stretched critical slowing down of PNRs. Since $\beta = 3.0$, 2.6, and 2.58 were reported for PZN-7PT [28], PMN-30PT [29], and SBN70 [18], respectively, the strength of RFs in CBN30 single crystal is relatively strong [17].

8.3.2 Effects of external electric field

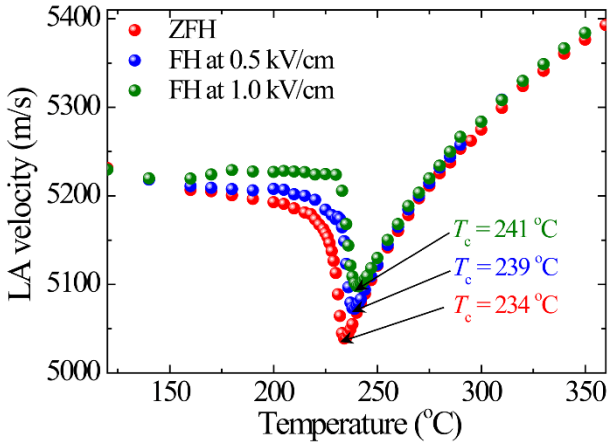

Fig. 8.4. Temperature dependence of LA velocities of a CBN30 single crystal under constant electric fields along the [001] direction on heating.

The LA velocity V_{LA} was determined from ν_B using the relation $V_{LA} = \lambda \nu_B / 2n_o$, where λ and n_o denote the wavelength of laser (532 nm) and the ordinary refractive index at λ, respectively. In CBN30, $n_o = 2.363$ was reported for the incident laser wavelength of 532 nm [12]. Figure 8.4 shows the temperature dependence of V_{LA} on ZFH and under external electric field $E = 0.5$ and 1.0 kV/cm along the [001] direction. On field heating (FH) under $E = 1.0$ kV/cm (olive curve), an increase in V_{LA} was observed at around 160 ºC owing to the incomplete alignment of nanodomains caused by strong interaction among PNRs. This anomaly is similar to the low temperature anomaly in SBN40 single crystal [19]. While in CBN30 crystal, the anomaly near T_C was not observed. Presumably $E = 1.0$ kV/cm was not sufficient to complete switching/alignment of nanodomains by overcoming RFs. With the increase of E from 0 to 1.0 kV/cm, T_C shifts from 234 to 241 °C at which a sharp minimum of V_{LA} was observed. It indicates that the long-range

ferroelectric order is enhanced. Under E = 0.5 kV/cm, the observed alignment of nanodomains and the shift of T_C (239 ºC) both were lower than that of under E =1.0 kV/cm. Consequently, the decrease of V_{LA} towards T_C was the similar fashion of ZFH. Since the external E suppresses RFs which are responsible for the diffusive phase transition, a decrease of the diffuseness is observed by increasing the strength of E. As a result, under higher E, the alignment of nanodomains becomes enhanced and the phase transition becomes sharper.

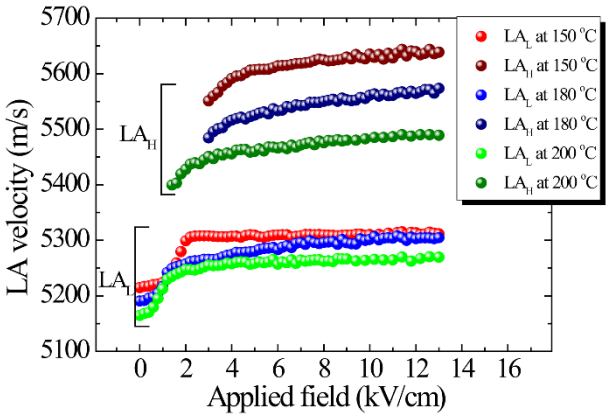

Fig. 8.5. Electric field dependence of LA velocities at 150, 180, and 200 ºC.

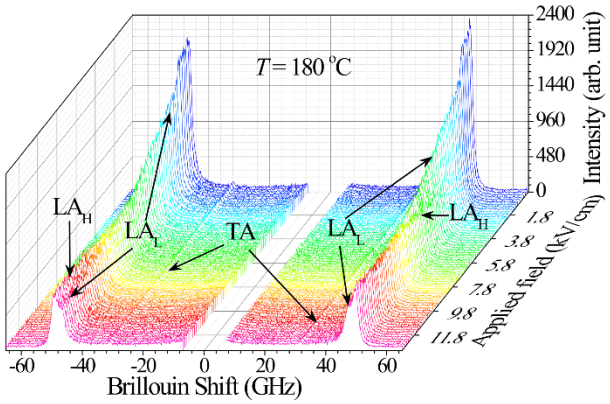

Fig. 8.6. Electric field dependence of Brillouin scattering spectra of a CBN30 single crystal at 180 ºC.

Figure 8.5 shows the electric field dependence of V_{LA} of a c-plate CBN30 single crystal after ZFC measured at constant temperatures of 150, 180, and 200 ºC. In a ferroelectric phase below T_C, by applying an external E to a ZFC crystal, a discontinuous transition of V_{LA} from a nanodomain state to an intermediate state of coexisting nano- and macrodomain was observed at $E \approx 3.0$ kV/cm as shown in Figs. 8.5 and 8.6. Where, the low-frequency LA (LA_L) modes correspond to nanodomains induced by RFs and the high-frequency LA (LA_H) modes correspond to macrodomains induced by the external E. Similar phenomena were also reported in other uniaxial TTB and cubic perovskite REFs [2,18,22,29]. The coexisting state was observed up to 13.0 kV/cm owing to the incomplete switching of nanodomains into the equilibrium macro/single domain states, caused by the strong interaction among PNRs. Similar incomplete switching of nanodomains was also observed in SBN70 single crystal [18]. When the temperature was increased towards T_C, a decrease of the frequency of both LA_L and LA_H modes were observed as shown in Fig. 8.5. In the vicinity of T_C, the effect of RFs enhances which try to stabilize nanodomains by pinning of domain walls and

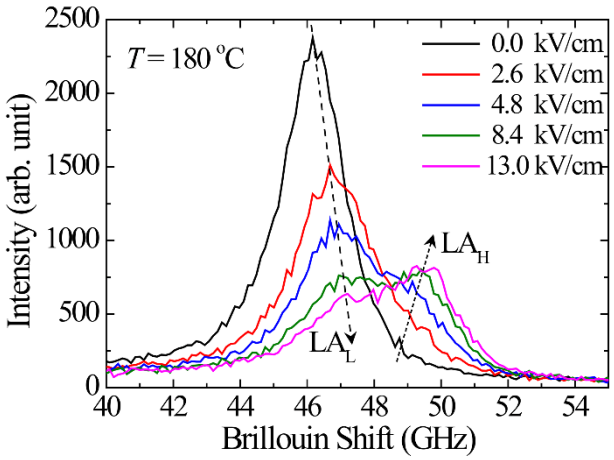

Fig. 8.7. Electric field dependence of Brillouin spectra of the LA mode at some selected E at 180 ºC.

consequently, suppress the growth of macrodomains. In addition near T_C, the electrostrictive coupling between local polarization of PNRs and the strain becomes stronger and hence, the frequency of both LA_L and LA_H modes decreases.

Figure 8.6 shows the electric field dependence of Brillouin scattering spectra of a CBN30 single crystal at 180 ºC, and Fig. 8.7 shows the Brillouin peak of an LA mode at some selected electric fields at the same temperature. When E was increased from zero to 3.0 kV/cm, the intensity of the peak of LA_L mode was gradually decreased and additional new peak of the LA_H mode was observed at a higher frequency. At E = 8.4 kV/cm, the intensity of both peaks were equal. Upon further increase of the field strength, the peak of LA_H mode starts to dominate and the double-peak state exists up to E = 13.0 kV/cm at which a very weak peak of LA_L mode still visible owing to quenched RFs. This double-peak state was observed even after removing the external E. This strong memory effect of external E can be removed by short-circuiting the electrodes of the crystal above T^* for more than 15 min.

8.4 Conclusions

A noticeable thermal hysteresis was observed between ZFH and ZFC which signifies the relaxor nature of a CBN30 single crystal. The intermediate temperature T^* = 370 °C and the Curie temperature T_C = 231 °C were observed from the temperature dependent FWHM on ZFC. From the fitting of temperature dependent inverse relaxation time, the stretched index β = 2.05 was observed, which indicates that the CBN30 single crystal exhibits the stretched critical slowing down of PNRs with the presence of relatively strong RFs. The effect of an external E along the [001] direction was clearly observed. From the temperature dependent V_{LA} at constant E, an incomplete alignment of nanodomains and an enhancement of the long-range ferroelectric order were observed below T_C. In the field dependent measurement below T_C, the mixed state consisting of macro- and nanodomains was observed at E = 3.0 kV/cm. This mixed state was existed up to a very high E because of the incomplete switching of nanodomains owing to the strong interaction among PNRs. After removing the external E, a strong field-induced memory effect was also observed, which can be erased by short-circuiting the electrodes above T^* for more than 15 min.

References

[1] M. Eßer, M. Burianek, D. Klimm, and M. Mühlberg, J. Cryst. Growth **240**, 1 (2002).

[2] K. Matsumoto and S. Kojima, Jpn. J. Appl. Phys. **54**, 10NC04 (2015).

[3] H. Song, H. Zhang, X. Xu, X. Hu, X. Cheng, J. Wang, and M. Jiang, Mater. Res. Bull. **40**, 643 (2005).

[4] H. Song, H. Zhang, Q. Jiang, X. Xu, C. Lu, X. Hu, J. Wang, and M. Jiang, J. Cryst. Growth **290**, 431 (2006).

[5] U. Heine, U. Völker, K. Betzler, M. Burianek, and M. Mühlberg, New J. Phys. **11**, 083021 (2009).

[6] K. Suzuki, K. Matsumoto, J. Dec, T. Łukasiewicz, W. Kleemann, and S. Kojima, Phys. Rev. B **90**, 064110 (2014).

[7] Y. J. Qi, C. J. Lu, J. Zhu, X. B. Chen, H. L. Song, H. J. Zhang, and X. G. Xu, Appl. Phys. Lett. **87**, 082904 (2005).

[8] K. Suzuki, K. Matsumoto, J. Dec, T. Łukasiewicz, W. Kleemann, and S. Kojima, Proc. 34th Symp. Ultrasonic Electronics, 2013, p. 29.

[9] G. Burns and F. H. Dacol, Solid State Commun. **48**, 853 (1983).

[10] S. Podlozhenov, H. A. Graetsch, J. Schneider, M. Ulex, M. Wöhlecke, and K. Betzler, Acta Crystallogr., Sect. B **62**, 960 (2006).

[11] X. K. Han, L. L. Wei, Z. P. Yang, and T. Zhang, Ceram. Int. **39**, 4853 (2013).

[12] M. Muehlberg, M. Burianek, B. Joschko, D. Klimm, A. Danilewsky, M. Gelissen, L. Bayarjargal, G. P. Görler, B.O. Hildmann, J. Cryst. Growth **310**, 2288 (2008).

[13] W. L. Gao, H. J. Zhang, S. Q. Xia, B. B. Huang, D. Liu, J. Y. Wang, M. H. Jiang, L. M. Zheng, J. F. Wang, and C. J. Lu, Mater. Res. Bull. **45**, 1209 (2010).

[14] S. Ke, H. Fan, H. Huang, H. L. W. Chan, and S. Yu, J. Appl. Phys. **104**, 024101 (2008).

[15] T. Łukasiewicz, M. A. Swirkowicz, J. Dec, W. Hofman, and W. Szyrski, J. Cryst. Growth **310**, 1464 (2008).

[16] S. Kojima, Jpn. J. Appl. Phys. **49**, 07HA01 (2010).

[17] M. Aftabuzzaman, J. Dec, W. Kleemann, and S. Kojima, Jpn. J. Appl. Phys. **55**, 10TC01 (2016).

[18] M. Aftabuzzaman, M. A. Helal, J. Dec, W. Kleemann, and S. Kojima, Jpn. J. Appl. Phys. **56**, 10PC06 (2017).

[19] M. Aftabuzzaman, M. A. Helal, R. Paszkowski, J. Dec, W. Kleemann, and S. Kojima, Sci. Rep. **7**, 11615 (2017).

[20] S. Tsukada, T. H. Kim, and S. Kojima, APL Mater. **1**, 032114 (2013).

[21] T. H. Kim, J. -H. Ko, and S. Kojima, Jpn. J. Appl. Phys. **52**, 09KC01 (2013).

[22] T. H. Kim, S. Kojima, and J. -H. Ko, Curr. Appl. Phys. **14**, 1643 (2014).

[23] J.-H. Ko, T. H. Kim, S. Kojima, K. -S. Lim, and T. -Y. Koo, Appl. Phys. Lett. **99**, 212902 (2011).

[24] E. Dul'kin, S. Kojima, and M. Roth, J. Appl. Phys. **110**, 044106 (2011).

[25] M. Roth, E. Mojaev, E. Dul'kin, P. Gemeiner, and B. Dkhil, Phys. Rev. Lett. **98**, 265701 (2007).

[26] S. Tsukada and S. Kojima, Phys. Rev. B **78**, 144106 (2008).

[27] J.-H. Ko, T. H. Kim, S. Kojima, A. A. Bokov, and Z.-G. Ye, J. Phys.: Condens. Matter **22,** 485902 (2010).

[28] S. Kojima and S. Tsukada, Ferroelectrics **405**, 32 (2010).

[29] M. Aftabuzzaman and S. Kojima, Jpn. J. Appl. Phys. **55**, 07KB03 (2016).

Chapter 9

Summary

This research was devoted to investigate the effects of temperature and electric field on the acoustic and dielectric properties of relaxor ferroelectrics (REFs) using Brillouin scattering and dielectric spectroscopy. It was done to clarify the critical nature and related functionality of polar nanoregions (PNRs) in domain states above and below the Curie temperature T_C. The materials to be studied were Pb-based cubic perovskite type $(1-x)Pb(Mg_{1/3}Nb_{2/3})O_3$-$xPbTiO_3$ (x = 0.30, PMN-30PT), and Pb-free uniaxial tetragonal tungsten bronze (TTB) type $Sr_xBa_{1-x}Nb_2O_6$ (x = 0.70, SBN70; x = 0.40, SBN40), and $Ca_xBa_{1-x}Nb_2O_6$ (x = 0.30, CBN30) single crystals. The major findings of this study are summarized as follows:

A remarkable thermal hysteresis between zero field heating (ZFH) and zero field cooling (ZFC), and a broad-diffused ferroelectric phase transition have been observed in all single crystals, which indicate that all single crystals studied here are relaxor ferroelectrics. Stretched index $\beta > 2$ for PMN-30PT, SBN70, and CBN30 single crystals indicates that they are REFs with strong random fields (RFs). While for SBN40, β = 1.31 indicates that the strength of RFs is very weak in SBN40. Due to the presence of strong RFs, the difference between ZFH and ZFC are small in PMN-30PT, SBN70, and CBN30 single crystals. While in SBN40, this difference is very large because of the very weak RFs. After removing the external electric field, a strong field-induced memory effect is observed in all single crystals studied here and the process of erasing this memory has also been clarified.

In PMN-30PT single crystal, a mixed state of nanodomain and macrodomain was observed under lower electric field both in Brillouin scattering and dielectric measurements because of the incomplete switching of nanodomains along the field direction. This mixed changes into macro/single domain states at the critical end point (CEP) at which the highest dielectric constant was observed. Therefore, it is suggested that at the CEP, the transition from mixed state to a macro/single domain states may be the origin of the maximum dielectric response in PMN-30PT single crystal with composition near the morphotropic phase boundary.

Upon the application of an external electric field, T_C of SBN70, SBN40, and CBN30 single crystals shift to the higher temperature. It indicates that the long-range ferroelectric order is enhanced. In SBN70, SBN40, and CBN30 single crystals, the mixed state persists up to a very high electric field because of the incomplete switching of nanodomains due to the interaction among PNRs in a low temperature ferroelectric phase. Electric field, aging memory and rejuvenation effects observed in SBN40 indicate that the cluster-glass type disorder state is formed in a low temperature ferroelectric phase due to the interaction among PNRs similar to other perovskite REFs. On field cooling from a high temperature paraelectric phase, a macro/single domain state can easily be obtained due a complete switching of nanodomains by a lower electric field, while on field heating from a low temperature ferroelectric phase, the complete switching was not observed due to the interaction among PNRs. It also indicates the presence of a cluster-glass type disorder state in a low temperature ferroelectric phase of uniaxial TTB REFs. The above findings can be helpful for not only in the device applications but also in the fundamental research of REFs.

List of publications closely related to my dissertation

1. **M. Aftabuzzaman** and S. Kojima,
   "Electric field effect of relaxor ferroelectric (1-*x*)Pb($Mg_{1/3}Nb_{2/3}$)O_3-*x*$PbTiO_3$ crystals near morphotropic phase boundary composition probed by Brillouin scattering" Jpn. J. Appl. Phys. **55**, 07KB03 (2016).

2. **M. Aftabuzzaman**, J. Dec, W. Kleemann, and S. Kojima,
   "Field dependent elastic anomaly in uniaxial tungsten bronze relaxors" Jpn. J. Appl. Phys. **55**, 10TC01 (2016).

3. **M. Aftabuzzaman** and S. Kojima,
   "Memory effects of relaxor ferroelectric 0.70Pb($Mg_{1/3}Nb_{2/3}$)O_3-0.30$PbTiO_3$ single crystals studied by dielectric spectroscopy" Ferroelectrics **513**, 38 (2017).

4. **M. Aftabuzzaman**, M. A. Helal, R. Paszkowski J. Dec, W. Kleemann, and S. Kojima,
   "Electric field and aging effects of uniaxial ferroelectrics $Sr_xBa_{1-x}Nb_2O_6$ probed by Brillouin scattering" Sci. Rep. **7**, 11615 (2017).

5. **M. Aftabuzzaman**, M. A. Helal, J. Dec, W. Kleemann, and S. Kojima,
   "Electric field effect on elastic properties of uniaxial relaxor $Sr_xBa_{1-x}Nb_2O_6$ single crystals with strong random fields" Jpn. J. Appl. Phys. **56**, 10PC06 (2017).

6. **M. Aftabuzzaman**, J. Dec, W. Kleemann, and S. Kojima,
   "Electric field effect on polar nanoregions of uniaxial ferroelectric $Sr_xBa_{1-x}Nb_2O_6$ with weak random fields studied by Brillouin scattering" Jpn. J. Appl. Phys. (**Accepted**).

Other related papers

1. M. A. Helal, **M. Aftabuzzaman**,
   S. Tsukada, and S. Kojima, “Role of polar nanoregions with weak random fields in Pb-based perovskite ferroelectrics” Sci. Rep. **7**, 44448 (2017).

2. M. A. Helal, **M. Aftabuzzaman**, S. Svirskas, J. Banys and S. Kojima,
   “Temperature evolution of central peaks and effect of electric field in relaxor ferroelectric $0.83Pb(Mg_{1/3}Nb_{2/3})O_3–0.17PbTiO_3$ single crystals” Jpn. J. Appl. Phys. **56**, 10PB03 (2017).

3. M. A. Helal, **M. Aftabuzzaman**, and S. Kojima,
   “Stretched slowing down in high-PT content PMN-*x*PT single crystals probed by Brillouin scattering” Ferroelectrics **519**, 109 (2017).

List of conferences

A. Oral presentations

1. **M. Aftabuzzaman**, M. A. Helal, J. Dec, W. Kleemann, and S. Kojima,
"Electric Field Induced Elastic Anomaly in Uniaxial Relaxor $Sr_{0.70}Ba_{0.30}Nb_2O_6$ Single Crystals" The 34th Meeting on Ferroelectric Materials and Their Applications (FMA34), 2017, Kyoto, Japan

2. **M. Aftabuzzaman**, M. A. Helal, J. Dec, W. Kleemann, and S. Kojima,
"Electric Field Induced Elastic Anomaly in Uniaxial Relaxor Ferroelectric $Ca_xBa_{1-x}Nb_2O_6$ Single Crystals Studied by Broadband Brillouin Scattering Spectroscopy" The 64th JSAP Spring Meeting, 2017, Yokohama, Japan

3. **M. Aftabuzzaman**, M. A. Helal, J. Dec, W. Kleemann, and S. Kojima,
"Electric Field Effect on Lead Free Relaxor Ferroelectrics with Uniaxial Tungsten Bronze Structure" International Conference on Technologically Advanced Materials and Asian Meeting on Ferroelectricity (ICTAM-AMF10), 2016, New Delhi, India

4. **M. Aftabuzzaman**, J. Dec, W. Kleemann, and S. Kojima,
"Field Dependent Elastic Anomaly in Uniaxial Tungsten Bronze Relaxors" The 33th Meeting on Ferroelectric Materials and Their Applications (FMA33), 2016, Kyoto, Japan

5. **M. Aftabuzzaman** and S. Kojima,
"Electric Field Effect of Relaxor Ferroelectric $0.7Pb(Mg_{1/3}Nb_{2/3})O_3$-$0.3PbTiO_3$ Single Crystals Studied by Micro-Brillouin Scattering" The 63rd JSAP Spring Meeting, 2016, Tokyo, Japan

6. **M. Aftabuzzaman** and S. Kojima,
"Effect of electric field on phase transition temperature in a $0.7Pb(Mg_{1/3}Nb_{2/3})O_3$-$0.3PbTiO_3$ single crystal" Tsukuba International Conference on Materials Science, IWP-2015, Tsukuba, Japan

B. Poster Presentations

1. **M. Aftabuzzaman**, J. Dec, W. Kleemann, and S. Kojima,
"Electric field effect on polar nanoregions of uniaxial ferroelectric $Sr_xBa_{1-x}Nb_2O_6$ with weak random fields studied by Brillouin scattering" The 38th Symposium on Ultrasonic Electronics, USE 2017, Tagajo, Japan

2. **M. Aftabuzzaman**, M. A. Helal, J. Dec, W. Kleemann, and S. Kojima,
"Effect of electric field on 180° domain switching in uniaxial $Ca_{0.30}Ba_{0.70}Nb_2O_6$ crystals studied by Brillouin scattering" The 14th International Meeting on Ferroelectricity (IMF2017), San Antonio, TX, USA

3. **M. Aftabuzzaman**, M. A. Helal, J. Dec, W. Kleemann, and S. Kojima,
"Electric Field Effect on Lead Free Uniaxial Relaxor $Sr_{0.4}Ba_{0.6}Nb_2O_6$ Single Crystal Studied by Brillouin Scattering" Fundamental Physics of Ferroelectrics and related materials 2017 (Ferro2017), Colonial Williamsburg, VA, USA

4. **M. Aftabuzzaman**, M. A. Helal, J. Dec, W. Kleemann, and S. Kojima,
"Electric field dependent elastic anomaly in uniaxial tungsten bronze relaxor ferroelectric $Ca_{0.30}Ba_{0.70}Nb_2O_6$ single crystals studied by Brillouin scattering spectroscopy" The 8th Japan-China Symposium on Ferroelectric Materials and Their Applications, 2016, Tsukuba, Japan

5. **M. Aftabuzzaman** and S. Kojima,
"Memory Effects of Relaxor Ferroelectric $0.70Pb(Mg_{1/3}Nb_{2/3})O_3$-$0.30PbTiO_3$ Single Crystals Studied by Dielectric Spectroscopy" 13th Russia/CIS/Baltic/Japan Symposium on Ferroelectricity (RCBJSF) and International Workshop on Relaxor Ferroelectrics (IWRF), 2016, Matsue, Japan

6. **M. Aftabuzzaman** and S. Kojima,
"Electric field effect of relaxor ferroelectric $(1-x)Pb(Mg_{1/3}Nb_{2/3})O_3$- $xPbTiO_3$ crystals near MPB composition probed by Brillouin scattering" The 36th Symposium on Ultrasonic Electronics, USE 2015, Tsukuba, Japan

List of awards

1. **“IWP2015 Prize” for the best presentation**

   Tsukuba International Conference on Materials Science, IWP-2015, Tsukuba, Japan

2. **“Young Scientist Award 2017”**

   The 38th Symposium on Ultrasonic Electronics, USE 2017, Tagajo, Japan

Acknowledgements

First of all, I would like to acknowledge and express my sincere regards and gratitude to **Prof. Seiji Kojima**, Institute of Materials Science, University of Tsukuba, for accepting me as a Ph.D. student in his research laboratory and providing me the opportunity to continue my research under his supervision. I am grateful to him for his inspiring guidance, encouragement, and invaluable suggestions during my Ph.D. research. Again I would like to express my heart-felt gratitude to **Prof. Seiji Kojima** for providing the continuous guidance and supervision even after his retirement from the last year. His wisdom and research expertise are invaluable in my life, and have greatly enriched my research experience.

I also would like to acknowledge and express my sincere regards and gratitude to my present supervisor **Prof. Kiyoto Matsuishi,** Institute of Materials Science, University of Tsukuba, for providing a great support by accepting me to continue my Ph.D. research under his supervision after the retirement of Prof. Seiji Kojima. I am also grateful to him for his kind cooperation.

I would like to thank Prof. Hisanori Tanimoto, Institute of Materials Science, University of Tsukuba, for being the co-supervisor of my Ph.D. thesis and for his kind cooperation.

I would like to thank Prof. Wolfgang Kleemann, Angewandte Physik, Universität Duisburg-Essen, Germany, for his valuable comments, expert opinion, and fruitful discussion on manuscripts related to the present research. I would like to thank Prof. Jan Dec, Institute of Materials Science, University of Silesia, Poland, for providing SBN70, SBN40 and CBN30 single crystals and his valuable comments and fruitful discussion on manuscripts related to the present research. I also would like to thank Mr. Robert Paszkowski, Institute of Materials Science, University of Silesia, Poland, for providing the X-ray measurement data of SBN40 single crystal.

I am so much thankful to Prof. Shinya Tsukada (Shimane University), for providing the experimental facilities, valuable suggestions, and explanations on the research results. I would like to thank Prof. Tatsuya Mori (University of Tsukuba), for his supports and kind cooperation to purchase accessories related to my research. I am also grateful to Prof. J. -H. Ko (Hallym University, South Korea), Dr. M. M. Rahaman (Rajshahi University, Bangladesh) and Dr. M. A. Helal (Begum Rokeya University, Bangladesh) for their fruitful discussion related to my research.

I would like to thank all of the existing and former members in our laboratory specially, my tutor Hashimoto san, Koda san, Sasaki san, Yamada san, Kabeya san, Nakano san, and Jiang san for their technical support, kind help, and very friendly behavior which provide me a happy and harmonious lab environment. I also would like to thank all of my good friends with whom I have enjoyed a happy life in Japan.

I am also thankful to the Japanese government for providing MONBUKAGASHO (MEXT) scholarship to support my study in Japan. For partial support in my research, Marubun Research Promotion and Murata Science Foundations are also gratefully acknowledged.

It would like to express my sincere gratitude to Prof. Al-Nakib Chowdhury (Dept. of Chemistry, BUET, and Ex-Vice-Chancellor, PUST, Bangladesh) for his great support and kind cooperation to proceed for Ph.D. study. I would like to thank my friends, colleagues, and well-wishers for their inspiration kind cooperation. Finally, I would like to thank all of my family members specially my wife, Mst. Firoza Khatun Rina for her sweet love, great patience, mental support, and encouragement during the course of my long stay in Japan.